Ductile Fracture Initiation in Compact Tension, Pressure Tube and Curved Compact Tension Specimens of Hydrided Irradiated Zr-2.5Nb Materials with Split Circumferential Hydrides

by

Shin-Jang Sung

A dissertation submitted in partial fulfillment
of the requirements for the degree of
Doctor of Philosophy
(Mechanical Engineering)
in the University of Michigan
2018

Doctoral Committee:

Professor Jwo Pan, Chair
Professor Yue Fan
Professor Wei Lu
Professor Jason McCormick

Shin-Jang Sung

sjsung@umich.edu

ORCID iD: 0000-0002-6477-7826

Dedication

To my wife and my family

Acknowledgements

I would like to express my sincere appreciation and gratitude to my advisor, Professor Jwo Pan, for his guidance, encouragement, and support throughout this research work. His intellectual support and insightful suggestions have been invaluable in enabling me to carry this work to completion. I would like to thank Professor Yue Fan, Professor Wei Lu, and Professor Jason McCormick of my doctoral committee for their efforts on providing valuable advices and suggestions.

I appreciate the financial support from the CANDU Owners Group for the research work reported in this dissertation. I am grateful to Dr. Douglas A. Scarth and Ms. Preeti Doddihal of Kinectrics for their support and useful discussions. I would like to thank Dr. Poh-Sang Lam of Savannah River National Laboratory for helpful suggestions, discussions and proofreading of the project reports. I would also like to thank Dr. Sterling St Lawrence and Dr. Brian Leitch of Chalk River Laboratories for fruitful discussions at several critical stages of this work. In addition, I also appreciate the experimental data and fractographs provided by Dr. Sterling St Lawrence of Chalk River Laboratories. I appreciate the financial support provided by Ford Motor Company and Michigan Memorial Phoenix Project Seed Funding Program for my research projects in the initial stage of my PhD program. Helpful discussions with Dr. Saeed Barbat of Ford Motor Company on our research project are also greatly appreciated.

I am thankful to my colleagues, Dr. William Lai and Dr. Mohammed Yusuf Ali, for their helpful instructions and discussions during my first two years of research works. I also appreciate the efforts of Mr. Frank Yan, Mr. Seung Hoon Hong and Mr. Wei-Ning Chen for

taking care of the critical experiments for our several research projects. I would like to thank Mr. Shengjia Wu for his efforts in extending our present research into a new research direction. Collaborations with Mr. Nikhil Kotasthane, Dr. Yugo Ashida, Mr. Jifan Chen, Ms. Lunyu Zhang and Mr. Chien-Po Huang in our several research projects are greatly appreciated.

Finally, I would like to thank my family and friends for their support and encouragement during my study at University of Michigan.

Table of Contents

List of Tables

List of Figures

List of Appendices

Nomenclature

a	half crack length
E_{ij}^{p}	macroscopic plastic strain
f	void volume fraction
f_0	initial void volume fraction
f_f	failure void volume fraction
F	bulging factor
h	hydride height
K_C	fracture toughness
K_I	mode I stress intensity factor
L	half tube length
p	applied internal pressure
p_0	applied internal pressure corresponding to K_C
P	applied load
P_0	applied load corresponding to K_C
q_1, q_2, q_3	parameters of the Gurson yield function
r, θ	polar coordinates defined on the axial-circumferential plane
R, Θ	polar coordinates defined on the radial-circumferential plane
R_i	inner radius
R_m	mean radius
R_o	outer radius
t	ligament thickness
T	tube thickness
W_p	macroscopic plastic energy dissipation
X, Y, Z	Cartesian coordinates
α	stress triaxiality ($=\sigma_m/\sigma_e$ or Σ_m/Σ_e)
$\overline{\alpha}$	average stress triaxiality
δ	ligament thickness ratio $(=t/h)$
ε_p	tensile plastic strain
$\bar{\varepsilon}_p$	effective plastic strain
$\bar{\varepsilon}_p^f$	failure effective plastic strain
λ	shell parameter
$d\Lambda$	proportionality factor

ν	Poisson's ratio
σ_0	stress on the plateau of the true stress-plastic strain curve
σ_e	tensile effective stress
σ_f	matrix flow stress
σ_h	hoop stress
σ_{ij}	stress tensor
σ'_{ij}	deviatoric stress tensor
σ_m	hydrostatic tension
σ_{RR}	out-of-plane normal stress
$\sigma_{\Theta\Theta}$	opening stress
σ_{yy}	opening stress
σ_{zz}	out-of-plane normal stress
Σ_e	macroscopic effective stress
Σ_{ij}	macroscopic stress tensor
Σ'_{ij}	macroscopic deviatoric stress tensor
Σ_m	macroscopic hydrostatic tension
Φ	Gurson yield function

Abstract

Zr-2.5Nb pressure tubes are primary containment components in CANDU (CANada Deuterium Uranium) reactors. One of the important reactor safety concerns is the fracture of the Zr-2.5Nb pressure tubes due to precipitation of circumferential hydrides. In this investigation, ductile fracture initiation with consideration of strain concentration and stress triaxiality near crack fronts in compact tension (CT), pressure tube (PT) and curved compact tension (CCT) specimens of hydrided irradiated Zr-2.5Nb pressure tube materials with split circumferential hydrides is investigated by three-dimensional finite element analyses with submodeling. The stress-strain relation for the irradiated Zr-2.5Nb pressure tube materials is taken as elastic plastic strain hardening with the perfectly plastic behavior at large plastic strains based on the experimental results of transverse tensile tests. A strain-based failure criterion with consideration of stress triaxiality is developed from the Gurson yield model with use of the experimental/computational results of transverse tensile tests and the effective plastic strain of the critical material element in CT specimens without hydride at fracture initiation.

The results of the three-dimensional finite element analyses of CT, PT and CCT specimens of irradiated Zr-2.5Nb pressure tube materials without circumferential hydrides suggest that circumferential hydrides ahead of the crack front in the middle of CT, PT and CCT specimens should fracture with the assumption of the hydride fracture stress of 750 MPa for the given load or internal pressure that corresponds to the same fracture toughness (Kc) of the irradiated Zr-2.5Nb pressure tube materials without circumferential hydrides. Based on a strain-based failure criterion with consideration of stress triaxiality, the fracture initiation is determined,

respectively, in the middle of the thickness for CT specimens, near the middle of the thickness for PT specimens, and at a quarter of the specimen thickness from the inner specimen surface for CCT specimens. The fracture initiation load or internal pressure corresponding to the same Kc based on the strain-based failure criterion with consideration of stress triaxiality for CCT specimens without hydrides is 2% lower than that for CT specimens without hydrides and is 4.3% lower than that for PT specimens without hydrides. The strain-based failure criterion with consideration of stress triaxiality can be used to describe the slightly higher fracture toughness for a PT specimen due to different constraint conditions and different types of loading, compared with that for a CCT specimen at room temperature.

For CT, PT and CCT specimens with split circumferential hydrides with various heights and ligament thicknesses, plastic strain concentration is observed in the middle of the ligament ahead of the crack front when the ratio of the ligament thickness to the hydride height is less than 3. With the strain-based failure criterion with consideration of stress triaxiality, the necessary fraction of the load for crack initiation is about 0.60 to 0.70 to fracture the ligaments when compared to that for CT, PT and CCT specimens without split circumferential hydrides. The computational results can be used to explain the near 35% reduction of the fracture toughness at room temperature obtained from hydrided irradiated PT and CCT specimens when compared with those from unhydrided irradiated ones.

Chapter 1 Introduction

The CANDU (Canada Deuterium Uranium) reactor, also named pressurized heavy-water reactor (PHWR), is a Generation-II type reactor, and has been used in the commercial nuclear power plants for about 50 years. The first large-scale commercial CANDU power plant is Pickering A station in Pickering, Ontario, which started operations in 1971 and is still in service [42]. Other reactors categorized as the Generation-II type includes [22]: light water reactors (LWR) including pressurized water reactors (PWR) and boiled water reactors (BWR), light water graphite reactors (LWGR or RMBK). One of the most important feature of CANDU reactors is that they use natural uranium (0.7% uranium-235) dioxide as fuel, instead of enriched uranium (2.5% - 4% uranium-235) [22]. As a result, heavy water, with less absorption of neutrons, needs to be used as a moderator in CANDU reactors.

1.1 CANDU Reactors

The core of a CANDU reactor is a cylindrical calandria stainless steel shell containing heavy water as moderator. Figure 1-1 shows a schematic plot of a calandria shell of a CANDU reactor. The calandria shell is penetrated by hundreds of horizontal annealed Zircaloy-2 calandria tubes, as shown in Figure 1-2. Inside a calandria tube, a pressure tube containing fuel bundles, shown in Figure 1-3, is inserted with four spacers to maintain the annular gap between the calandria tube and the pressure tube, as shown in the close-up in Figure 1-1. The gap is filled by carbon dioxide gas used as an insulator. Pressurized heavy water, as the primary coolant,

passes through the pressure tubes and transports the heat generated by fuel bundles to a steam generator to produce steam for turning an electricity generator. The cooled heavy water then goes back to the cooling loop [42]. The advantage of the design of a calandria containing hundreds of individual pressure tubes, instead of a large reactor pressure vessel (RPV) enclosing all fuels, is to allow refuelling without shutting down the whole reactor [22,42]. Fuel bundles can be replaced one pressure tube by one pressure tube so that only one pressure tube needs to be depressurized at one time while others are still working. Another advantage is that if there is any defect in fuel bundles, this design allows quick locating and removing the defective fuel bundle from the cooling loop. However, the CANDU design increases the number of primary containment components (pressure tubes), which also raises the possibility for the leak of coolant. In order to alleviate that risk, structural integrity assessments for pressure tubes are periodically conducted by mechanical testing of surveillance tubes removed from the service. The mechanical testing provides information on possible degradation in mechanical properties, due to irradiation and deuterium pickup, of pressure tube materials in service.

1.2 CANDU Pressure Tubes

Pressure tubes in CANDU reactors have been manufactured from cold-worked Zr-2.5Nb since 1971, as successors to Zircoloy-2 pressure tubes [9]. The microstructure of the cold-worked Zr-2.5Nb pressure tubes consists of elongated α-phase (HCP) containing about 1 wt% niobium, surrounded by a thin layer of β-phase (BCC) containing about 20 wt% niobium. The α-grain size is typically about 0.2 to 0.5 μm thick in the radial direction, with an aspect ratio of 1:5:50 in the radial, circumferential and axial direction. Duo to the specific cold-worked

process, the α-grains are preferentially oriented such that their basal poles are mostly in the circumferential direction [7].

Zr-2.5Nb pressure tubes typically have an inner radius of about 104 mm with the thickness of about 4.2 mm, a total length of 630 mm. They operate at an internal pressure of about 10 MPa and at a temperature ranging from about 250 to 265°C (inlet ends) to about 290 to 315°C (outlet ends) during normal conditions. Pressure tubes in service should satisfy a leak-before-break (LBB) criterion. The LBB criterion requires that any pressure tube which fails by crack propagation must leak sufficient coolant so that the annulus gas system can detect the change of moisture of the gas between calandria tubes and pressure tubes [42] before the crack becomes unstable (reaches critical crack length). The LBB criterion needs accurate fracture toughness values of Zr-2.5Nb pressure tube materials.

1.3 Fracture Toughness of Zr-2.5Nb Pressure Tube Materials

Fracture toughness values of Zr-2.5Nb pressure tube materials can vary due to several reasons, such as irradiation and presence of trace elements. Chow et al. [10] presented the effects of irradiation by measuring the ultimate tensile strength (UTS) and fracture toughness of Zr-2.5Nb materials of pressure tubes at about the operating temperature. The pressure tubes were removed from nuclear power plants after various years of service, up to 15 years. The results showed that the UTS increases and the fracture toughness decreases rapidly during the first few years of operation. After that, the UTS and the fracture toughness approaches to constants. As for the effects of trace elements, Theaker et al. [43] listed five trace elements detrimental to fracture toughness values of Zr-2.5Nb pressure tube materials, which are carbon, chlorine, phosphorus, oxygen and hydrogen. Among these trace elements, chlorine is directly

related to the formation of fissure structures, which can severely lower fracture toughness values of Zr-2.5Nb pressure tube materials. Aitchison and Davies [2] experimentally showed that fissures result from the microsegregation of chlorine and carbon (as carbide). Even a small amount of concentration (> 1 ppmw) of chlorine can sharply lower the value of fracture toughness of Zr-2.5Nb pressure tube materials [2,14]. The concentration of chlorine is so important that the specification for Zr-2.5Nb pressure tubes has introduced a maximum chlorine concentration value of 0.5 ppmw after 1987 while there was none before 1987 [14].

Another important trace element is hydrogen, which is related to the formation of hydrides. Hydrides are very brittle with fracture toughness value of about 1 $\mathrm{MPa}\cdot\sqrt{\mathrm{m}}$ at 25°C and 3 $\mathrm{MPa}\cdot\sqrt{\mathrm{m}}$ at 300°C, as investigated in Simpson and Cann [30]. The fracture strength of hydrides embedded in Zr-2.5Nb alloys is between 500 MPa to 800 MPa at temperature between 25°C to 250°C [8,20,29]. The compressive transformation stress results from volume expansion of hydride formation can be ignored if the length of hydrides is long enough (>50 μm) [20,29]. With consideration of the low fracture toughness value of hydrides and the relatively low fracture strength of hydrides, which is generally lower than the yield stress of its adjacent zirconium matrix, it can be inferred that the presence of hydrides in zirconium matrix can deteriorate the fracture toughness of Zr-2.5Nb pressure tube materials.

Typically, newly-made Zr-2.5Nb pressure tubes contain equivalent hydrogen concentration (hydrogen + 0.5 deuterium) of less than 25 ppmw, which was included in the specification before 1987 [14]. The terminal solid solubility (TSS) for hydride dissolution is about 29 ppmw at 250°C and less than 1 ppmw at room temperature [23]. For newly-installed pressure tubes under normal operating conditions, no or only few hydrides will precipitate in pressure tubes, and hydrogen effects are negligible. However, pressure tubes will gradually pick

up deuterium and the equivalent hydrogen concentration increases during service. The increase could reach 40 ppmw after 30 years of service [7], which means that hydrides will gradually precipitate in pressure tubes in service. Another extreme case is the shutdown of reactor. Due to the drastic decrease of temperature, the TSS also decreases so that extra hydrogen will precipitate as hydrides. As discussed above, either an increase of service years or a decrease of temperature could be detrimental to the fracture toughness of Zr-2.5Nb pressure tube materials. Due to these uncertainties, the maximum equivalent hydrogen concentration in the specification has been lowered to 5 ppmw since 1987 [14] to increase the safety margin.

1.4 Orientation of Hydrides

With the specific cold-worked process (a large amount of compressive strain in the radial direction [23]), most of the hydrides, if any, in newly-made pressure tubes are circumferential hydrides, with their platelet normals in the radial direction. However, after thermal cycling with an internal pressure which is large enough, the circumferential hydrides could dissolve and reprecipitate as reoriented hydrides (radial hydrides) [31]. The normals of radial hydrides are parallel to the applied tensile stress, which is in the circumferential direction of pressure tubes. The reorientation of hydrides happens only if the basal poles of HCP structure of α-grains are also along the maximum tensile stress [18]. It should be mentioned that radial hydrides in pressure tubes are usually expected to have more embrittlement effects than circumferential ones since radial hydrides are perpendicular to the hoop stress direction and parallel to the crack plane. The mechanism of radial hydrides on reduction of fracture toughness of Zr-2.5Nb pressure tube materials were already studied and well-known as delayed hydrogen cracking (DHC) [25]. However, the effects of circumferential hydrides on reduction of fracture toughness

were either unrecognized for Zr-2.5Nb cold-rolled sheet materials [1] or mentioned but not studied for Zr-2.5Nb pressure tube materials [32]. This is the gap this investigation is going to fill.

1.5 Scope of Work

In Chapter 2, ductile fracture initiation with consideration of strain concentration and stress triaxiality near crack fronts in compact tension (CT) specimens of hydrided irradiated Zr-2.5Nb materials with split circumferential hydrides is investigated by three-dimensional finite element analyses with submodeling. A strain-based failure criterion with consideration of stress triaxiality is developed from the Gurson yield model. With that fracture criterion at a critical distance ahead of the main crack front in the CT specimen, the implications of the strain concentration in the ligaments between circumferential hydrides on the fracture toughness of the irradiated Zr-2.5Nb materials are examined and investigated.

In Chapter 3, ductile fracture initiation with consideration of strain concentration and stress triaxiality near axial crack fronts in pressure tube (PT) specimens of hydrided irradiated Zr-2.5Nb materials with split circumferential hydrides is examined by three-dimensional finite element analyses with submodeling. The critical location along the crack front is determined based on the strain-based failure criterion with consideration of stress triaxiality as established in Chapter 2. Following the same failure criterion, the effects of the plastic strain concentration and stress triaxiality in the ligaments between circumferential hydrides on the fracture initiation in the PT specimens of irradiated Zr-2.5Nb materials with hydrides are examined and investigated.

In Chapter 4, the effects of curvature on ductile fracture initiation with consideration of strain concentration and stress triaxiality near crack fronts in curved compact tension (CCT)

specimens of hydrided irradiated Zr-2.5Nb materials with split circumferential hydrides are examined by three-dimensional finite element analyses with submodeling. The effects of the curvature on the J-integral distributions along the crack front, and on the stress and strain states ahead of the crack front in the CCT specimen are examined. The critical location along the crack front is determined based on the strain-based failure criterion with consideration of stress triaxiality as established in Chapter 2. The computational results of the CCT specimen are then benchmarked with those of the CT specimen to investigate the effects of the curvature on the fracture initiation loads for the CCT specimens. In addition, the computational results of the CT, PT and CCT specimens are examined to show the applicability that the fracture toughness values obtained from CCT specimens can be used to predict the fracture of pressure tube (PT) specimens. Following the same failure criterion, the effects of the plastic strain concentration and stress triaxiality in the ligaments between circumferential hydrides on the fracture initiation loads in the CCT specimens of irradiated Zr-2.5Nb materials with hydrides are examined and investigated.

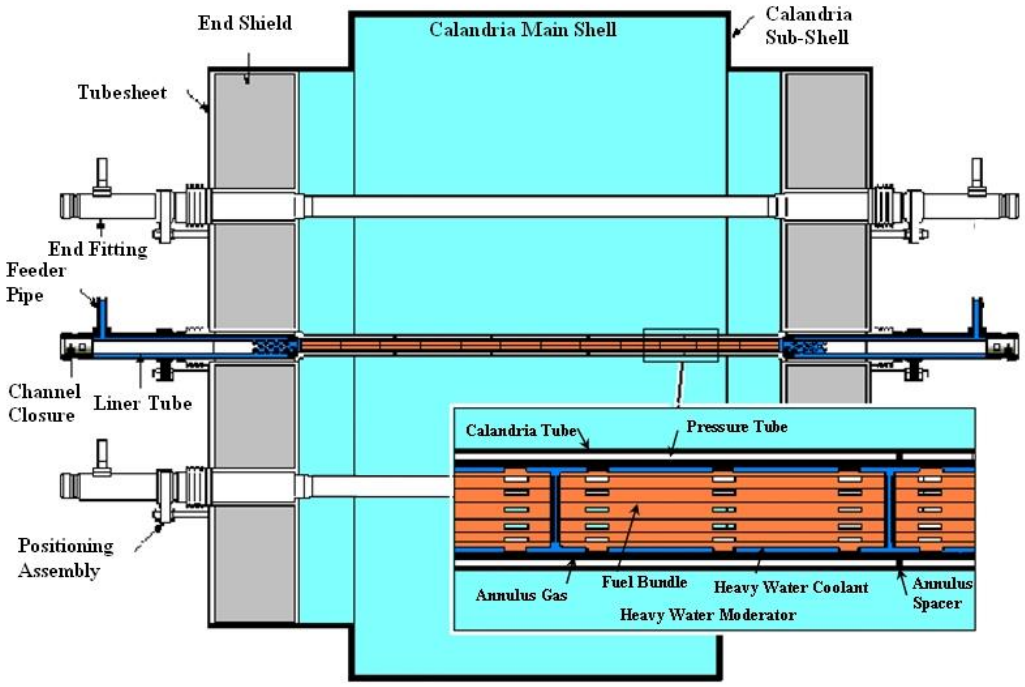

Figure 1-1. A schematic plot of a calandria shell in a CANDU reactor [19].

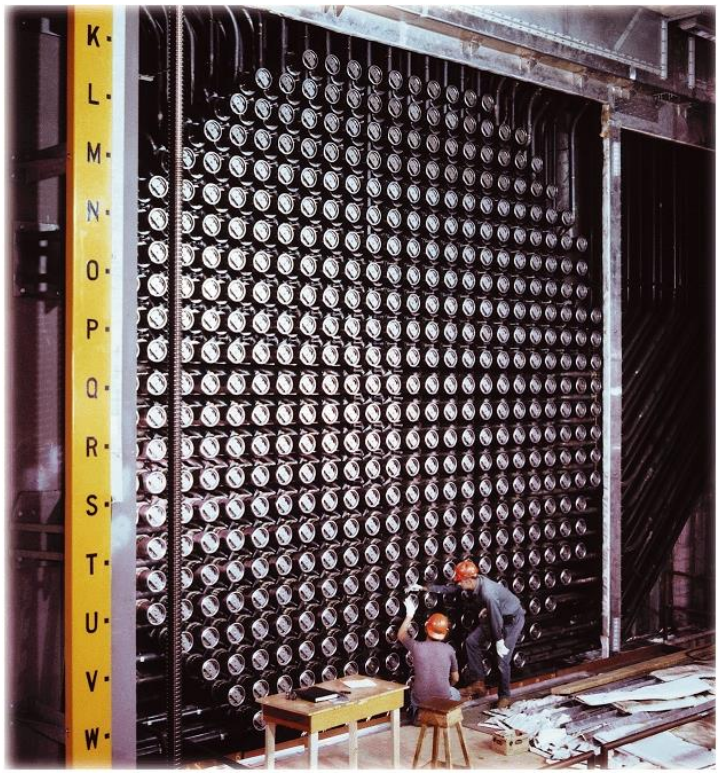

Figure 1-2. A side view of a calandria shell penetrated by hundreds of calandria tubes [19].

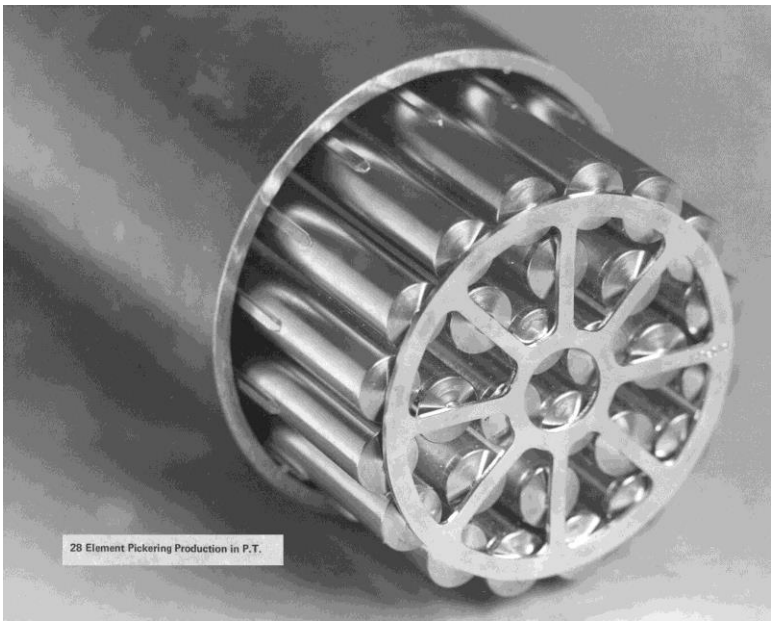

Figure 1-3. A fuel bundle inside a Zr-2.5Nb pressure tube [19].

Chapter 2 Ductile Fracture Initiation with Consideration of Strain Concentration and Stress Triaxiality near Crack Fronts in Compact Tension Specimens of Hydrided Irradiated Zr-2.5Nb Materials with Split Circumferential Hydrides

2.1 Introduction

Smith and Davies [34,35] examined the low fracture toughness of Zr-2.5Nb CANDU pressure tube material associated with the fissure formation due to microsegregation of chlorine and carbon. Scarth et al. [27] investigated the low fracture toughness of Zr-2.5Nb CANDU pressure tube material related to similar fissure structures as the result of splitting of circumferential hydrides. Sung et al. [39] investigated the crack tip stresses along the front of a crack in a compact tension (CT) specimen of unirradiated Zr-2.5Nb materials by three-dimensional finite element analyses with submodeling. Based on the computational results with the assumption of the hydride fracture stress of 750 MPa for both radial and circumferential hydrides, all radial hydrides and the circumferential hydrides in the middle portion of the specimen ahead of the crack front should fracture at the specimen load of 3,000 N. Sung et al. [40] also examined the opening strain in the ligament directly ahead of the crack front based on a thin-sliced CT model with the assumption of the plane strain conditions in the thickness direction in order to save the computational effort. The computational results indicate that with the split circumferential hydrides, the crack tip opening displacement (CTOD) can increase by 50% for thinner thin-sliced specimens under the same load per unit thickness. With the use of a strain-

Published in Engineering Fracture Mechanics, 186, pp. 208–241, 2017

based failure criterion, the load per unit thickness for thinner thin-sliced specimens with split circumferential hydrides can be reduced by at most 70% when the failure criterion is met. However, in the investigation of Sung et al. [39,40], the materials for the CT specimen and thin-sliced CT specimen were idealized as elastic perfectly plastic materials. In order to explore the effects of split circumferential hydrides on the fracture behavior of the full-sized CT specimens of irradiated materials, three-dimensional finite element analyses without and with split circumferential hydrides are needed to explore the stress and strain states in the ligament directly ahead of the crack front in a CT specimen of irradiated materials with a realistic stress-strain relation obtained from the transverse tensile tests of irradiated materials.

In this investigation, the reduced fracture toughness associated with split circumferential hydrides at room temperature is examined by conducting three-dimensional finite element analyses of CT specimens of irradiated Zr-2.5Nb materials without and with split circumferential hydrides. The stress-strain relation for the irradiated Zr-2.5Nb materials is taken as elastic plastic strain-hardening with a perfectly plastic behavior at large plastic strains based on the results of transverse tensile tests. A three-dimensional finite element analysis of a CT specimen of irradiated Zr-2.5Nb materials without circumferential hydrides is first conducted to examine the stress and strain states near the crack front in the CT specimens. Three-dimensional finite element analyses of CT specimens of irradiated Zr-2.5Nb materials with a pair of circumferential hydrides with various hydride heights and ligament thicknesses near the middle of the crack front in the CT specimen are then conducted to examine the effective plastic strains in the ligaments between the split circumferential hydrides. With a strain-based fracture criterion with consideration of stress triaxiality at a critical distance ahead of the main crack front in the full-sized CT specimen, the implications of the strain concentration in the ligaments on the fracture

toughness of the irradiated Zr-2.5Nb materials are examined and investigated. Finally, conclusions are made.

2.2 Finite Element Models

The geometry of the three-dimensional finite element models in this study is based on the geometry of the curved compact tension (CCT) specimens [12] machined from irradiated pressured tubes. Figure 2-1(a) shows a schematic of a CCT specimen without hydrides. The specimen has the thickness of 4.2 mm and the width of 17 mm. The total crack length is 8.75 mm including the fatigue crack length of 2 mm. Figure 2-1(b) shows a schematic of a CCT specimen with circumferential hydrides. The left figure in Figure 2-1(b) schematically shows a side view of the CCT specimen with a rectangular circumferential hydride. The right figure in Figure 2-1(b) schematically shows a front view of the CCT specimen with a pair of circumferential hydrides. The circumferential hydrides are assumed to have already split so that the split circumferential hydrides are considered as transverse cracks. As the first step, the curvature of the specimen and the curvature of the circumferential hydrides are not considered in this investigation so that a flat compact tension (CT) specimen and flat split circumferential hydrides are actually modeled in this study. The computational results including the effects of the curvature of the CCT specimen and the curvature of the circumferential hydrides will be presented in Chapter 4. Due to the symmetries of the CT specimen, only a quarter of a CT specimen is considered for modeling.

In order to investigate the effects of split circumferential hydrides on the fracture behavior ahead of the front of a crack in a hydrided irradiated CT specimen, submodeling was adopted to reduce unnecessary repetitive computation. The details of submodeling and the

criteria to select the sizes of the submodels were discussed in [39]. Basically, the idea of submodeling is dividing one-step simulation of a large-scale finite element model into two-step simulation with a global model describing the general characteristics of the model, and one or more sub-regions as one or more submodels catching the mechanical responses of regions of interest, of which the sizes are relatively small compared to that of the entire model.

Figure 2-2 shows the geometry of the global finite element model of a right upper quarter of a CT specimen for three-dimensional finite element analyses. The global model was partitioned to four regions of different element sizes for efficient meshing and computation. The four regions of different element sizes on the $X-Y$ plane are shown in Figures 2-3(a) and (b). The sizes and the numbers of elements for the four regions are listed in Table 2-1. The Z symmetry boundary condition was imposed on the left side surface and the Y symmetry boundary condition was imposed on the bottom surface of the global model, as shown in Figures 2-4(a) and (b). Without using transitional elements, tie constraints were used to impose the displacement continuity between the regions of different element sizes, as shown in Figure 2-4(b). Collapsed elements with the size of 12.5 μm by 12.5 μm by 25 μm in the X, Y and Z directions were placed adjacent to the crack front to induce the necessary singularity [39]. The total number of the elements for the global model is 113,763.

In order to study the effects of split circumferential hydrides with various hydride heights and ligament thicknesses on the crack initiation of the CT specimens, several submodels were built in this investigation. The size of all submodels is the same, as shown in Figure 2-5. The size is defined as that of the Region 3 of the global model based on the shape of the plastic zone from the elastic-plastic analysis of the global model [39]. The submodels were also partitioned to three regions of different element sizes. The partition of the regions of different element sizes

on the $X-Y$ plane is shown in Figures 2-6(a) and (b). The sizes and the numbers of elements for the three regions are listed in Table 2-2. Region 3 of the submodels has two sizes of elements for better computational efficiency when split circumferential hydrides were considered. The submodel boundaries, where the displacements are acquired from the analyses of the corresponding global model, and two symmetry boundary conditions are shown in Figures 2-7(a) and (b). Tie constraints were used to impose the displacement continuity between different regions, as shown in Figure 2-7(b). The right-side surface of the submodel is the only free surface. Due to the small size (5 μm by 5 μm by 5 μm) of the elements near the crack front, no collapsed element was needed in the submodels [24]. The total number of the elements for each submodel is 556,458.

Split circumferential hydrides are modeled by separating elements on the interface where the hydrides are located. A pair of split circumferential hydrides was assumed in the middle of CT specimen ahead of the crack front. Since only a quarter of a CT specimen is considered in this study, only the upper half of one split circumferential hydride is modeled. The locations of the half split circumferential hydride with three different sizes of 525 μm by 25 μm, 525 μm by 50 μm and 525 μm by 75 μm on the $X-Y$ plane are shown in Figures 2-8(a), (b) and (c), respectively. Different ligament thicknesses between split circumferential hydrides considered in this investigation are 30, 50, 100, 150, and 200 μm. These different thicknesses are simulated by controlling the location of the split circumferential hydride in the $-Z$ direction.

The irradiated Zr-2.5Nb material used in the finite element analyses is strain hardening at small plastic strains and becomes perfectly plastic at large plastic strains. The details are discussed in Appendix A. The Young's modulus is taken to be 102.1 GPa and the Poisson's ratio is taken to be 0.4. The input plastic hardening curve is shown in Figure A-3. A load P_0 of

3,206 N corresponding to K_C = 59.2 $\mathrm{MPa}\cdot\sqrt{\mathrm{m}}$ [37] based on the ASME E399 [4] is applied. It should be mentioned that K_C = 59.2 $\mathrm{MPa}\cdot\sqrt{\mathrm{m}}$ is determined from curved compact tension specimens cut from unhydrided irradiated Zr-2.5Nb pressure tubes [37]. The commercial finite element program ABAQUS was employed to perform the computations. First-order three-dimensional brick element with reduced integration (C3D8R) was used exclusively in this study since large local plastic strains are expected. The option of the geometric nonlinearity is set to off in the elastic analyses and is turned on in the elastic-plastic analyses.

2.3 Computational Results

2.3.1 Compact Tension Specimen without Split Circumferential Hydrides

Based on the submodeling strategy established in [39], two conditions should be satisfied for appropriate sets of global models and submodels. First, the mechanical behaviors near the crack front of the submodels should be similar to that of the global model. Figure 2-9 shows the consistency of the distributions of the computational J-integrals in the thickness direction of the global model and the submodel without split circumferential hydrides from the elastic analyses. In the figure, Z represents the location in the thickness direction of the CT specimen. Due to the consistency of the two distributions of J-integrals, the first condition is fulfilled. Second, the size of submodels should enclose the whole plastic zones in all elastic-plastic analyses. Figure 2-10 shows the envelope of the three-dimensional plastic zone in the submodel from the elastic-plastic analyses. The plastic zone is completely in the fine mesh region of the submodel. Based on the discussions above, this set of the global model and submodel satisfies the two conditions and is adequate for the three-dimensional finite element analyses of the quarter CT specimen. It should be noted that the unconventional shape of the three-dimensional plastic zone, which was

discussed in [39], is shown in Figure 2-10. Three cross sections a, b and c are also defined in Figure 2-10. The plastic zones in the cross sections a, b and c are shown in Figures 2-11(a), (b) and (c), respectively. As discussed in Sung et al. [39], the largest plastic zone size on the $X-Y$ plane does not occur on the free surface as shown in Figures 2-10 and 2-11. The plastic zone size and shape on the free surface (cross section c) are more similar to those in the middle of the specimen (cross section a) but with a smaller size ahead of the crack front.

The contours of the opening stress σ_{yy} and the out-of-plane normal stress σ_{zz} on the half of the crack plane ahead of the crack front are plotted in Figures 2-12 and 2-13, respectively. The radial distance r is the distance from the crack front in the X direction on the crack plane. The range of interest of r in this study is from $r = 0$ μm to $r = 125$ μm, as shown in Figures 2-12 and 2-13. In order to clearly show the magnitude of stresses ahead of the crack front, the distributions of the opening stress σ_{yy} and the out-of-plane normal stress σ_{zz} are also plotted at different radial distance r's ahead of the crack front in the thickness direction in Figures 2-14 and 2-15, respectively. As shown in Figures 2-12 and 2-14, the largest opening stress σ_{yy} occurs at about $r = 60$ μm, not adjacent to the crack front, in the middle of a CT specimen. In addition, all σ_{yy} in this region of interest is larger than the hydride fracture stress of 750 MPa [28]. The normal of the radial hydrides is parallel to the Y direction. If radial hydrides precipitate in this region of interest, all of them should fracture under this given load for crack initiation. It should be mentioned that the largest opening stress σ_{yy} is quite close to the theoretical value of $2.97\sigma_0$ (3,356 MPa), which is derived from the slip line theory for rigid perfectly plastic materials under plane strain conditions. Here, σ_0 is defined as the stress on the plateau of the input true stress-plastic strain curve (1,130 MPa), as shown in Figure A-3. This comparison suggests that the

stress state ahead of the crack front in the middle of a CT specimen is close to that of plane strain conditions for the finite element model with the given crack tip element size under the given load.

In the same region of interest, the distributions of the out-of-plane normal stress σ_{zz} has the same trend as those of σ_{yy}, as shown in Figures 2-13 and 2-15. The largest out-of-plane normal stress σ_{zz} occurs at about $r = 50$ μm, but not all σ_{zz} in this region of interest is larger than the hydride fracture stress of 750 MPa. The σ_{zz} in the zone near the free surface does not exceed 750 MPa and the width of the zone with σ_{zz} less than 750 MPa increases with r due to the free surface effect in the three-dimensional modeling, as shown in Figure 2-13. If there are circumferential hydrides, with their normal parallel to the Z direction, in this region of interest, they do not fracture near the free surface but fracture in the middle portion of a CT specimen. The general trends on the distributions of the opening stress σ_{yy} and the out-of-plane normal stress σ_{zz} and their implications to the hydride fracture, as discussed above, are also applicable at a smaller load than 3,206 N. This phenomenon of the fracture of circumferential hydrides may be observed on the fracture surface of a hydrided irradiated CCT specimen tested at room temperature, as shown in Figures 2-16 and 2-17 [36]. In Figure 2-16, on the top and the bottom parts with light color, there is no obvious woody texture. The woody texture in the middle portion may come from the ductile failure of thin ligaments between split circumferential hydrides [36]. The ductile failure of thin ligaments can be evidenced by dimples on the fracture surface in Figure 2-17, which reveals the details of the rectangular region marked in Figure 2-16. The transverse cracks due to split circumferential hydrides are marked in Figure 2-17. In this paper, the normal of the transverse cracks due to split circumferential hydrides is in the Z direction. This suggests that circumferential hydrides may not fracture in these light-colored

zones. These light-colored zones without split circumferential hydrides increase with the increasing radial distance r from the crack front, which agrees with the computational results shown in Figure 2-13.

2.3.2 Compact Tension Specimen with Split Circumferential Hydrides

Now, we consider a pair of split circumferential hydrides with various heights and ligament thicknesses ahead of the crack front near the Z symmetry plane of the quarter finite element model. The deformed meshes with the magnitudes of the effective plastic strain $\bar{\varepsilon}_p$ for the finite elements marked in colors for the radial-circumferential ($Z-Y$) plane near the Z symmetry plane at the radial distance $r = 15$ μm ahead of the crack front under 60% of the applied load of 3,206 N are shown in Figures 2-18 to 2-20 for the models with split circumferential hydrides with the total heights of 50 μm, 100 μm and 150 μm, respectively, and with different ligament thicknesses. Figures 2-18(a) to (e) show the results for the hydride height of 50 μm and the ligament thicknesses of 30, 50, 100, 150 and 200 μm, respectively. Figures 2-19(a) to (e) and Figures 2-20(a) to (e) show the corresponding results for the hydride heights of 100 μm and 150 μm, respectively. In Figures 2-18 to 2-20, the right vertical sides of the plots are the Z symmetry planes and the bottom sides of the plots are the Y symmetry planes. Note that the radial distance of $r = 15$ μm is three elements away from the crack front. The deformed meshes are also examined at $r = 50$ μm ahead of the crack front. The deformation modes of the ligaments are quite similar to those at $r = 15$ μm presented in Figures 2-18 to 2-20. In Figures 2-18 to 2-20, only the magnitudes of the effective plastic strain $\bar{\varepsilon}_p$ larger than 6.5% are marked in color. In these figures, the red color represents the regions where the effective plastic strains

are larger than 20% while the white color represents the regions where the effective plastic strains are less than 6.5%.

By comparison of Figures 2-18 to 2-20, three types of strain concentration can be identified. The type of strain concentration can be determined by the ligament thickness ratio δ which is defined as

$$\delta = \frac{t}{h} \tag{2-1}$$

where t represents the ligament thickness and h represents the hydride height. For small ligament thickness ratios with $\delta \le 1$, strain concentration occurs in the middle of the ligaments and then shear localization emanates from it, as shown in Figures 2-18(a) to (b), Figures 2-19(a) to (c) and Figures 2-20(a) to (d). For the cases of the ligament thickness t comparable to the hydride height h with $1 < \delta \le 2$, shear localization also emanates from the tip of the split circumferential hydride at the angle slightly smaller than 45 degrees with respective to the horizontal plane in addition to the strain concentration in the middle of the ligaments. Two types of shear localization emanate from different sources and then connect with each other to cross the entire ligament, as shown in Figure 2-18(c), Figures 2-19(d) to (e) and Figure 2-20(e). For large ligament thickness ratios with $\delta > 2$, shear localization emanates from the tip of the split circumferential hydride at the angle slightly smaller than 45 degrees but ends near the split circumferential hydride, as shown in Figures 2-18(d) to (e).

For the first two types of strain concentration with $\delta \le 2$, since the concentrated plastic deformation is across the entire ligament thickness, the plastic work or energy for the ligament to reach ductile fracture should be substantially smaller than that for the ligaments without large amount of strain concentration across the ligament thickness. The phenomena of strain concentration with $\delta \le 2$ are similar to those of the cumulative modes as discussed in [11] or

low energy modes discussed in [27]. For the third type of strain concentration ($\delta > 2$), since the region affected by strain concentration is relatively small, the plastic work or energy to reach ductile fracture for the entire ligament will have only a relatively small decrease. It should be noted that for the ligament thickness ratio with $\delta = 3$ in Figures 2-18(d), the strain concentration in the middle of the ligament is also moderate.

It should be noted that only the circumferential hydrides with the heights larger than 50 μm are assumed to be split [27] and considered in this investigation. With this assumption, quantification of the distribution of ligament thicknesses shows that in a hydrided irradiated Zr-2.5Nb pressure tube, almost all ligament thicknesses are less than 150 μm and most of them are less than 100 μm [21]. Based on the same assumption, the observation of hydride morphologies also shows that, in a hydrided irradiated Zr-2.5Nb pressure tube, the heights of circumferential hydrides are all larger than 50 μm and most of them are much larger than 50 μm [21]. From the discussion above, it can be concluded that in a hydrided irradiated Zr-2.5Nb pressure tube, the ligament thickness ratio δ of any adjacent circumferential hydrides is commonly no larger than 3 (with $t \le 150$ μm and $h \ge 50$ μm, and then $\delta = t/h \le 3$). Consequently, the low energy types of strain concentration ($\delta \le 3$) can be assumed to be pronounced in a hydrided irradiated Zr-2.5Nb pressure tube.

In order to consider the effect of strain concentration on the ductile fracture of ligaments, a strain-based failure criterion without consideration of stress triaxiality is first examined in this investigation. The history of the effective plastic strain $\bar{\varepsilon}_p$ at the radial distance of $r = 15$ μm ahead of the crack front in the middle of a CT specimen without hydride is plotted as a function of the normalized applied load P / P_0 with P_0 = 3,206 N in Figures 2-21 to 2-23 and these curves are marked as "No Hydride". The applied load P_0 of 3,206 N corresponds to K_C = 59.2

$\mathrm{MPa}\cdot\sqrt{\mathrm{m}}$ obtained from unhydrided irradiated curved compact tension (CCT) specimens [37]. In these figures, when the crack is initiated at $P/P_0 = 1$, the effective plastic strain $\bar{\varepsilon}_p$ is about 0.21 at the radial distance of $r = 15$ μm ahead of the crack front in the middle of a CT specimen without split circumferential hydrides. Therefore, the failure effective plastic strain $\bar{\varepsilon}_p^f = 0.21$ at the radial distance of $r = 15$ μm is chosen as the baseline failure strain for the strain-based failure criterion in this investigation.

Figures 2-21 to 2-23 also show the histories of the effective plastic strain $\bar{\varepsilon}_p$ at the radial distance of $r = 15$ μm ahead of the crack front in the middle of ligaments with split circumferential hydrides with the heights of 50, 100 and 150 μm, respectively, and the ligament thicknesses of 30, 50, 100, 150, and 200 μm. As shown in Figures 2-21 to 2-23, the material elements in the middle of ligaments at the radial distance of $r = 15$ μm with different ligament thicknesses and different hydride heights will reach the failure effective plastic strain $\bar{\varepsilon}_p^f = 0.21$ due to strain concentration earlier than the material elements in the middle of a CT specimen at the radial distance of $r = 15$ μm without split circumferential hydrides. For small ligament thickness ratios with $\delta \le 3$, the necessary fraction of the load for crack initiation to reach the failure criterion decreases to about 0.45 to 0.70, as marked by the vertical dotted lines in the figures. For large ligament thickness ratios with $\delta > 3$, the necessary fraction of the load to reach the failure effective plastic strain $\bar{\varepsilon}_p^f = 0.21$ is between 0.70 to 1.00, depending on the value of the ligament thickness ratio δ.

When the same analysis procedure as discussed earlier is followed with the material element selected at a different radial distance r such as 25 or 50 μm ahead of the crack front as the critical material element, the general trends of the normalized applied loads for crack

initiation for the CT specimens without and with hydrides are quite similar to those for the selected material elements at the radial distance of $r = 15$ μm ahead of the crack front. It should be mentioned again that the values of δ are commonly no larger than 3 in a hydrided irradiated Zr-2.5Nb pressure tube. When a hydrided irradiated CT specimen with a significant presence of randomly distributed circumferential hydrides is under an increasing load, these circumferential hydrides will first split in the middle portion of the specimen and many ligaments with different ligament thicknesses will be created near the crack front. Subsequently, low-energy and moderate strain concentration with $\delta \leq 3$ occurs in most of ligaments, and the load does not need to go to the full load to reach the failure effective plastic strain $\bar{\varepsilon}_p^f$ in most of the ligaments. Only a fraction, 0.45 to 0.70, of the applied load is needed to initiate the crack growth with many split circumferential hydrides near the crack front. The computational results may be used to explain the significant reduction of the fracture toughness at room temperature obtained from hydrided irradiated curved compact tension (CCT) specimens when compared with that from unhydrided irradiated ones as observed in [27].

As shown in Figures 2-18 to 2-20, the split circumferential hydrides give the free surfaces ahead of the crack front in the middle of the CT specimens with hydrides. The free surfaces result in strain concentration in the ligaments ahead of the crack front. This is the reason that the effective plastic strain curves for CT specimens with hydrides are higher than that for a CT specimen without hydride in Figures 2-21 to 2-23. However, the free surfaces also reduce the stress triaxiality in the ligaments ahead of the crack front. When a material element fails by void nucleation, growth and coalescence, the failure effective plastic strain is in general higher for the material element with lower stress triaxiality [5]. Therefore, the effects of the stress triaxiality

on the failure of material elements ahead of the crack fronts in CT specimens without and with hydrides should be considered.

2.4 Strain Failure Criterion with Consideration of Stress Triaxiality

For ductile fracture, the failure effective plastic strain $\bar{\varepsilon}_p^f$ depends on the stress triaxiality α [5]. The stress triaxiality α is defined as

$$\alpha = \frac{\sigma_m}{\sigma_e} \tag{2-2}$$

where σ_m $(=\sigma_{kk}/3)$ represents the hydrostatic tension, and σ_e $(=\sqrt{3\sigma'_{ij}\sigma'_{ij}/2}\,)$ is the tensile effective stress which is based on the second invariant of the deviatoric stress tensor σ'_{ij} ($=\sigma_{ij}-\sigma_{kk}\delta_{ij}/3$). When the stress triaxiality α is large, the ductile fracture process is governed by void nucleation, growth and coalescence, and the failure effective plastic strain $\bar{\varepsilon}_p^f$ decreases with increasing stress triaxiality α [5]. In Bao and Wierzbicki [5], the failure effective plastic strain $\bar{\varepsilon}_p^f$ was presented as a function of the stress triaxiality α based on the experimental and computational results for aluminum alloy 2024-T351. However, the failure effective plastic strain $\bar{\varepsilon}_p^f$ as a function of the stress triaxiality α for irradiated Zr-2.5Nb materials based on the experimental and computational results is not available.

The computational results on the states of the stress triaxiality ahead of crack front for a CT specimen without hydride and a CT specimen with hydrides are presented in Appendix B. As shown in Figures B-3 to B-5, the values of the stress triaxiality α are larger than 0.7 ahead of the crack front during the most deformation histories. The failure of irradiated Zr-2.5Nb materials with hydrides ahead of the crack front is ductile as shown from the dimpled fracture

surface in Figure 2-17. Since the stress triaxiality is quite high ahead of the crack front and the fracture of irradiated Zr-2.5Nb materials is ductile, a phenomenological macroscopic void growth model based on the Gurson yield function [17] is adopted here to model the effects of void growth on ductile fracture in order to develop the failure effective plastic strain $\bar{\varepsilon}_p^f$ as a function of the stress triaxiality α for irradiated Zr-2.5Nb materials to model the fracture initiation in the CT specimens without and with hydrides. The details for the development the governing equations of the Gurson model to determine the failure strains of irradiated Zr-2.5Nb materials is presented in Appendix C.

In order to better visualize the effect of the stress triaxiality α on the failure effective plastic strain $\bar{\varepsilon}_p^f$, $\bar{\varepsilon}_p^f$ as a function of α under constant α conditions with the selection of the initial void volume fraction $f_0 = 0.03$ and the failure void volume fraction $f_f = 0.113$ based on the governing equations of the Gurson model presented in Appendix C is shown in Figure 2-24. In order to compare the results of the Gurson model approach presented in Appendix C with those of the average stress triaxiality approach of Bao and Wierzbicki [5], an average stress triaxiality $\bar{\alpha}$ defined by Bao and Wierzbicki [5] is adopted here as

$$\bar{\alpha} = \frac{1}{\bar{\varepsilon}_p^f} \int_0^{\bar{\varepsilon}_p^f} \alpha \, d\bar{\varepsilon}_p \tag{2-3}$$

With this definition of the average stress triaxiality $\bar{\alpha}$, the failure effective plastic strain $\bar{\varepsilon}_p^f$ of 0.634 for the critical center element in the transverse tensile tests for the average stress triaxiality $\bar{\alpha}$ of 0.603 can be determined and then plotted as a solid square symbol in Figure 2-24 based on the experimental results and the three-dimensional finite element analyses of the transverse tensile tests as detailed in Appendix D. The average stress triaxiality $\bar{\alpha}$ at the radial distance of $r = 15$ μm ahead of the crack front in the CT specimen without hydride can be determined as

1.766 when the effective tensile plastic strain $\bar{\varepsilon}_p^f$ reaches the failure effective plastic strain of 0.21 at K_C. The lower failure effective plastic strain $\bar{\varepsilon}_p^f$ of 0.21 for the higher average stress triaxiality $\bar{\alpha}$ of 1.766 is also shown as the solid triangular symbol in Figure 2-24. As shown in Figure 2-24, the results of the Gurson model approach presented in Appendix C and the average stress triaxiality approach of Bao and Wierzbicki [5] are consistent with each other to correlate to the fracture initiation in the CT specimens without hydride. As shown in Figure 2-24, the failure effective plastic strain $\bar{\varepsilon}_p^f$ as a function of the stress triaxiality α based on the Gurson model can be correlated to the transverse tensile test results and the fracture initiation for the CT specimen without hydride at K_C. The general trend of the curve for the failure effective plastic strain $\bar{\varepsilon}_p^f$ as a function of the stress triaxiality α for irradiated Zr-2.5Nb materials is quite similar to that for aluminum alloy 2024-T351 shown in Bao and Wierzbicki [5].

2.5 Reduction of Frature Initiation Load Due to Split Circumferential Hydrides

The failure effective plastic strain $\bar{\varepsilon}_p^f$ can now be calculated from the given stress triaxiality history $\alpha(\bar{\varepsilon}_p)$ at the radial distance of $r = 15$ μm ahead of the crack front in CT specimens with split circumferential hydrides with the heights of 50, 100 and 150 μm and different ligament thicknesses based on the Gurson model approach. The material stress-strain curve $\sigma_f(\bar{\varepsilon}_p)$ and the stress triaxiality history $\alpha(\bar{\varepsilon}_p)$ during the increasing effective plastic strain $\bar{\varepsilon}_p$ are tracked to obtain the failure effective plastic strain $\bar{\varepsilon}_p^f$ to grow from the initial volume fraction $f_0 = 0.03$ to the failure void volume fraction $f_f = 0.113$ based on the governing equations of the Gurson model derived and presented in Appendix C. The average stress triaxiality approach of Bao and Wierzbicki [5] is also used to determine the failure effective

plastic strain $\bar{\varepsilon}_p^f$ based on the curve for the failure effective plastics strain $\bar{\varepsilon}_p^f$ as a function of the stress triaxiality α obtained from the Gurson model shown in Figure 2-24. The results based on the two approaches for the fracture initiation loads for CT specimens with split circumferential hydrides are quite similar and only the results based on the Gurson model are presented in Figures 2-25 to 2-27. The values of the failure effective plastic strain $\bar{\varepsilon}_p^f$ are marked by the crosses for CT specimens with hydrides with the heights of 50, 100 and 150 μm and different ligament thicknesses in Figures 2-25 to 2-27, respectively.

As shown in Figures 2-25 to 2-27, the material elements in the middle of ligaments at the radial distance of $r = 15$ μm in the middle of CT specimens with hydrides with different ligament thicknesses and different heights will achieve the failure effective plastic strain $\bar{\varepsilon}_p^f$ earlier than the material element at the radial distance of $r = 15$ μm in the middle of CT specimens without hydride due to different types of strain concentration as discussed earlier. Based on the values of the failure effective plastic strain $\bar{\varepsilon}_p^f$ obtained from the governing equations of the Gurson model for the cases with $\delta \le 3$, the necessary fraction of the normalized load for crack initiation to reach the values of the failure effective plastic strain $\bar{\varepsilon}_p^f$ decreases to 0.60 to 0.70. The normalized loads from 0.60 to 0.70 to reach the failure criterion are higher than those based on the failure criterion without consideration of stress triaxiality as presented in Figures 2-21 to 2-23 due to larger failure effective plastic strains for the low stress triaxiality of the critical material elements in ligaments with small thicknesses of 30 and 50 μm. This is the main reason that a strain-based failure criterion with consideration of stress triaxiality is needed for the fracture initiation analysis where the constraint conditions change from the nearly plane strain conditions in CT specimens without hydride to the nearly plane stress conditions in the

ligaments between split circumferential hydrides. For the cases with $\delta > 3$, the necessary fraction of the load for crack initiation to reach the failure effective plastic strain $\bar{\varepsilon}_p^f$ is between 0.70 to 1.00, depending on the value of the ligament thickness ratio δ. It should be mentioned again that the values of the ligament thickness ratio δ are commonly no larger than 3 in a hydrided irradiated Zr-2.5Nb pressure tube. As shown in Figures 2-25 to 2-27, the computational results with consideration of stress triaxiality can be used to explain the near 35% reduction of the fracture toughness at room temperature obtained from hydrided irradiated curved compact tension (CCT) specimens when compared with that obtained from unhydrided irradiated ones [27].

When the same analysis procedure is followed with the material element selected at a different radial distances of 10 μm ahead of the crack front as the critical material element, the curve of the failure effective plastics strain $\bar{\varepsilon}_p^f$ as a function of the stress triaxiality α will still be fitted by the experimental/computational results of the transverse tensile tests and the effective plastic strain $\bar{\varepsilon}_p$ at the critical material element, and the curve will be higher than that shown in Figure 2-24 for larger values of the stress triaxiality α. However, the general trends of the normalized applied loads for fracture initiation for the CT specimens with hydrides are quite similar to those for the selected material element at the radial distance of $r = 15$ μm ahead of the crack front as presented in this paper.

2.6 Conclusions

In this study, simulations of CT specimens without and with split circumferential hydrides were conducted with a quarter finite element model using the submodeling technique. The choices of the mesh sizes and geometric sizes of the global model and the submodels follow

the guidelines established in [39]. For a CT specimen without split circumferential hydrides, the distributions of the opening stress σ_{yy} and the out-of-plane normal stress σ_{zz} on the half crack plane ahead of the crack front are obtained. The computational results show that in the middle of the specimen, the largest opening stress σ_{yy} and the largest out-of-plane normal stress σ_{zz} occur at the radial distances of about $r = 60$ μm and $r = 50$ μm, respectively, not adjacent to the crack front under the given load. The largest opening stress σ_{yy} is quite close to the theoretical value derived from the slip line theory for rigid perfectly plastic materials under plane strain conditions. This means that the stress state near the middle portion of the crack front is close to that of the plane strain conditions under the given load. With the hydride fracture stress of 750 MPa, the distributions of the opening stress σ_{yy} and the out-of-plane normal stress σ_{zz} show that all radial hydrides ahead of the crack front will fracture, and circumferential hydrides ahead of the crack front split in the middle portion of specimen but they do not split near the free surface. The size of the zone without split circumferential hydrides increases with the increasing radial distance r from the crack front.

For CT specimens with split circumferential hydrides with various heights and ligament thicknesses, strain concentration is observed in the middle of the ligaments when the ratio of the ligament thickness to the hydride height less than 3. A strain-based failure criterion with consideration of stress triaxiality is developed using the Gurson yield model with two fitting parameters of the initial void volume fraction f_0 and the failure void volume fraction f_f. The two fitting parameters are determined by the failure engineering plastic strain of the transverse tensile tests and the failure effective plastic strain for the material element at $r = 15$ μm ahead of the crack front in the CT specimen without hydride at K_C. With the strain-based failure

criterion with consideration of stress triaxiality, the necessary fraction of the load for crack initiation is about 0.60 to 0.70 to fracture the ligaments with low plastic work or energy types of strain concentration. The results suggest that low plastic work or energy types of strain concentration in ligaments are pronounced in a hydrided irradiated Zr-2.5Nb pressure tube. The computational results suggest that only 60% to 70% of the load for crack initiation of an unhydrided irradiated CT specimen is needed to fracture a hydrided irradiated CT specimen with many randomly distributed split circumferential hydrides near the crack front. The computational results can be used to explain the near 35% reduction of the fracture toughness at room temperature obtained from hydrided irradiated curved compact tension (CCT) specimens when compared with that from unhydrided irradiated ones.

Acknowledgement

The support of this work from CANDU Owners Group is greatly appreciated. Helpful discussions with Sterling St Lawrence and Brian Leitch of Chalk River Laboratories are also greatly appreciated. In addition, the authors appreciate the two fractographs from a hydrided irradiated Zr-2.5Nb specimen provided by Sterling St Lawrence of Chalk River Laboratories.

Table 2-1. Sizes and numbers of elements for the four regions of the three-dimensional global finite element model.

Region of global model	Element size in the X, Y and Z directions (μm)	Number of elements
Region 1	500x500x500	3,765
Region 2	100x100x100	20,412
Region 3	50x50x50	41,034
Region 4	25x25x25	48,552

Table 2-2. Sizes and numbers of elements for the three regions of the three-dimensional submodels.

Region of submodel	Element size in the X, Y and Z directions (μm)	Number of elements
Region 1	50x50x50	36,666
Region 2	25x25x25	74,592
Region 3	5x5x5, 25x5x5	445,200

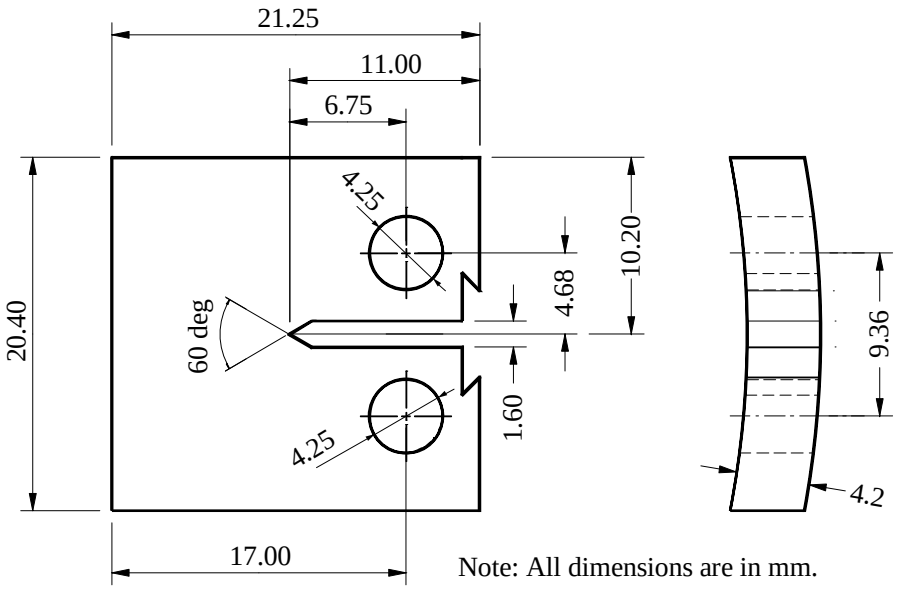

(a)

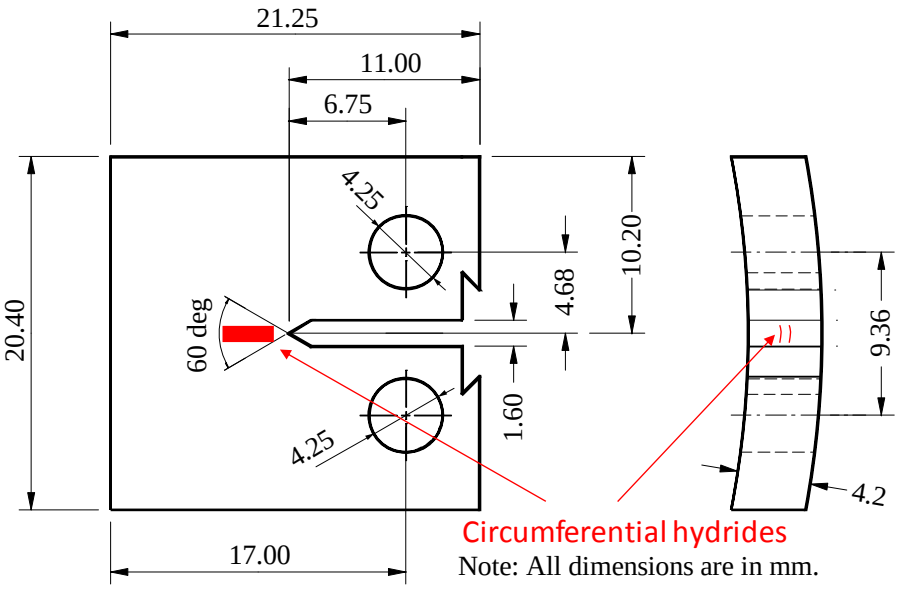

(b)

Figure 2-1. Schematics of a curved compact tension (CCT) specimen (a) without and (b) with circumferential hydrides. The CCT specimen has a fatigue crack with a length of 2 mm ahead of the notch tip.

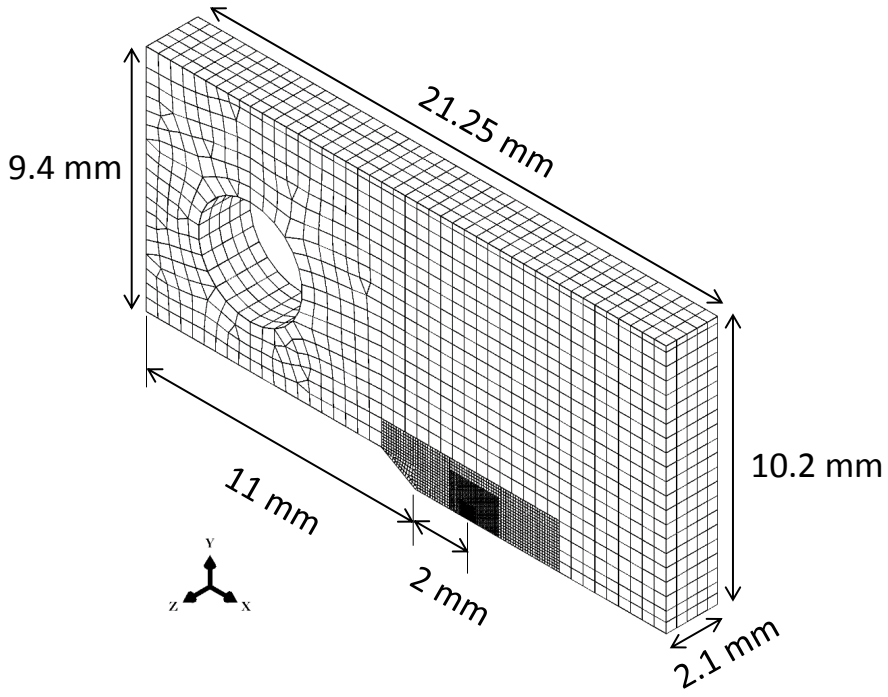

Figure 2-2. Geometry of the three-dimensional global finite element model of a quarter of a CT specimen.

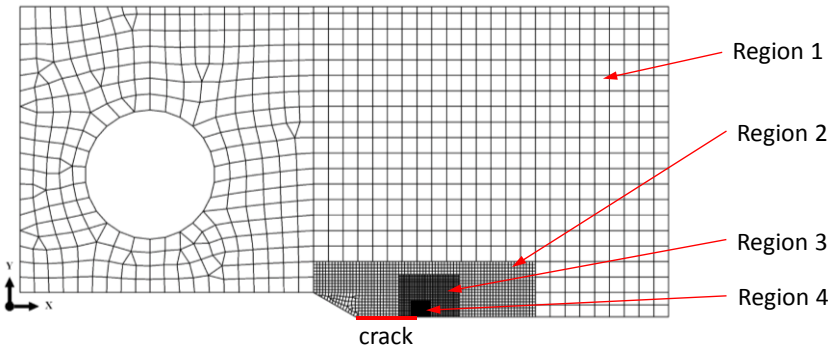

(a)

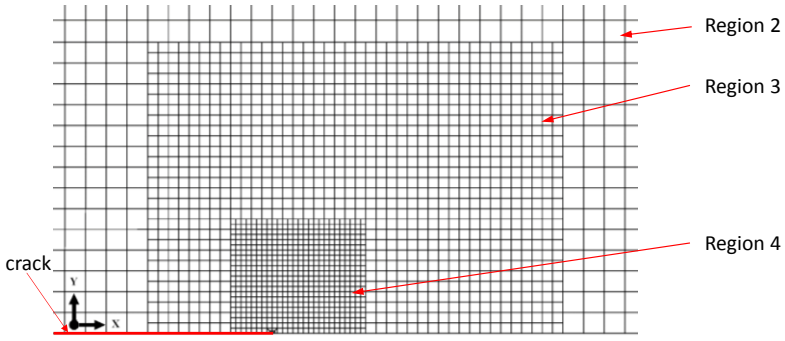

(b)

Figure 2-3. Partition of the regions of different element sizes on the $X-Y$ plane of the global model.

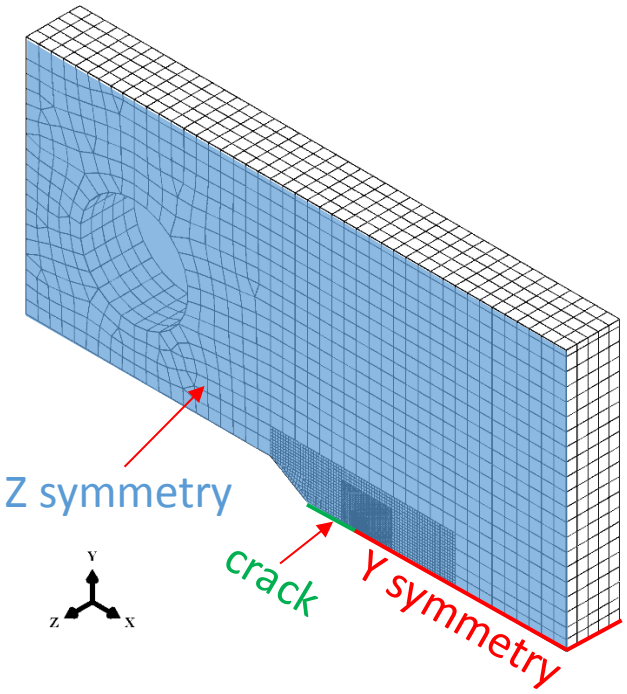

(a)

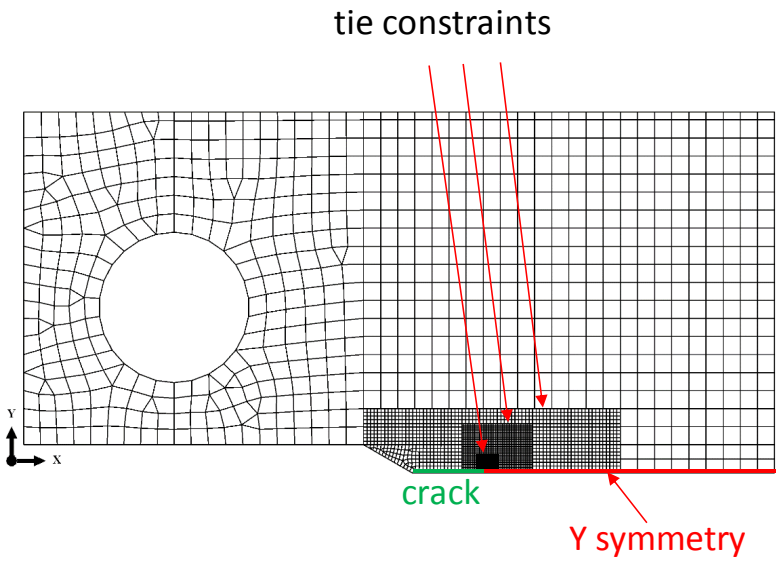

(b)

Figure 2-4. Boundary and constraint conditions of the three-dimensional global finite element model.

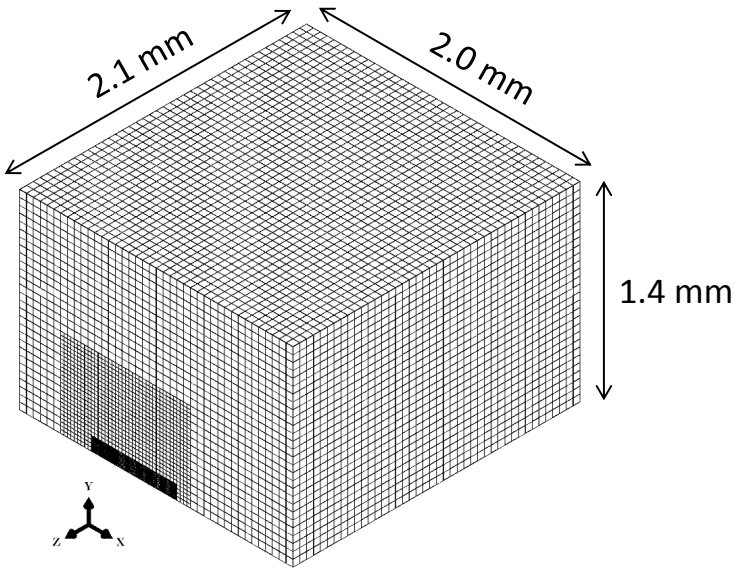

Figure 2-5. Geometry of the submodels of a quarter of a CT specimen.

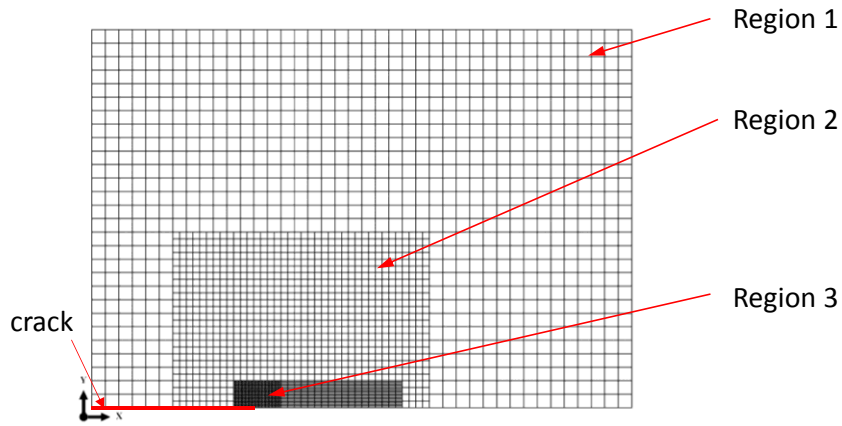

(a)

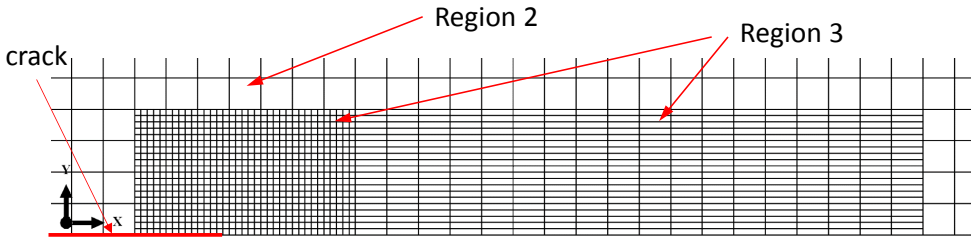

(b)

Figure 2-6. Partition of the regions of different element sizes on the $X-Y$ plane of the submodels.

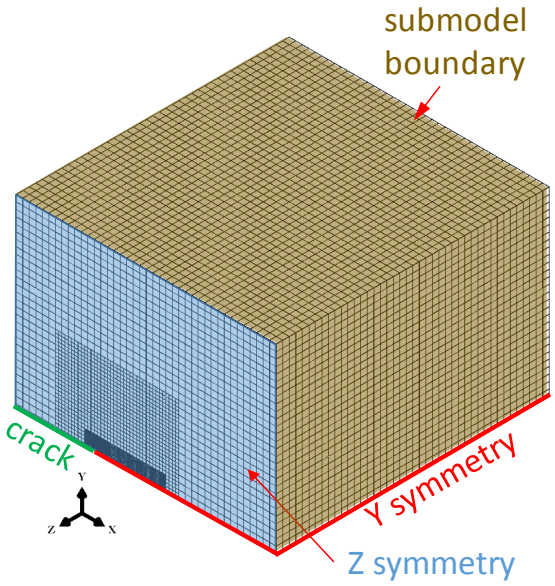

(a)

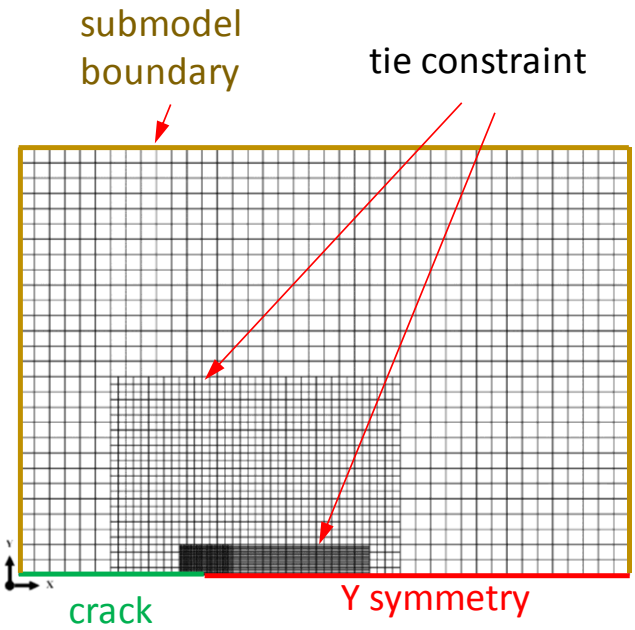

(b)

Figure 2-7. Boundary and constraint conditions of the three-dimensional submodels.

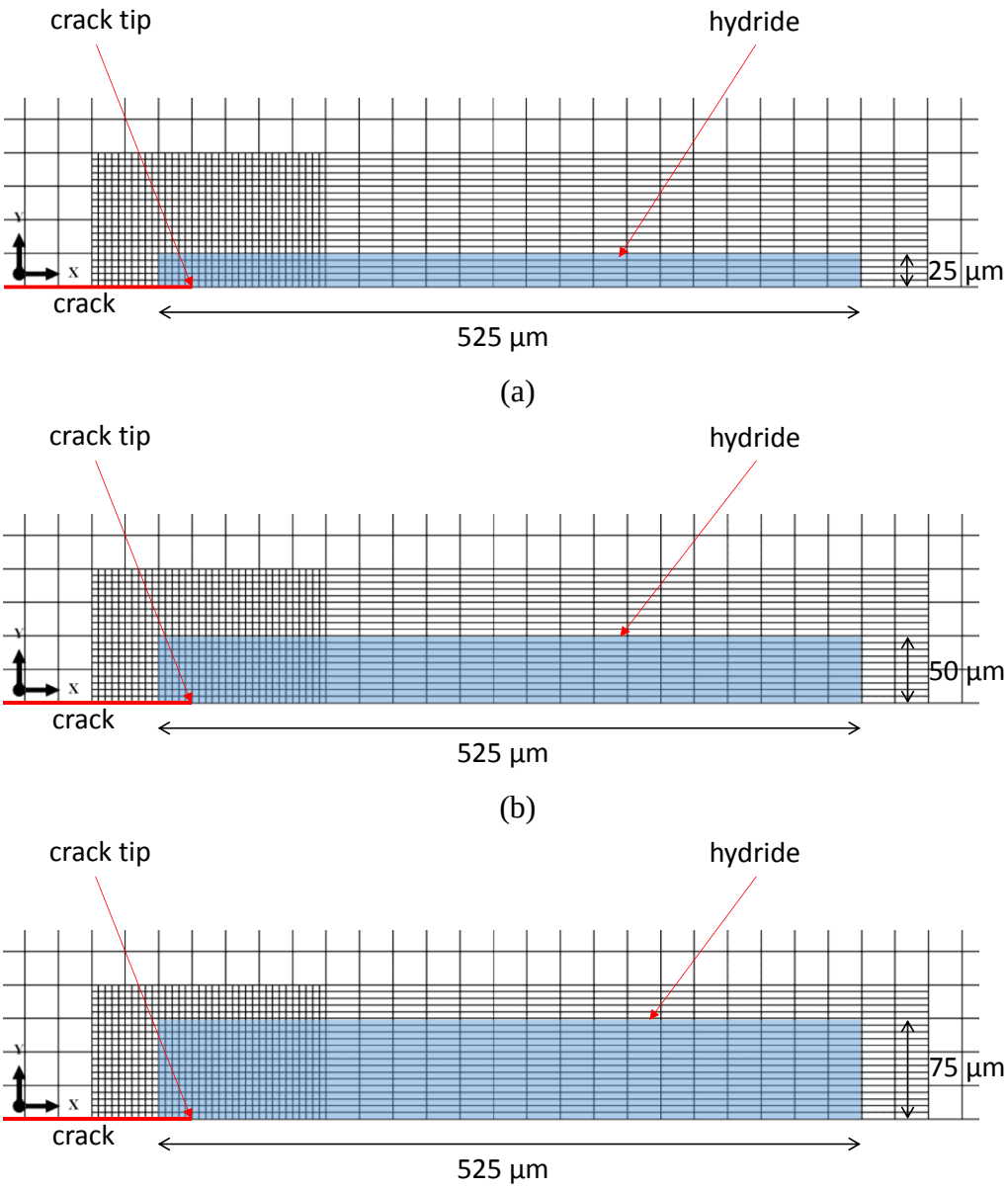

Figure 2-8. The positions and the sizes of split circumferential hydrides with different hydride heights on the $X-Y$ plane in the submodels. (a) 50 µm; (b) 100 µm; (c) 150 µm.

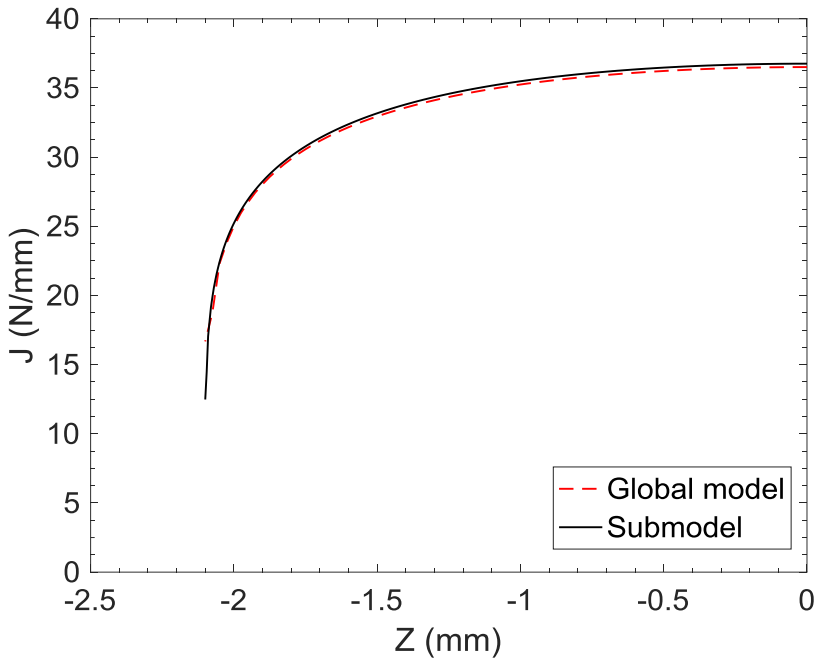

Figure 2-9. The distributions of the computational J-integrals of the global model and the submodel without split circumferential hydrides.

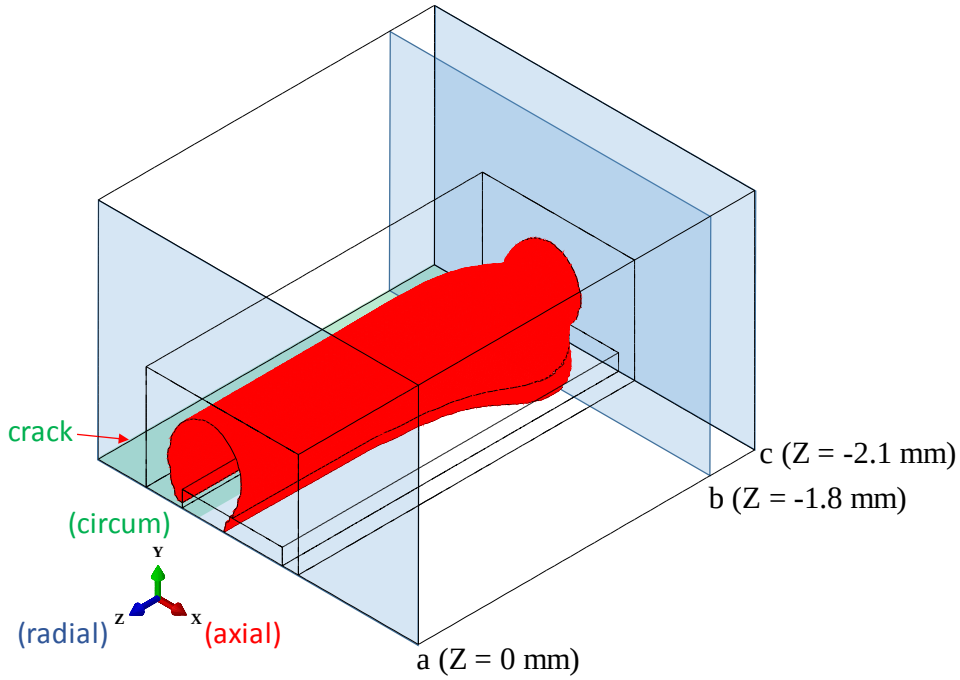

Figure 2-10. The envelope surface of the three-dimensional plastic zone of the submodel without split circumferential hydrides and the locations of three cross sections a, b and c.

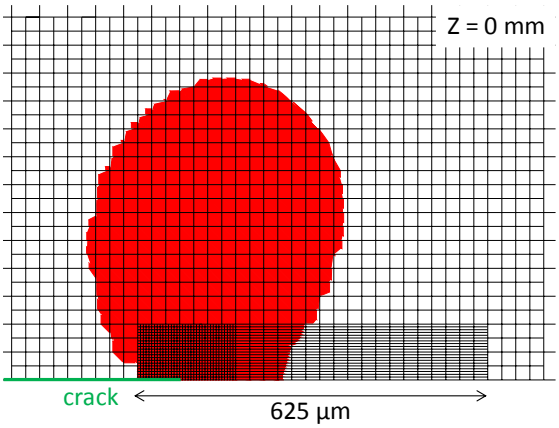

(a)

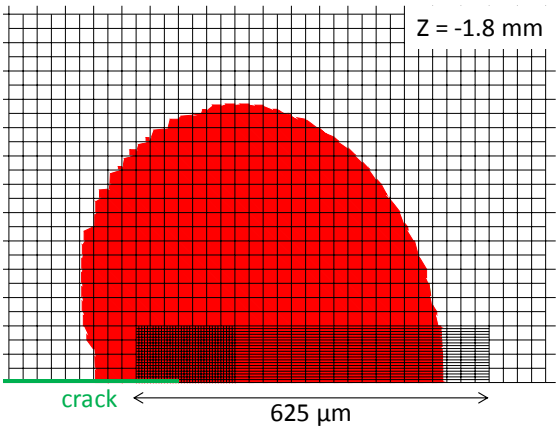

(b)

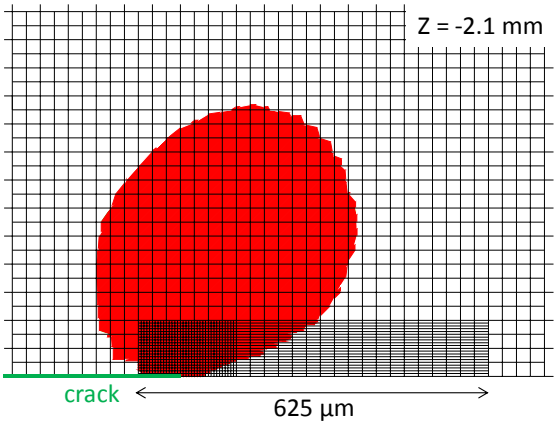

(c)

Figure 2-11. The plastic zones in three cross sections a, b, and c. (a) Cross section a, (b) cross section b, and (c) cross section c.

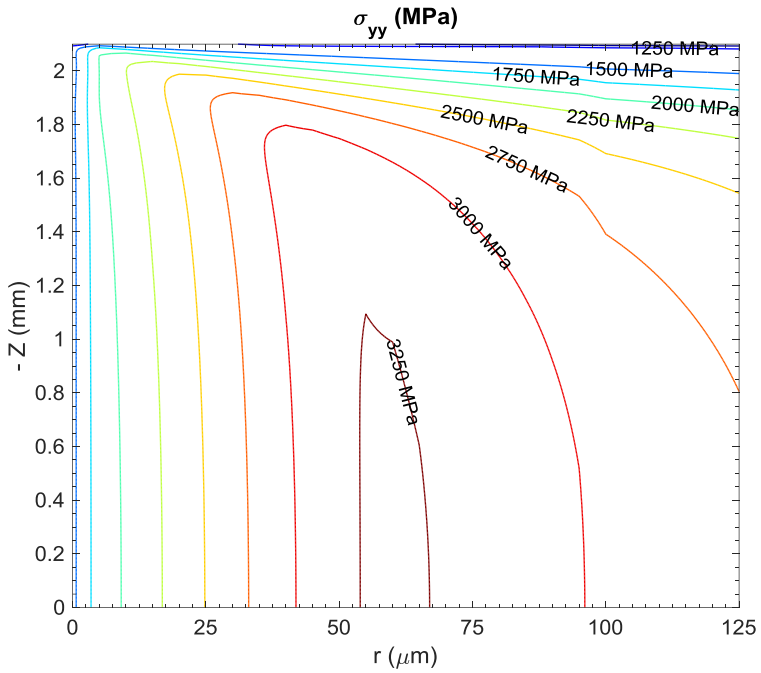

Figure 2-12. The contours of the opening stresses σ_{yy} on the half crack plane ahead of the crack front.

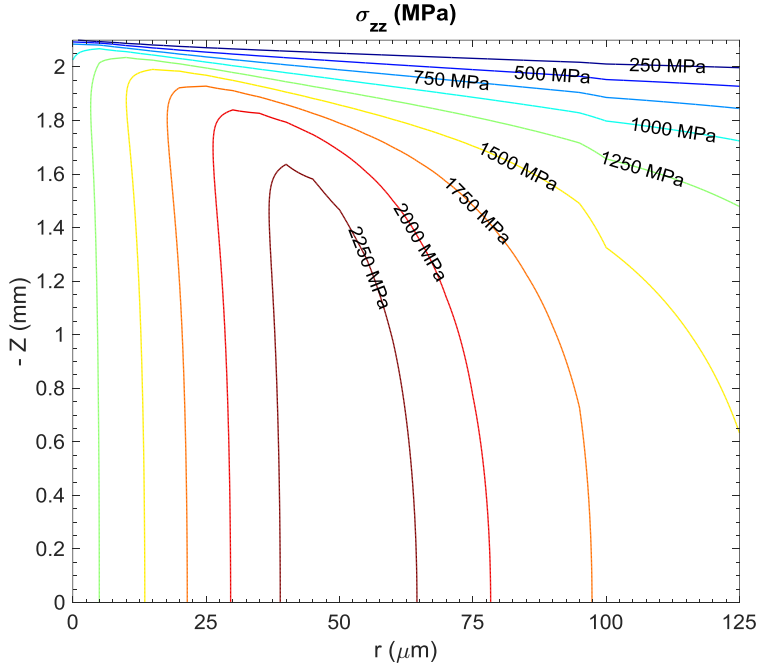

Figure 2-13. The contours of the out-of-plane normal stresses σ_{zz} on the half crack plane ahead of the crack front.

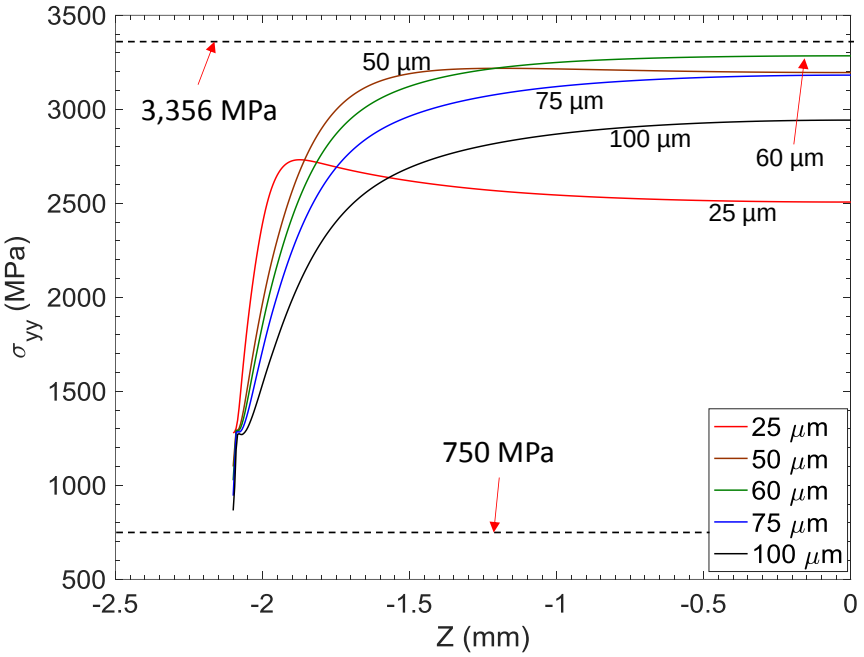

Figure 2-14. The distributions of the opening stresses σ_{yy} at different r's in the thickness direction (Z) ahead of the crack front.

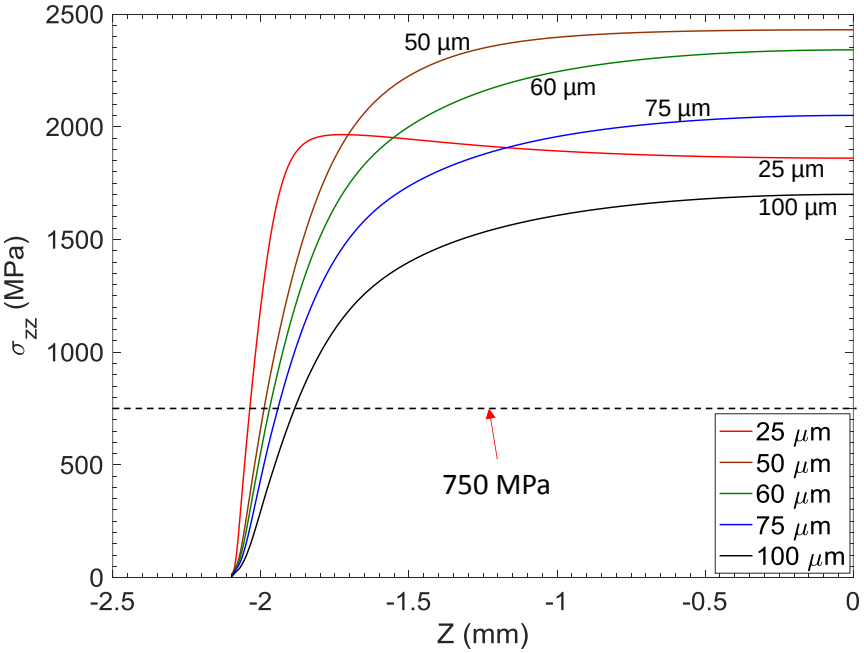

Figure 2-15. The distributions of the out-of-plane normal stresses σ_{zz} at different r's in the thickness direction (Z) ahead of the crack front.

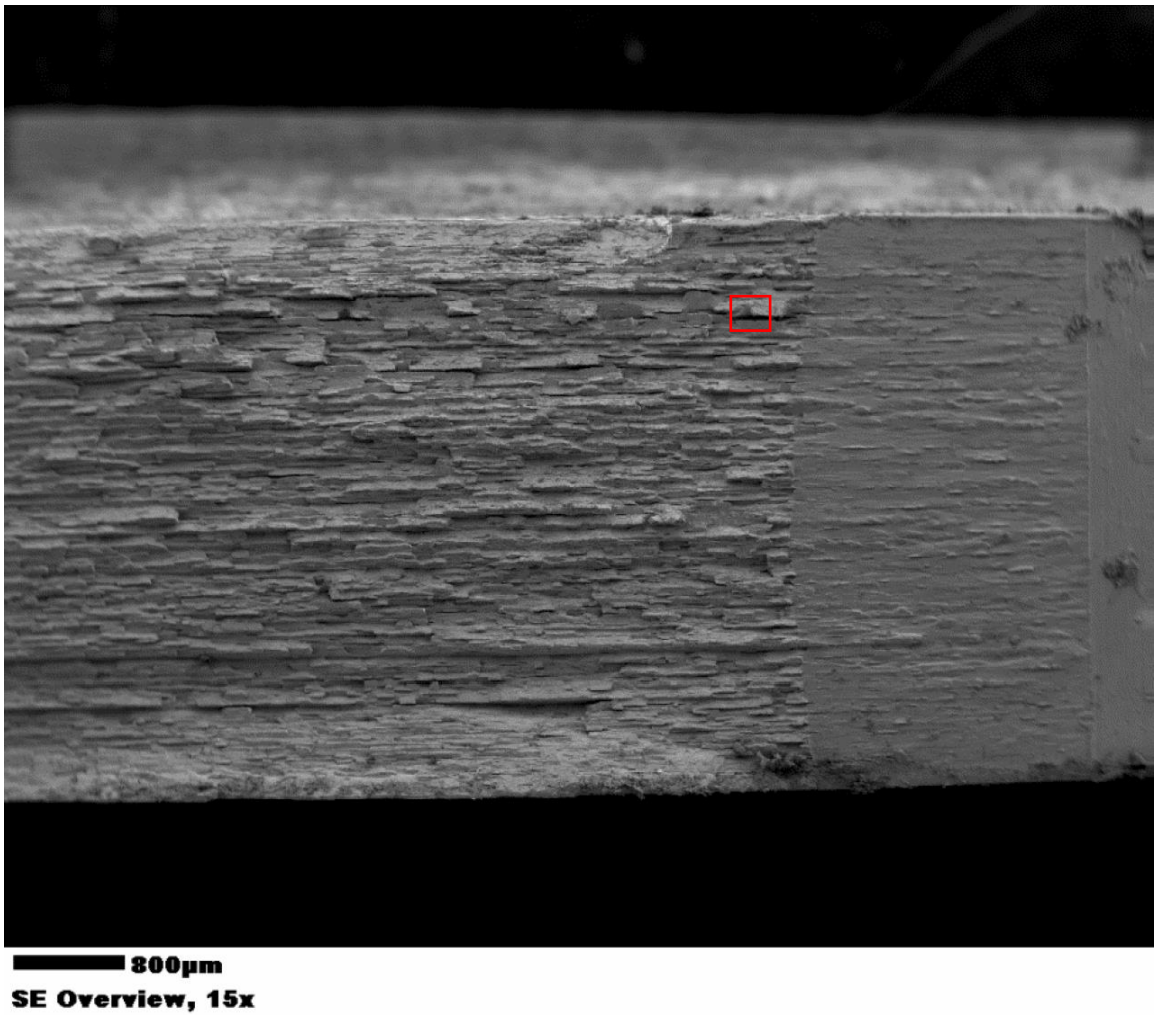

Figure 2-16. A SEM picture of the fracture surface of a hydrided irradiated curved compact tension (CCT) specimen at room temperature.

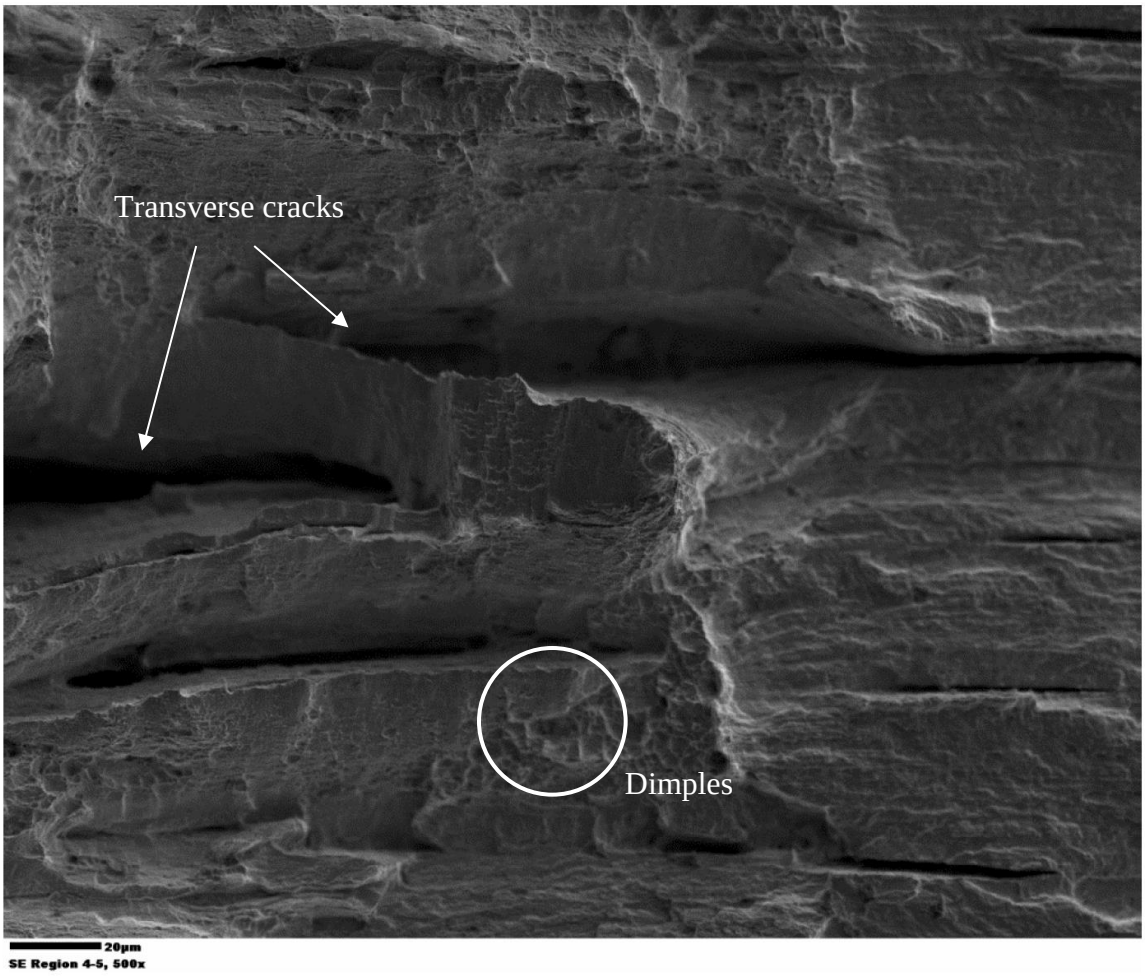

Figure 2-17. A magnified picture of the fracture surface of a hydrided irradiated curved compact tension (CCT) specimen at room temperature.

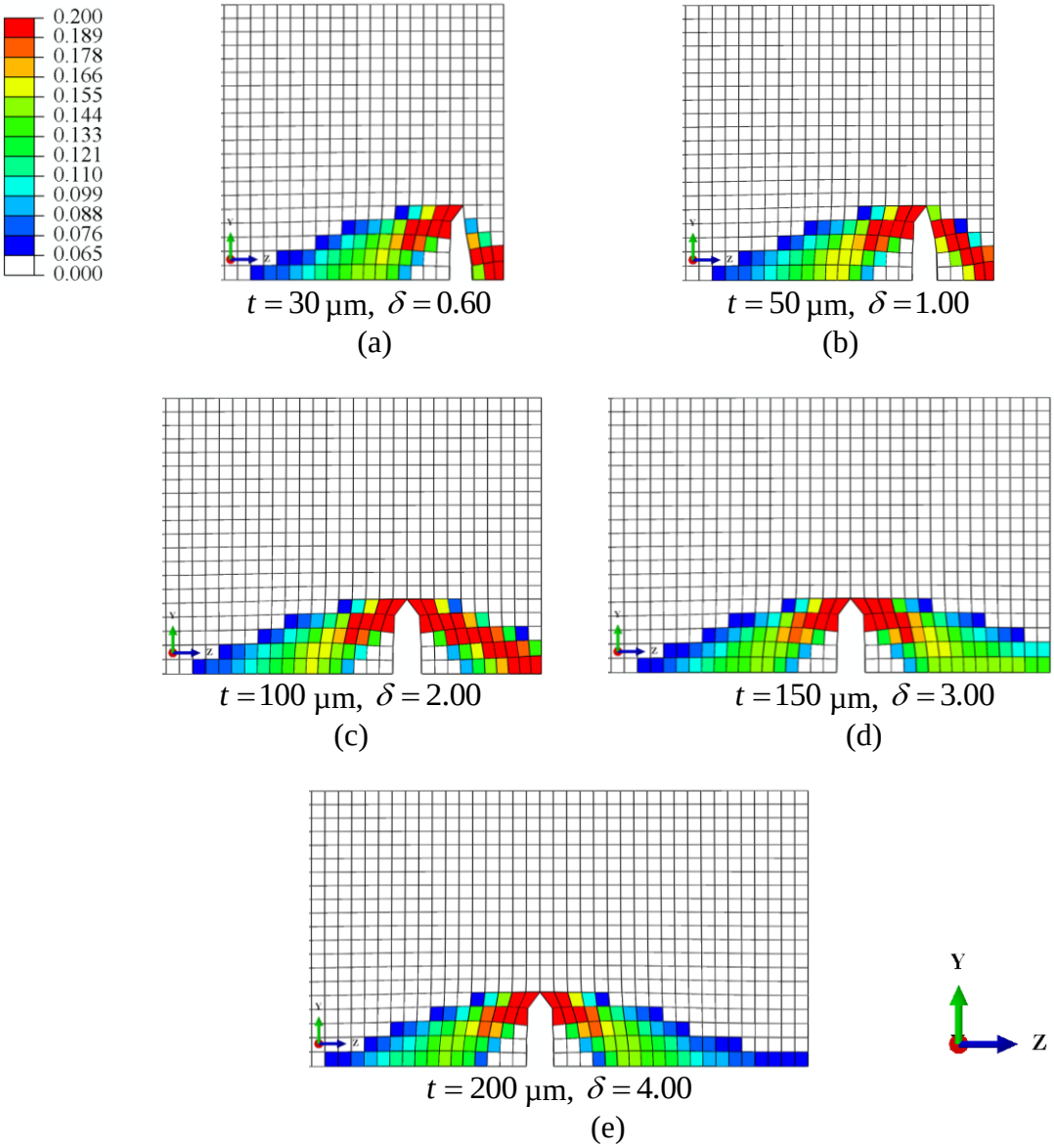

Figure 2-18. The deformed meshes with the magnitudes of the effective plastic strain $\bar{\varepsilon}_p$ for the finite elements marked in colors for the radial-circumferential plane near the Z symmetry plane at the radial distance $r = 15$ μm ahead of the crack front for the CT specimens with hydrides with the height of 50 μm under a half of the applied load of 3,206 N. The ligament thicknesses are (a) 30 μm, (b) 50 μm, (c) 100 μm, (f) 150 μm, and (e) 200 μm.

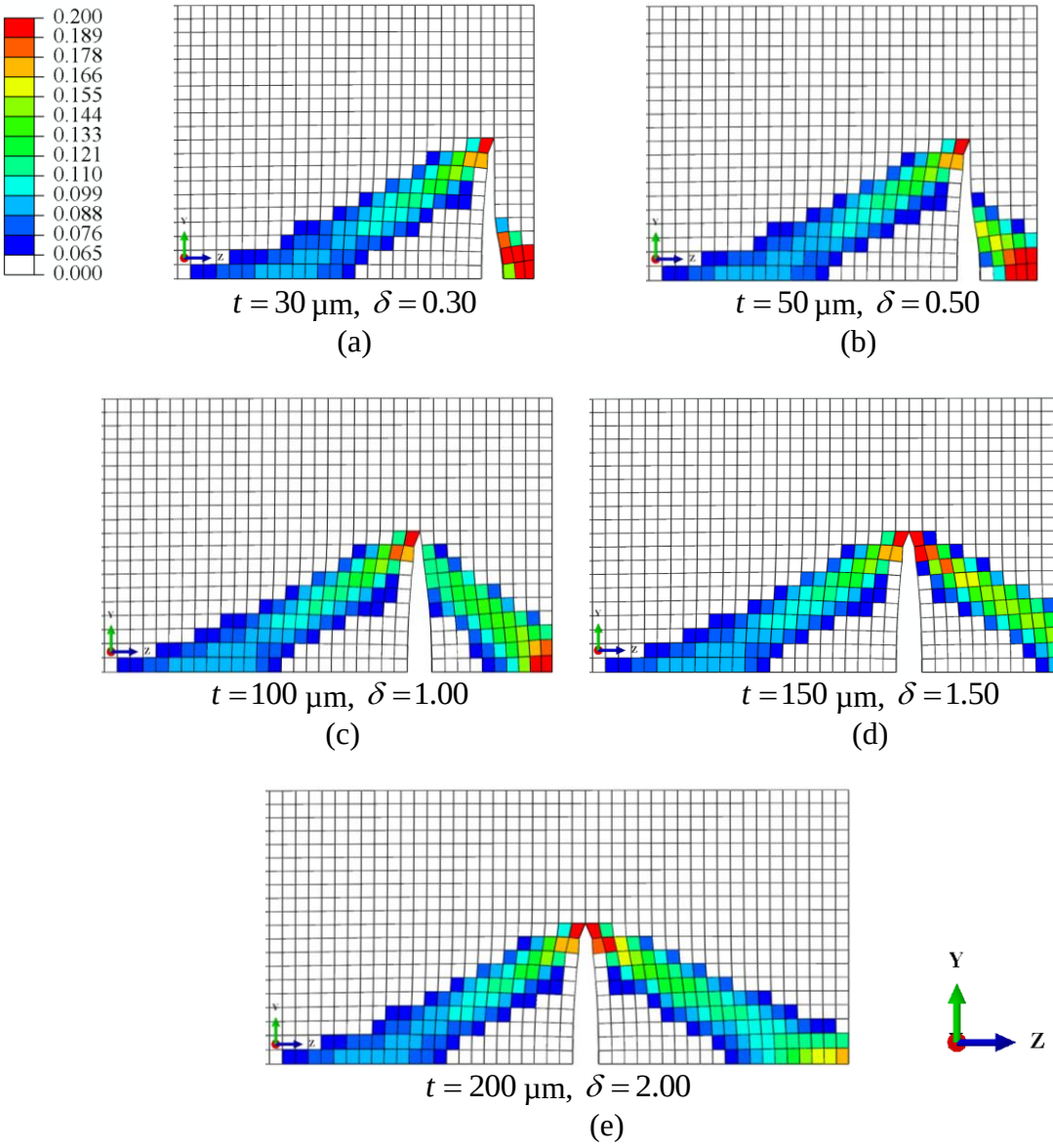

Figure 2-19. The deformed meshes with the magnitudes of the effective plastic strain $\bar{\varepsilon}_p$ for the finite elements marked in colors for the radial-circumferential plane near the Z symmetry plane at the radial distance $r = 15$ μm ahead of the crack front for the CT specimens with hydrides with the height of 100 μm under a half of the applied load of 3,206 N. The ligament thicknesses are (a) 30 μm, (b) 50 μm, (c) 100 μm, (f) 150 μm, and (e) 200 μm.

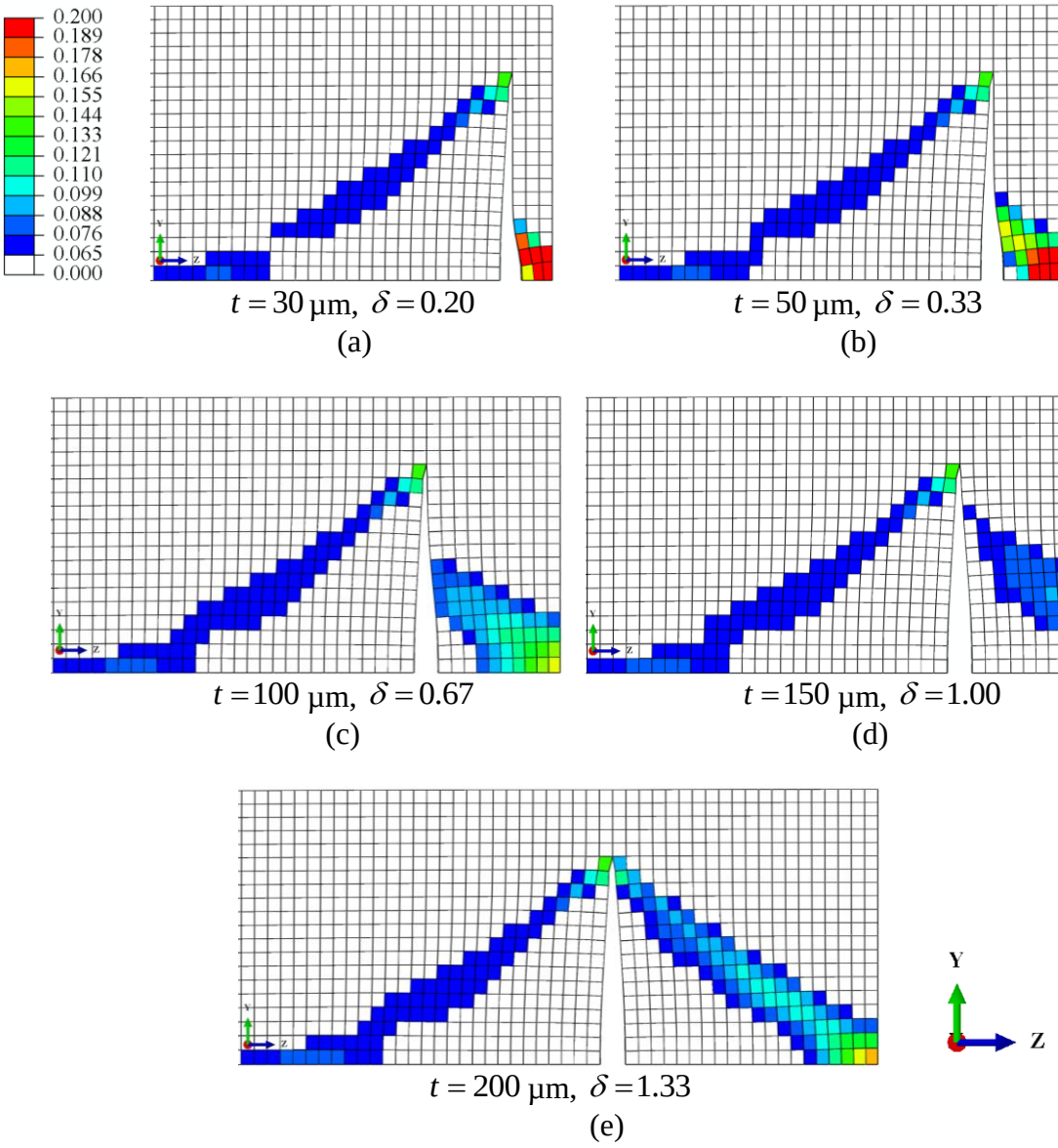

$t = 30$ μm, $\delta = 0.20$
(a)

$t = 50$ μm, $\delta = 0.33$
(b)

$t = 100$ μm, $\delta = 0.67$
(c)

$t = 150$ μm, $\delta = 1.00$
(d)

$t = 200$ μm, $\delta = 1.33$
(e)

Figure 2-20. The deformed meshes with the magnitudes of the effective plastic strain $\bar{\varepsilon}_p$ for the finite elements marked in colors for the radial-circumferential plane near the Z symmetry plane at the radial distance $r = 15$ μm ahead of the crack front for the CT specimens with hydrides with the height of 150 μm under a half of the applied load of 3,206 N. The ligament thicknesses are (a) 30 μm, (b) 50 μm, (c) 100 μm, (f) 150 μm, and (e) 200 μm.

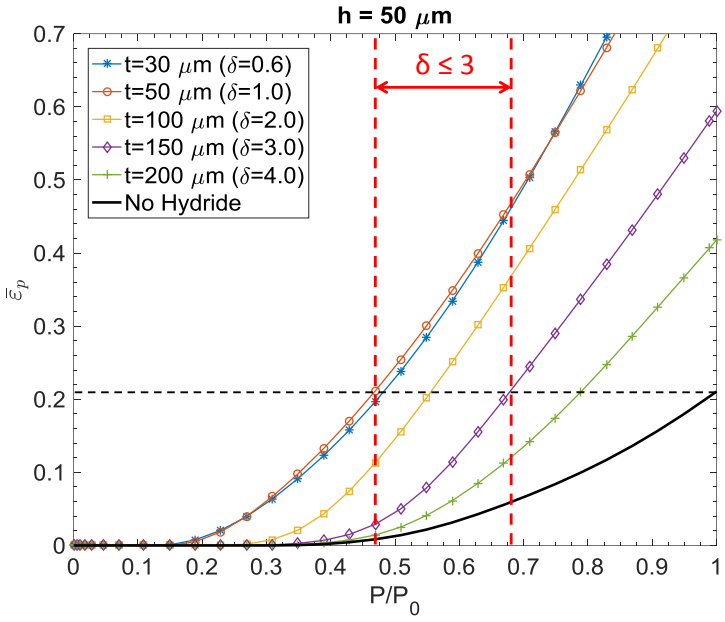

Figure 2-21. The histories of the effective plastic strain $\bar{\varepsilon}_p$ at the radial distance of $r = 15$ μm plotted as functions of the normalized applied load P/P_0 for a CT specimen without hydride and CT specimens with split circumferential hydrides with the height of 50 μm and different ligament thicknesses.

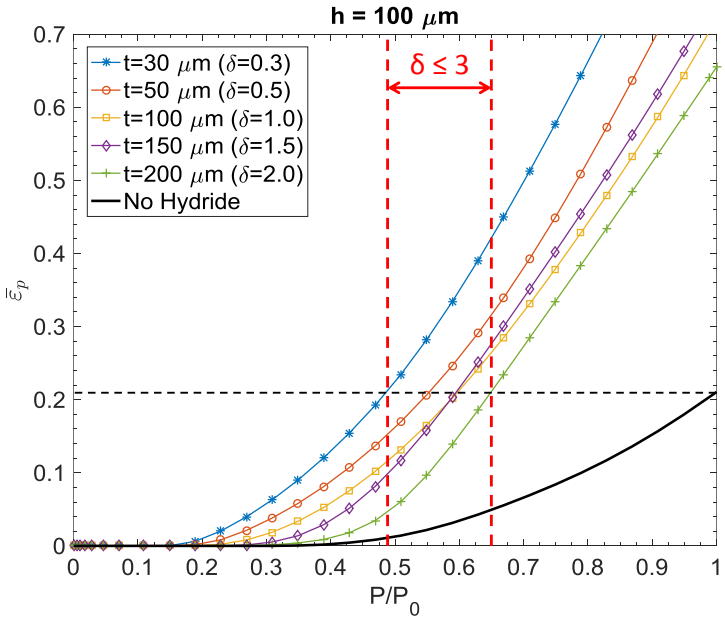

Figure 2-22. The histories of the effective plastic strain $\bar{\varepsilon}_p$ at the radial distance of $r = 15$ μm plotted as functions of the normalized applied load P/P_0 for a CT specimen without hydride and CT specimens with split circumferential hydrides with the height of 100 μm and different ligament thicknesses.

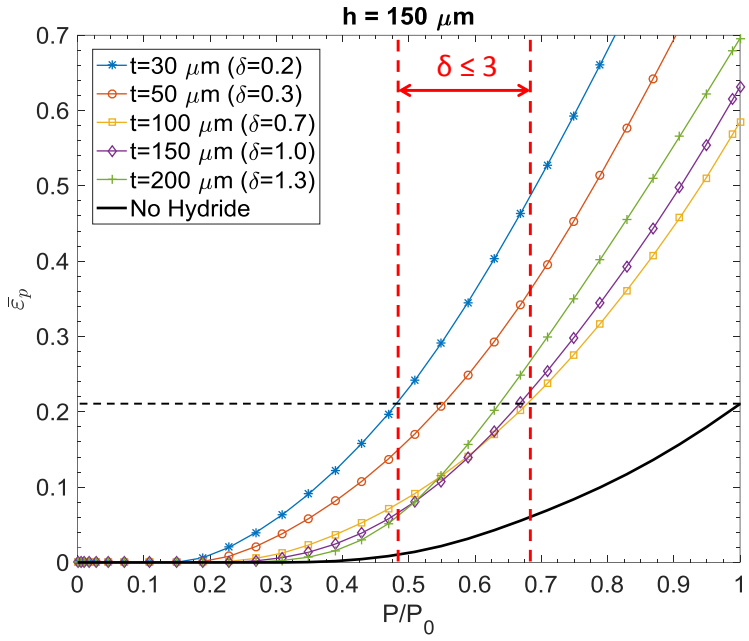

Figure 2-23. The histories of the effective plastic strain $\bar{\varepsilon}_p$ at the radial distance of $r = 15$ μm plotted as functions of the normalized applied load P/P_0 for a CT specimen without hydride and CT specimens with split circumferential hydrides with the height of 150 μm and different ligament thicknesses.

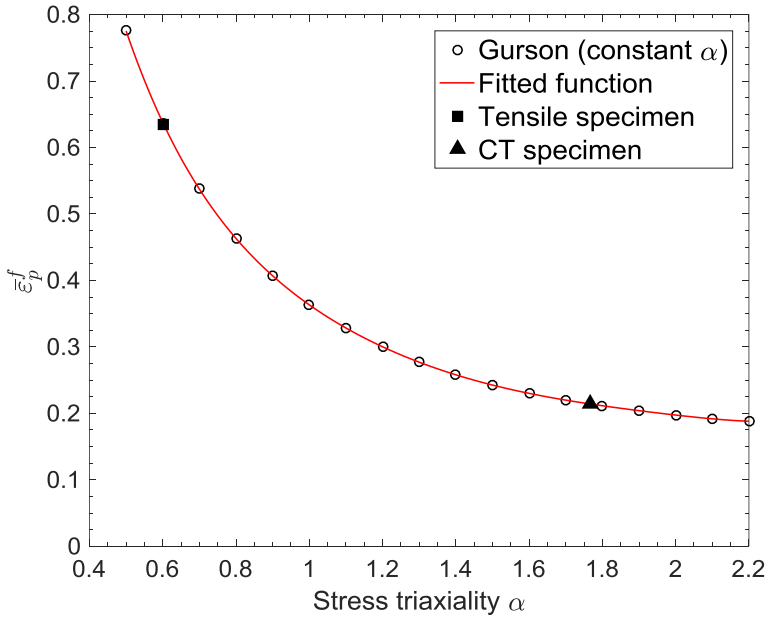

Figure 2-24. The failure effective plastic strain $\bar{\varepsilon}_p^f$ plotted as a function of the stress triaxiality α for a material element subjected to constant stress triaxiality α during the deformation histories.

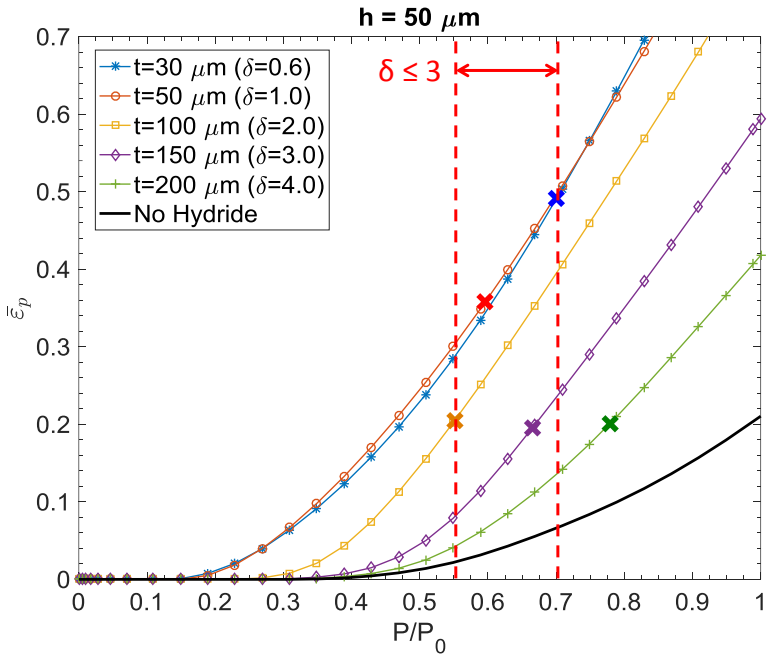

Figure 2-25. The values of the effective plastic strains $\bar{\varepsilon}_p$ at the radial distance of $r = 15$ μm as functions of the normalized applied load for a CT specimen without hydride and with split circumferential hydrides with the height of 50 μm and different ligament thicknesses.

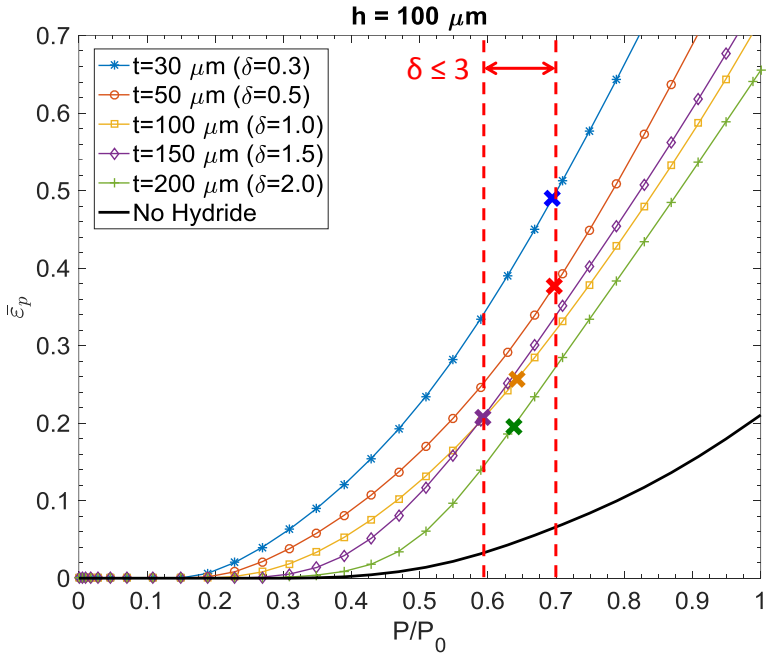

Figure 2-26. The values of the effective plastic strains $\bar{\varepsilon}_p$ at the radial distance of $r = 15$ μm as functions of the normalized applied load for a CT specimen without hydride and with split circumferential hydrides with the height of 100 μm and different ligament thicknesses.

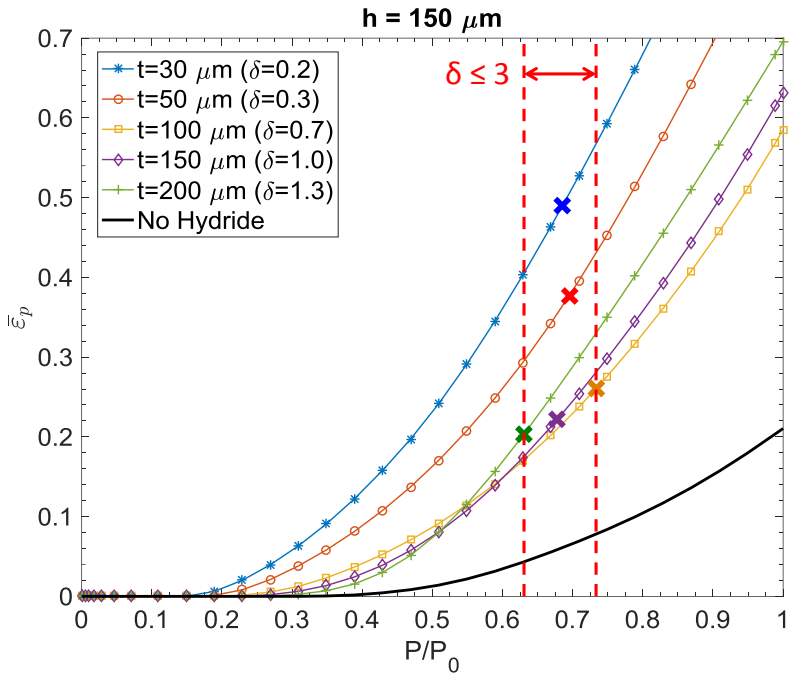

Figure 2-27. The values of the effective plastic strains $\bar{\varepsilon}_p$ at the radial distance of $r = 15$ μm as functions of the normalized applied load for a CT specimen without hydride and with split circumferential hydrides with the height of 150 μm and different ligament thicknesses.

Chapter 3 Ductile Fracture Initiation near Axial Crack Fronts in Pressure Tubes of Hydrided Irradiated Zr-2.5Nb Materials with Split Circumferential Hydrides

3.1 Introduction

In a companion investigation in Chapter 2, the reduced fracture toughness associated with split circumferential hydrides at room temperature was examined by conducting three-dimensional finite element analyses of compact tension (CT) specimens of irradiated Zr-2.5Nb materials without and with split circumferential hydrides. The free surfaces of the split circumferential hydrides allow the strain concentration developed in the ligament between the split circumferential hydrides. However, the free surfaces also reduce the stress triaxiality in the ligament ahead of the crack front when compared with that in CT specimens without split circumferential hydrides. The stress concentration in the ligament promotes ductile failure while the low stress triaxiality increases the failure effective plastic strain. In order to consider these two factors due to free surfaces simultaneously, the Gurson yield model [17] was used to develop a failure effective plastic strain criterion as a function of the stress triaxiality, motivated by the work of Bao and Wierzbicki [5], due to lack of such experimental data for irradiated Zr-2.5Nb materials.

Currently, no experimental data are available to indicate the magnitude of the failure effective plastic strain for irradiated Zr-2.5Nb materials under such a very high stress triaxiality of about 1.766 ahead of the crack front. However, with the selections of consistent

Published in Engineering Fracture Mechanics, 186, pp. 1–20, 2017

computational parameters such as the element size and the critical radial distance ahead of the crack front in all finite element analyses, the failure strain criterion with consideration of stress triaxiality used in Chapter 2 should provide reasonable qualitative and quantitative results on the effects of the strain concentration and stress triaxiality in the ligaments on the fracture initiation loads for CT specimens with split circumferential hydrides. The research results in Chapter 2 indicated that with a strain-based fracture criterion with consideration of stress triaxiality at a critical distance ahead of the main crack front in a full-sized CT specimen, only 60% to 70% of the fracture initiation load of an unhydrided irradiated CT specimen is needed to fracture a hydrided irradiated CT specimen with many randomly distributed split circumferential hydrides along the crack front.

Within the context of fracture mechanics, the stress triaxiality ahead of a crack tip can be affected by the specimen geometries and applied loads. Since the geometry and pressure loading for an axial crack in a pressure tube (PT) specimen of Scarth et al. [27] are different from those for a crack in a CT specimen, the crack-tip fields along the crack fronts can be different. Therefore, detailed analyses of the crack-tip fields along the axial crack front in PT specimens are needed to address the effects of loading and geometry. With the use of the strain-based failure criterion with consideration of stress triaxiality obtained in Chapter 2, this investigation can effectively account for the fracture initiation for the different crack-tip fields along the crack fronts due to the different geometries and different types of loading conditions for an axial crack in a PT specimen under an applied internal pressure and a crack in a CT specimen under an applied load.

In this investigation, the reduced fracture toughness associated with split circumferential hydrides at room temperature is examined by conducting three-dimensional finite element

analyses of PT specimens of irradiated Zr-2.5Nb materials without and with split circumferential hydrides. The stress-strain relation used in this investigation is the same as that used for the earlier investigation of CT specimens in Chapter 2. A three-dimensional finite element analysis of a PT specimen of irradiated Zr-2.5Nb materials without circumferential hydrides is first conducted with the submodeling strategy established in Sung et al. [39]. The computational results are used to examine the J-integral distributions along the crack front and the stress and strain states ahead of the axial crack front in the PT specimen. The effects of the pressure loading and the tube curvature on the plastic zone shapes and sizes along the crack front from the inner tube surface to the outer tube surface will also be examined under the given pressure corresponding to the fracture toughness K_C obtained from the corresponding curved CT specimens. Without using the criterion of the maximum J-integral along the crack front or the maximum opening stress at a critical distance ahead of the crack front, the critical location along the crack front is determined based on the strain-based failure criterion with consideration of stress triaxiality as established in Chapter 2. The computational results of the PT specimen are then benchmarked with those of the CT specimen to determine the effects of different types of loading and geometries on the fracture initiation loads for the PT and CT specimens.

Next, three-dimensional finite element analyses of PT specimens of irradiated Zr-2.5Nb materials with three pairs of split circumferential hydrides with various hydride heights and ligament thicknesses near three possible critical locations along the crack front for fracture initiation in the PT specimen are then conducted to examine the effective plastic strains and the stress triaxiality in the ligaments between the split circumferential hydrides. Following the same strategy established in Chapter 2, the effects of the plastic strain concentration and stress triaxiality in the ligaments on the fracture initiation in the PT specimens of irradiated Zr-2.5Nb

materials with hydrides are examined and investigated. Based on the strain-based failure criterion with consideration of stress triaxiality, the fracture initiation loads are determined for PT specimens with split circumferential hydrides with various heights and ligament thicknesses under the given internal pressure corresponding to the fracture toughness K_C obtained from the experimental results of curved compact tension specimens without hydride [37]. Finally, conclusions are made.

3.2 Finite Element Models

The geometry of the three-dimensional finite element models in this investigation is based on the geometry of the pressure tube (PT) specimens [27] obtained from removed irradiated pressure tubes. Figure 3-1 shows a schematic of a PT specimen with an axial crack. The PT specimen has the length $2L$ of 500 mm, inner radius R_i of 52 mm, outer radius R_o of 56 mm, and thickness T of 4 mm. The axial through-thickness crack with the length $2a$ of 55 mm is located in the middle of the specimen and parallel to the axial direction. Due to the symmetries of the PT specimen, only a quarter of a PT specimen is considered for modeling. In order to investigate the effects of split circumferential hydrides on the fracture behavior ahead of the front of the axial crack in a hydrided irradiated PT specimen, submodeling used in the earlier investigation of CT specimens [39] was also used in this investigation.

Figure 3-2 shows the geometry of the global finite element model of a right upper quarter of a PT specimen for three-dimensional finite element analyses. The global X, Y and Z coordinates are also plotted in the figure. The global X coordinate is plotted along the axial direction for convenience of presentation in this figure and many figures presented later. The global model was partitioned to four regions of different element sizes for efficient meshing and

computation. The four regions of different element sizes are shown in Figures 3-3(a) and (b). The sizes and the numbers of elements for the four regions are listed in Table 3-1. The X symmetry boundary condition was imposed on the left surface and the Y symmetry boundary condition was imposed on the bottom surface of the quarter model, as shown in Figures 3-4(a) and (b). Without using transitional elements, tie constraints were used to impose the displacement continuity between the regions of different element sizes, as shown in Figure 3-4(b). Collapsed elements with the size of 25 μm by 25 μm by 50 μm in the X, Y and Z directions were placed adjacent to the crack front to induce the necessary singularity [39]. The collapsed elements are linear wedge elements degenerated from linear brick elements. The overlapping crack-front nodes are untied and can move independently. The total number of the elements for the global model is 314,680. For better demonstration of computational results, two polar coordinate systems are introduced in Figures 3-5(a) and (b). The $R-\Theta$ coordinate system is defined on the axial cross-sectional planes of the pressure tube as shown in Figure 3-5(a) while the $r-\theta$ coordinate system is defined on the axial-circumferential planes near the crack front as shown in Figure 3-5(b).

In order to study the effects of split circumferential hydrides with various hydride heights and ligament thicknesses on the fracture initiation in the PT specimens, several submodels were built with the same geometry in this investigation, as shown in Figure 3-6. The size is defined as that of Region 4 of the global model, as shown in Figure 3-3(b), based on the size of the plastic zone from the elastic-plastic analysis of the global model [39]. In order to obtain accurate results using submodeling, the submodels should enclose the entire plastic zone through the thickness [39]. The submodels were also partitioned to three regions of different element sizes. The partition of the regions of different element sizes on the $X-Y$ plane is shown in Figures 3-7(a)

and (b). The sizes and the numbers of elements for the three regions are listed in Table 3-2. Region 3 of the submodels has two sizes of elements for better computational efficiency when split circumferential hydrides are considered. The submodel boundaries, where the displacements are acquired from the analyses of the corresponding global model, and the Y symmetry boundary condition are also shown in Figures 3-8(a) and (b). The right back surface, marked with "internal pressure", is the inner surface with the applied internal pressure and the left side surface is the outer free surface of the submodels. Tie constraints were used to impose the displacement continuity between different regions, as shown in Figure 3-8(b). Due to the small size (5 μm by 5 μm by 5 μm) of the elements near the crack front, no collapsed element was needed in the submodels [39]. The total number of elements for each submodel is 987,840.

Split circumferential hydrides are modeled by separating elements where the hydrides are located. Three pairs of split circumferential hydrides are assumed to exist (a) where the largest crack opening stress occurs near $R = 53$ mm, (b) where the earliest fracture initiation occurs near $R = 54$ mm with the failure criterion as the pressure increases and (c) where the largest J-integral occurs near $R = 55$ mm in the PT specimen ahead of the crack front, as shown in Figure 3-9. These three cases will be discussed later. Since only a quarter of a PT specimen is considered in this study, only the upper half parts of split circumferential hydrides are modeled. The locations of the split circumferential hydrides with three different sizes of 425 μm by 50 μm, 425 μm by 100 μm and 425 μm by 150 μm on the $X - Y$ plane are shown in Figures 3-10(a) to (c), respectively. The hydride dimensions were selected based on the experimental observations of the split circumferential hydrides with the dimension in the axial direction larger than the dimensions in the other two directions [27,33]. Different ligament thicknesses between split circumferential hydrides considered in this investigation are 30, 50, 100, 150, and 200 μm.

These different ligament thicknesses are simulated by controlling the distance between the split circumferential hydrides of each pair.

The irradiated Zr-2.5Nb material behavior used in the finite element analyses is the same as that in the investigation of the fracture initiation in CT specimens in Chapter 2. The Young's modulus is taken to be 102.1 GPa and the Poisson's ratio is taken to be 0.4. The plastic hardening curve is based on fitting the experimental results of transverse tensile tests by a three-dimensional finite element analysis as shown in Figure A-3. The plastic anisotropy of the Zr-2.5Nb material is not considered in this investigation and will be considered in the future. An internal pressure p_0 of 6.815 MPa is applied on the inner surface, which corresponds to the same K_C = 59.2 $\text{MPa}\cdot\sqrt{\text{m}}$ [37] as that used for CT specimens in Chapter 2. The detailed derivation is shown in Appendix E. It should be noted that the pressure is not applied on the crack faces since an internal patch was used to seal the pressure tube in an actual burst test. With the assumption of a closed pressure tube, a uniform tensile stress of 42.66 MPa is applied on the end surface to account for the axial stress due to the internal pressure. The commercial finite element program ABAQUS was employed to perform the computations. First-order three-dimensional elements with reduced integration (C3D8R) were used exclusively in this study since large local plastic strains are expected. The option of the geometric nonlinearity is set to off in the elastic analyses and is turned on in the elastic-plastic analyses.

3.3 Computational Results

3.3.1. Pressure Tube Specimen without Split Circumferential Hydrides

Based on the submodeling strategy established in [39], two conditions should be satisfied for appropriate sets of global models and submodels. First, the mechanical behaviors near the

crack front of the submodels should be similar to that of the global model. Secondly, the size of submodels should enclose the entire plastic zones in all elastic-plastic analyses. Figure 3-11 shows the consistency of the distributions of the computational J-integrals in the thickness direction from the elastic analyses of the global model and the submodel without split circumferential hydrides under the internal pressure p_0 of 6.815 MPa corresponding to K_C = 59.2 $\text{MPa}\cdot\sqrt{\text{m}}$. It should be mentioned that the computational results from ABAQUS for the 11 annular volumes enclosing the crack front of interest (excluding the immediate one close to the crack front) for the J-integral have only the difference about 1%. The horizontal axis R represents the location in the thickness direction of the PT specimen. Due to the consistency of the two distributions of the J-integrals, the first condition is fulfilled. As shown in Figure 3-11, the maximum value of the J-integral occurs close to the outer tube surface near $R = 55$ mm, not in the middle of the tube thickness. Fracture initiation can possibly occur at this location.

Figure 3-12 shows the envelope of the three-dimensional plastic zone in the submodel from the elastic-plastic analysis. The plastic zone is slightly larger than the fine mesh region of the submodel but is still enclosed in the submodel. Slight discontinuities of the envelope surface of the plastic zone occur where the envelope surface crosses the interfaces between two regions with different mesh sizes. Based on the discussions above, this set of the global model and submodel satisfies the two conditions and is adequate for the three-dimensional finite element analyses of the quarter PT specimen. As shown in Figure 3-12, the largest plastic zone size is not located on the inner or outer tube surfaces. Instead, the largest plastic zone size is located near the outer surface.

The contours of the opening stress $\sigma_{\Theta\Theta}$ and the out-of-plane normal stress σ_{RR} on the crack plane ahead of the crack front are plotted in Figures 3-13 and 3-14, respectively. The

radial distance r is the distance from the crack front in the X (axial) direction on the crack plane. The range of interest of r in this study is from $r = 0$ μm to $r = 125$ μm, as shown in Figures 3-13 and 3-14. In order to clearly show the magnitudes of the stresses ahead of the crack front, the distributions of the opening stress $\sigma_{\Theta\Theta}$ and the out-of-plane normal stress σ_{RR} are also plotted at different radial distance r's ahead of the crack front in the thickness direction in Figures 3-15 and 3-16, respectively. As shown in Figures 3-15 and 3-16, the distributions of the opening stress $\sigma_{\Theta\Theta}$ and the out-of-plane normal stress σ_{RR} are quite consistent with those in Figures 2-14 and 2-15 in Chapter 2. The largest opening stress $\sigma_{\Theta\Theta}$ and the largest out-of-plane normal stress σ_{RR} occur at the radial distances of about $r = 55$ μm and $r = 50$ μm, respectively, in the middle but leaning to the inner surface of the PT specimen, not adjacent to the crack front. The largest opening stress $\sigma_{\Theta\Theta}$ is quite close to the theoretical value of 3,356 MPa derived from the slip line theory for rigid perfectly plastic materials under plane strain conditions. This means that the stress state near the middle portion of the crack front but close to the inner surface is close to that of the plane strain conditions under the given internal pressure. With the hydride fracture stress of 750 MPa [28], the distributions of the opening stress $\sigma_{\Theta\Theta}$ and the out-of-plane normal stress σ_{RR} indicate that all radial hydrides ahead of the crack front will fracture, and circumferential hydrides ahead of the crack front split in the middle portion of specimen but they do not split near the inner and outer surfaces. The size of the zone without split circumferential hydrides increases with the increasing radial distance r from the crack front.

Due to the complicated distributions of the stresses ahead of the crack front and the J-integral along the crack front in the PT specimen, the location of the earliest fracture initiation is not necessary in the middle of the specimen. In order to determine the location of the earliest fracture initiation, the same strain-based failure criterion with consideration of stress triaxiality

used in Chapter 2 is adopted in this investigation. The failure effective plastic strain $\bar{\varepsilon}_p^f$ as a function of the stress triaxiality α is plotted in Figure 2-24. The failure criterion is obtained from the Gurson yield model with the experimental/computational results of transverse tensile tests, and the effective plastic strain of the critical material element ahead of the crack front in a CT specimen without hydride at fracture initiation. The failure effective plastic strain $\bar{\varepsilon}_p^f$ of 0.634 for the critical material element under the average stress triaxiality of 0.603 in the transverse tensile specimen and the failure effective plastic strain $\bar{\varepsilon}_p^f$ of 0.21 for the critical material element under the average stress triaxiality of 1.766 ahead of the crack front in the CT specimen without hydride are shown as symbols in Figure 2-24. The strain-based failure criterion is fitted by a sixth-order polynomial function of the stress triaxiality α in Appendix C. The details for the development of the strain-based failure criterion with consideration of stress triaxiality based on the Gurson yield model and the work of Bao and Wierzbicki [5] are presented in Chapter 2.

The stress triaxiality α is defined as

$$\alpha = \frac{\sigma_m}{\sigma_e} \tag{3-1}$$

where σ_m $(=\sigma_{kk}/3)$ represents the hydrostatic tension, and σ_e $(=\sqrt{3\sigma'_{ij}\sigma'_{ij}/2}\,)$ is the tensile effective stress which is based on the second invariant of the deviatoric stress tensor σ'_{ij} ($=\sigma_{ij}-\sigma_{kk}\delta_{ij}/3$). When the stress triaxiality α is large, the ductile fracture process is governed by void nucleation, growth and coalescence, and the failure effective plastic strain $\bar{\varepsilon}_p^f$ decreases with increasing stress triaxiality α [5]. In order to account for the effect of changing stress

triaxiality α during the deformation history for a material element of interest, an average stress triaxiality $\bar{\alpha}$ proposed by Bao and Wierzbicki [5] is adopted here as

$$\bar{\alpha} = \frac{1}{\bar{\varepsilon}_p^f} \int_0^{\bar{\varepsilon}_p^f} \alpha \, d\bar{\varepsilon}_p \tag{3-2}$$

Here, $\bar{\varepsilon}_p^f$ represents the failure effective plastic strain.

Figure 3-17(a) shows the effective plastic strain $\bar{\varepsilon}_p$ and the failure effective plastic strain $\bar{\varepsilon}_p^f$ (for the average stress triaxiality $\bar{\alpha}$) plotted as functions of the radial coordinate ranging from $R = 52$ mm to $R = 56$ mm at the radial distance of $r = 15$ μm ahead of the crack front of the PT specimen without split circumferential hydrides under the given internal pressure p_0 of 6.815 MPa corresponding to K_C = 59.2 MPa$\cdot\sqrt{\text{m}}$. The location of the earliest fracture initiation is where the effective plastic strain $\bar{\varepsilon}_p$ is closest to the failure effective plastic strain $\bar{\varepsilon}_p^f$, which is at $R = 53.7$ mm. Figure 3-17(b) shows the difference between the effective plastic strain $\bar{\varepsilon}_p$ and the failure effective plastic strain $\bar{\varepsilon}_p^f$ from $R = 53$ mm to $R = 55$ mm where the difference is relatively small. As shown in the figure, the minimum difference of 1.36% occurs at the radial distance of $r = 15$ μm and $R = 53.7$ mm.

Figure 3-18 shows the histories of the effective plastic strain $\bar{\varepsilon}_p$ and the failure effective plastic strain $\bar{\varepsilon}_p^f$ at the radial distance of $r = 15$ μm and $R = 53.7$ mm near the end of the application of the normalized internal pressure p / p_0 for a PT specimen without hydride. In the figure, the dashed red and blue lines represent the anticipated histories of $\bar{\varepsilon}_p^f$ and $\bar{\varepsilon}_p$, respectively, when the normalized internal pressure p / p_0 is larger than 1.0. As shown in Figure 3-18, additional 3% of the given internal pressure is needed for the effective plastic strain $\bar{\varepsilon}_p$ to

reach the failure effective plastic strain $\bar{\varepsilon}_p^f$. The results indicate that with the same strain-based failure criterion with consideration of stress triaxiality, the CT specimen fails and the PT specimen almost fails under the same $K_C = 59.2\ \text{MPa}\cdot\sqrt{\text{m}}$. It should be mentioned that the present strain-based failure criterion with consideration of stress triaxiality is used to account for the constraint effects ahead the crack front for different CT and PT specimen geometries and their different types of loading.

Figure 3-19 shows the effective plastic strain $\bar{\varepsilon}_p$ and the failure effective plastic strain $\bar{\varepsilon}_p^f$ at the radial distance of $r = 15$ μm and $R = 54$ mm, which is in the middle of the thickness of the PT specimen. As shown in the figure, the trends of the effective plastic strain $\bar{\varepsilon}_p$ and the failure effective plastic strain $\bar{\varepsilon}_p^f$ are very similar to those at $R = 53.7$ mm. Also, additional 3% of the given internal pressure is needed for the effective plastic strain $\bar{\varepsilon}_p$ to reach the failure effective plastic strain $\bar{\varepsilon}_p^f$. In the later investigation of the PT specimen with split circumferential hydrides, the location at $R = 54$ mm is chosen to represent the location of the earliest fracture initiation in the thickness direction.

3.3.2. Pressure Tube Specimen with Split Circumferential Hydrides

Three pairs of split circumferential hydrides with various heights and ligament thicknesses ahead of the crack fronts are considered at $R = 53$ mm, 54 mm and 55 mm, as schematically shown in Figure 3-9. As discussed earlier, $R = 53$ mm represents the location of the maximum opening stress ahead of the crack front, $R = 54$ mm represents the location where the earliest fracture initiation occurs with the strain-based failure criterion with consideration of stress triaxiality, and $R = 55$ mm represents the location of the largest J-integral along the crack

front. In this paper, the computational results for $R = 54$ mm will be first presented and the computational results for $R = 53$ mm and $R = 55$ mm will be briefly discussed later.

For the pair of split circumferential hydrides with various heights and ligament thicknesses ahead of the crack front near the location of $R = 54$ mm, the deformed meshes with the magnitudes of the effective plastic strain $\bar{\varepsilon}_p$ for the finite elements marked in colors for the radial-circumferential ($Z - Y$ or $R - \Theta$) plane near $R = 54$ mm at the radial distance $r = 15$ μm ahead of the crack front under 60 percent of the applied internal pressure p_0 of 6.815 MPa are shown in Figures 3-20 to 3-22. Note that the radial distance of interest of $r = 15$ μm is three elements away from the crack front, which is consistent with that in the earlier investigation of CT specimens in Chapter 2. For convenient discussions of the computational results, the ligament thickness ratio δ is defined as

$$\delta = \frac{t}{h} \tag{3-3}$$

where t represents the ligament thickness and h represents the hydride height. Figures 3-20(a) to (e) show the deformed meshes with the magnitudes of the effective plastic strain $\bar{\varepsilon}_p$ for the PT specimens with split circumferential hydrides with the height of 50 μm and the ligament thicknesses of 30, 50, 100, 150, and 200 μm, respectively. In the figures, only the finite elements with the magnitudes of the effective plastic strain $\bar{\varepsilon}_p$ larger than 6.5% are marked in color. In Figure 3-20, the red color represents the regions where the effective plastic strain is larger than 20% while the white color represents the regions where the effective plastic strain is less than 6.5%. With the same designations of colors for the effective plastic strains for the finite elements, Figures 3-21 and 3-22 show the deformed meshes of the PT specimens with hydrides with the heights of 100 μm and 150 μm, respectively. In Figures 3-20 to 3-22, the inner tube

surface is on the left side of the figures and the outer tube surface is on the right side of the figures.

In the earlier investigation of CT specimens in Chapter 2, three types of strain concentration were identified and discussed. In this investigation, the same three types of strain concentration can also be identified in Figures 3-20 to 3-22. The type of strain concentration can be determined by the ligament thickness ratio δ. For small ligament thickness ratios with $\delta \leq 1$, strain concentration occurs in the middle of the ligament and then shear localization emanates from it, as shown in Figures 3-20(a) to (b), Figures 3-21(a) to (c) and Figures 3-22(a) to (d). For the cases of the ligament thickness t comparable to the hydride height h with $1 < \delta \leq 2$, shear localization also emanates from the tip of the split circumferential hydride at the angle slightly smaller than 45 degrees with respect to the radial-axial plane in addition to the strain concentration in the middle of the ligament. Two types of shear localization emanate from different sources and then connect with each other to cross the entire ligament, as shown in Figure 3-20(c), Figures 3-21(d) to (e) and Figure 3-22(e). For large ligament thickness ratios with $\delta > 2$, shear localization emanates from the tip of the split circumferential hydride at the angle slightly smaller than 45 degrees with respect to the radial-axial plane but ends near the split circumferential hydride, as shown in Figures 3-20(d) to (e). Since the general trends of different types of strain localization for different thickness ratios are exactly the same as those in Chapter 2, the same conclusion can be drawn that the strain concentration with $\delta \leq 2$ can be assumed to be pronounced in a hydrided irradiated Zr-2.5Nb pressure tube based on the experimental observations of ligament thicknesses and heights of split hydrides as reported in [21]. It should be noted that for the ligament thickness ratio with $\delta = 3$ in Figures 3-20(d), the strain

concentration in the middle of the ligament is also moderate. As shown in Figures 3-20 to 3-22, the strain distributions show slight asymmetry for the PT specimens.

In order to consider the effect of strain concentration on the ductile fracture of ligaments, the same strain-based failure criterion with consideration of stress triaxiality used in Chapter 2 is considered. For a material element of interest ahead of the crack front, an average stress triaxiality $\overline{\alpha}$ can be determined during the deformation history. The failure effective plastic strain $\overline{\varepsilon}_p^f$ for the material element of interest can then be determined based on the same relationship between the failure effective plastic strain $\overline{\varepsilon}_p^f$ and the average stress triaxiality $\overline{\alpha}$ as shown in Figure 2-24. The histories of the effective plastic strains $\overline{\varepsilon}_p$ at the radial distance of $r = 15$ μm ahead of the crack front at $R = 54$ mm of a PT specimen without hydride and PT specimens with hydrides with the heights of 50, 100 and 150 μm and different ligament thicknesses are plotted as functions of the normalized internal pressure p / p_0 with p_0 = 6.815 MPa in Figures 3-23 to 3-25, respectively. The values of the failure effective plastic strain $\overline{\varepsilon}_p^f$ are marked by the crosses with the corresponding colors in the figures. In these figures, the material elements in the middle of ligaments at the radial distance of $r = 15$ μm ahead of the crack front at $R = 54$ mm in PT specimens with hydrides with various heights and ligament thicknesses will achieve the failure effective plastic strain $\overline{\varepsilon}_p^f$ earlier than the one without hydride due to different types of strain concentration as discussed earlier.

Based on the values of the failure effective plastic strain $\overline{\varepsilon}_p^f$ for the cases with $\delta \le 3$ as marked in Figures 3-23 to 3-25, the necessary fraction of the internal pressure for fracture initiation to reach the values of the failure effective plastic strain $\overline{\varepsilon}_p^f$ decreases to 0.60 to 0.70. For the cases with $\delta > 3$, the necessary fraction of the internal pressure for fracture initiation to

reach the failure effective plastic strain $\bar{\varepsilon}_p^f$ is between 0.70 to 1.00, depending on the value of the ligament thickness ratio δ. It should be mentioned again that the values of the ligament thickness ratio δ are commonly no larger than 3 in a hydrided irradiated Zr-2.5Nb pressure tube as explained in Chapter 2. As shown in Figures 3-23 to 3-25, the computational results can be used to explain the near 35% reduction of the K_C at room temperature obtained from hydrided irradiated pressure tube specimens when compared with that from unhydrided irradiated ones as observed in [37].

Finally, the computational results for $R = 53$ mm and $R = 55$ mm are very similar to those for $R = 54$ mm presented in Figures 3-20 to 3-25. In general, for a given normalized internal pressure p / p_0, the values of the effective plastic strain $\bar{\varepsilon}_p$ at the location of $r = 15$ μm ahead of the crack front at $R = 53$ mm and $R = 55$ mm are just slightly lower than those at $R = 54$ mm for the hydride heights of 50 μm, 100 μm and 150 μm and various ligament thicknesses. This general trend indicates that the necessary fraction of the internal pressure for fracture initiation due to the pairs of the split circumferential hydrides at $R = 53$ mm and $R = 55$ mm is just slightly higher than 0.60 to 0.70 as discussed earlier for $R = 54$ mm. The computational results are consistent with the results shown in Figure 3-17 where the effective plastic strain $\bar{\varepsilon}_p$ and the failure effective plastic strain $\bar{\varepsilon}_p^f$ at $R = 53$ mm and $R = 55$ mm are very close to each other as those for $R = 54$ mm.

3.4 Conclusions

In this investigation, simulations of pressure tube (PT) specimens without and with split circumferential hydrides were conducted with a quarter finite element model using the

submodeling technique. For a PT specimen without split circumferential hydrides, the computational results first show that the maximum J-integral occurs not in the middle of the crack front but at about one quarter of the tube thickness from the outer tube surface. The distributions of the opening stress $\sigma_{\Theta\Theta}$ and the out-of-plane normal stress σ_{RR} on the crack plane ahead of the crack front are then obtained. The distributions show that the largest opening stress $\sigma_{\Theta\Theta}$ and the largest out-of-plane normal stress σ_{RR} occur at the radial distances of about $r = 55$ μm and $r = 50$ μm, respectively, not adjacent to the crack front, under the given internal pressure at about one quarter of the tube thickness from the inner tube surface. The largest opening stress $\sigma_{\Theta\Theta}$ is quite close to the theoretical value derived from the slip line theory for rigid perfectly plastic materials under plane strain conditions. This means that the stress state near about one quarter thickness from the inner surface along the crack front is close to that of plane strain conditions under the given internal pressure. With the hydride fracture stress of 750 MPa, the distributions of the opening stress $\sigma_{\Theta\Theta}$ and the out-of-plane normal stress σ_{RR} show that all radial hydrides ahead of the crack front will fracture, and circumferential hydrides ahead of the crack front split in the middle portion of specimen but they do not split near the inner and outer surfaces. The sizes of the zones without split circumferential hydrides increase with the increasing radial distance r from the crack front.

With the same strain-based failure criterion with consideration of stress triaxiality in Chapter 2, the location of the earliest fracture initiation in the thickness direction can be determined to be at $R = 53.7$ mm near the middle of the crack front. Under the same K_C, the CT specimen fails and the PT specimen almost fails, respectively, based on the same strain-based failure criterion with consideration of stress triaxiality. It should be mentioned that the present strain-based failure criterion with consideration of stress triaxiality can be used to account for the

three-dimensional effects on the fracture initiation along the crack fronts in different specimen geometries and different types of loading.

For PT specimens with split circumferential hydrides with various heights and ligament thicknesses near the middle of the crack front, strain concentration is observed in the middle of the ligament when the ratio of the ligament thickness to the hydride height is less than 3. With a strain-based failure criterion with consideration of stress triaxiality, the necessary fraction of the internal pressure for fracture initiation is about 0.60 to 0.70 to fracture the ligaments with low plastic work or energy types of strain concentration. The results suggest that low plastic work or energy types of strain concentration in ligaments are pronounced in a hydrided irradiated Zr-2.5Nb pressure tube. The computational results suggest that only 60% to 70% of the internal pressure for fracture initiation of an unhydrided irradiated PT specimen is needed to fracture a hydrided irradiated PT specimen with many randomly distributed split circumferential hydrides near the crack front. The computational results can be used to explain the near 35% reduction of the K_C at room temperature obtained from hydrided irradiated pressure tube specimens when compared with that from unhydrided irradiated ones.

Acknowledgement

The support of this work from CANDU Owners Group is greatly appreciated. Helpful discussions with Brian Leitch and Sterling St. Lawrence of Canadian Nuclear Laboratories are greatly appreciated.

Table 3-1. Sizes and numbers of elements for the four regions of the three-dimensional global finite element model

Region of global model	Element size in X (axial), Θ (circumferential) and R (radial) directions (μm)	Number of elements
Region 1	1000x1000x1000	169,880
Region 2	500x500x500	5,920
Region 3	100x100x100	48,800
Region 4	50x50x50	90,080

Table 3-2. Sizes and numbers of elements for the three regions of the three-dimensional submodels

Region of submodel	Element size in X (axial), Θ (circumferential) and R (radial) directions (μm)	Number of elements
Region 1	50x50x50	71,360
Region 2	25x25x25	132,480
Region 3	5x5x5, 25x5x5	784,000

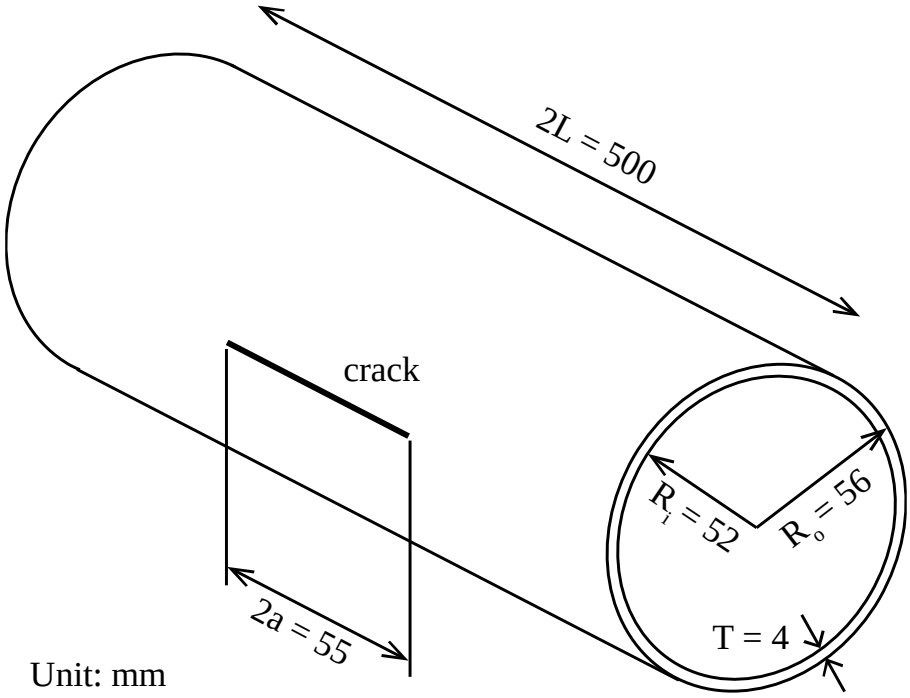

Figure 3-1. A schematic of a pressure tube (PT) specimen with an axial crack

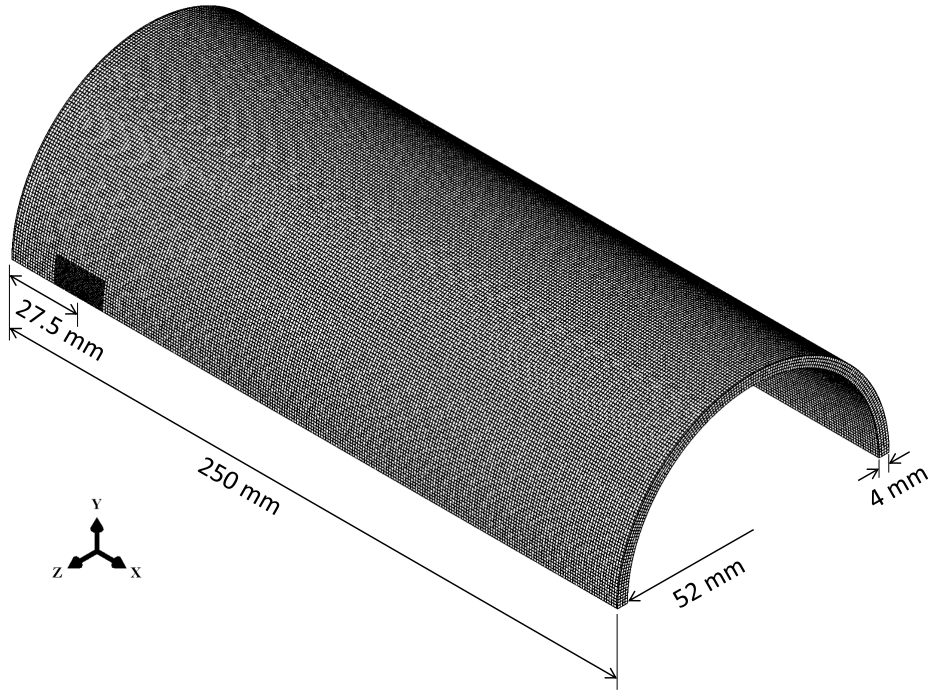

Figure 3-2. The geometry of the three-dimensional global finite element model of a quarter of a PT specimen

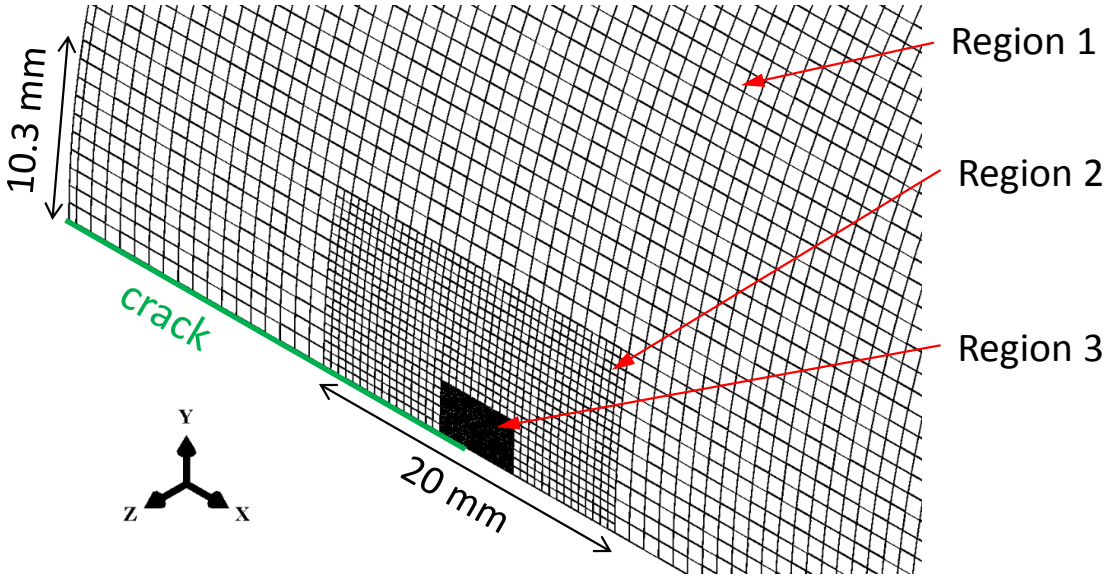

(a)

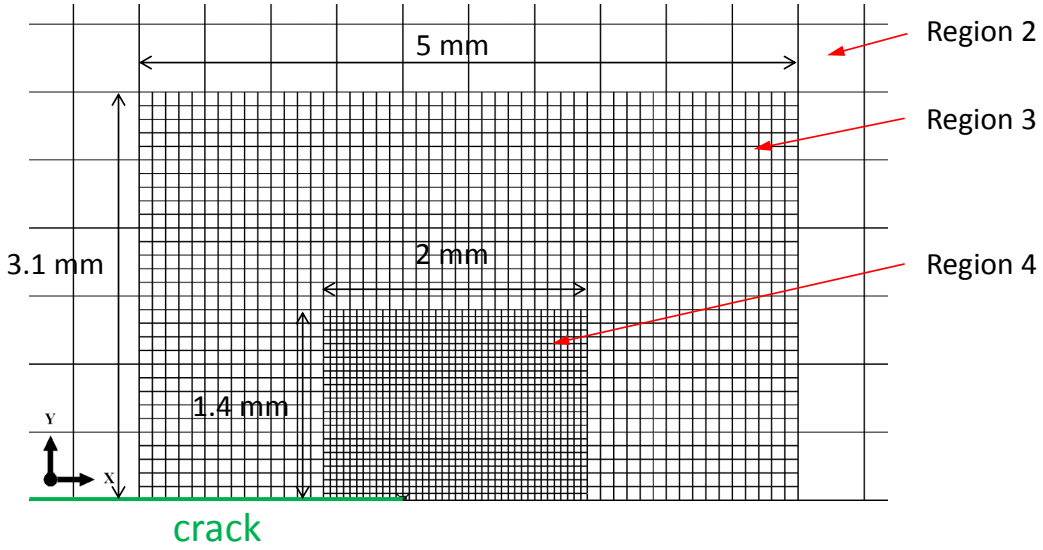

(b)

Figure 3-3. Partition of regions of different element sizes (a) in a three-dimensional view and (b) on the $X-Y$ plane of the global model.

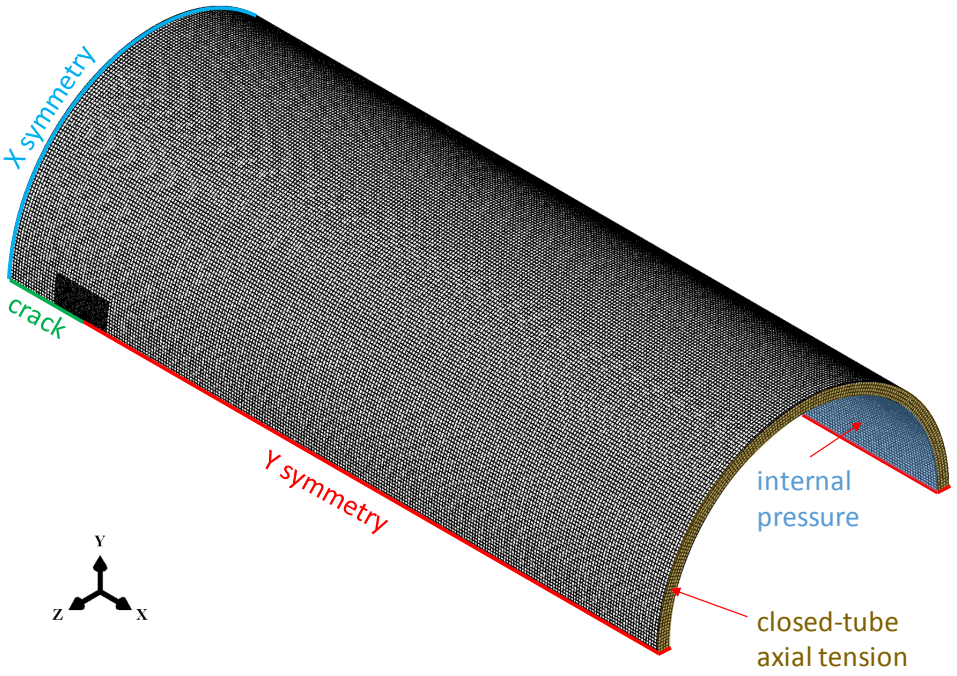

(a)

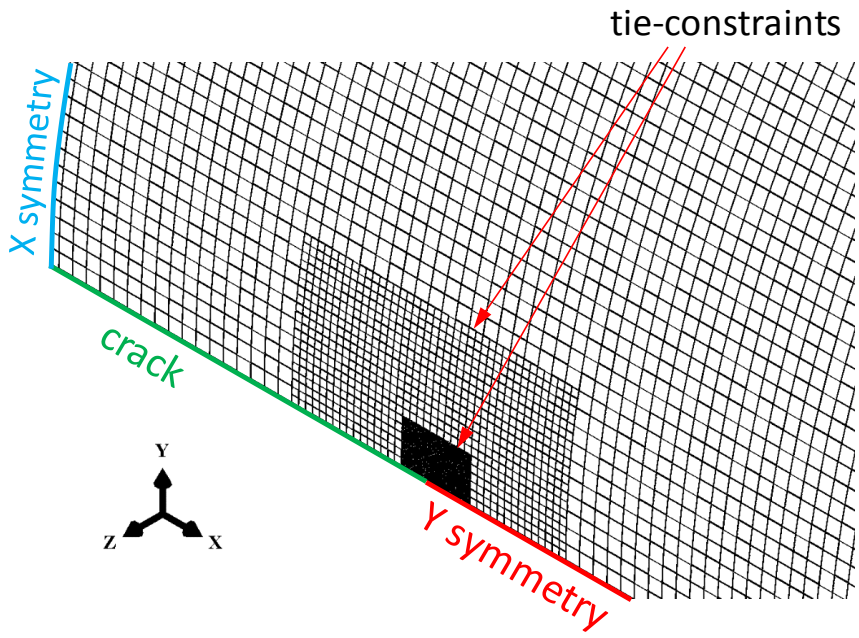

(b)

Figure 3-4. Boundary and constraint conditions of the three-dimensional global finite element model.

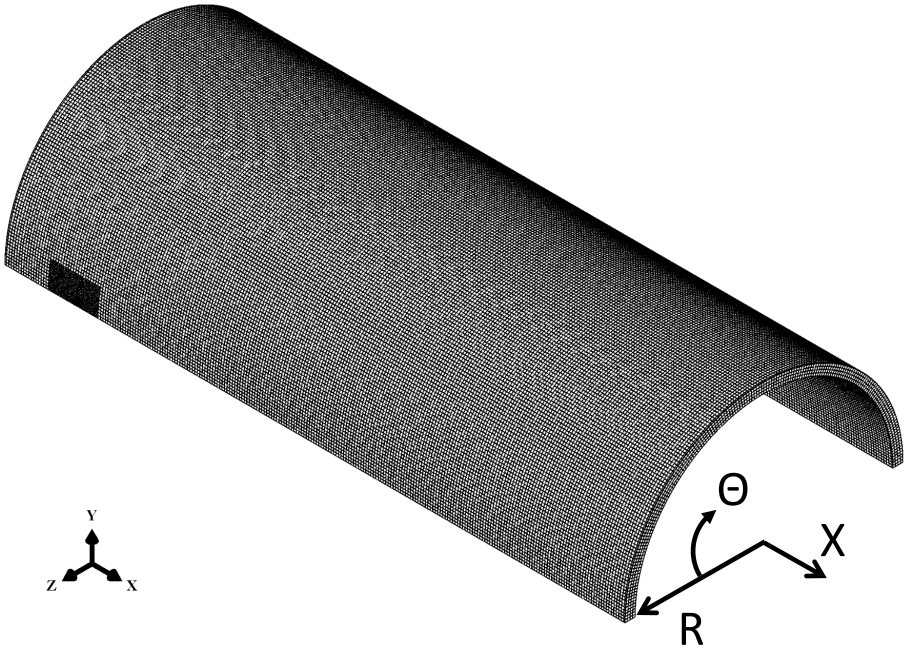

(a)

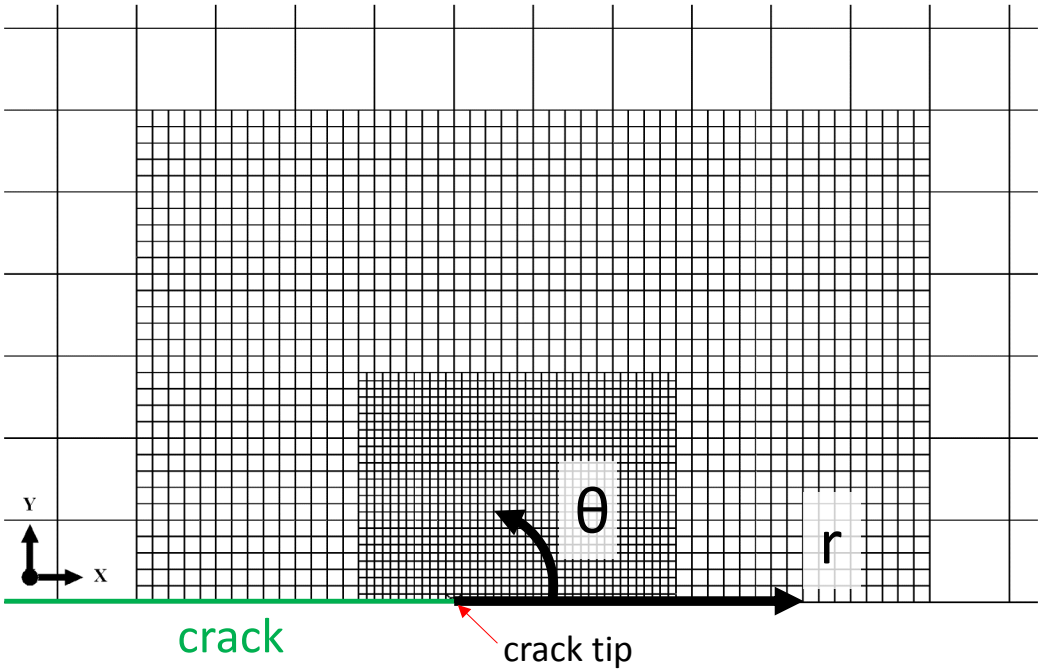

(b)

Figure 3-5. (a) The $R-\Theta$ coordinate system on the axial cross-sectional planes of the pressure tube and (b) the $r-\theta$ coordinate system on the axial-circumferential planes near the crack front.

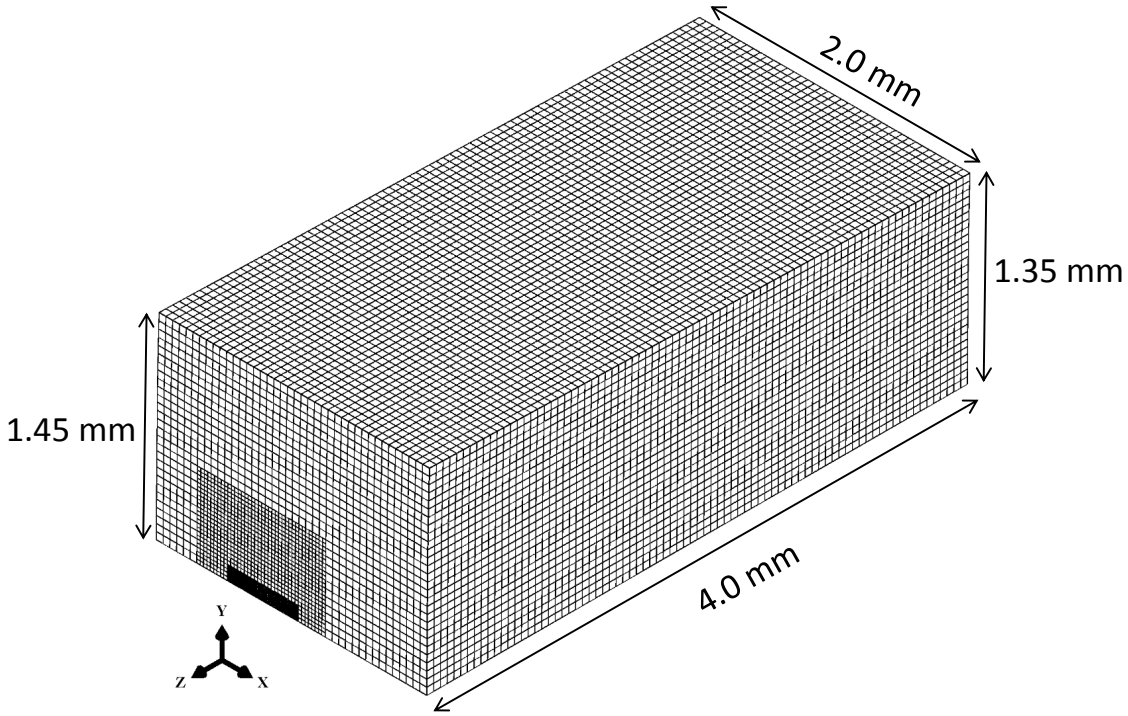

Figure 3-6. Geometry of the submodels of a quarter of a PT specimen.

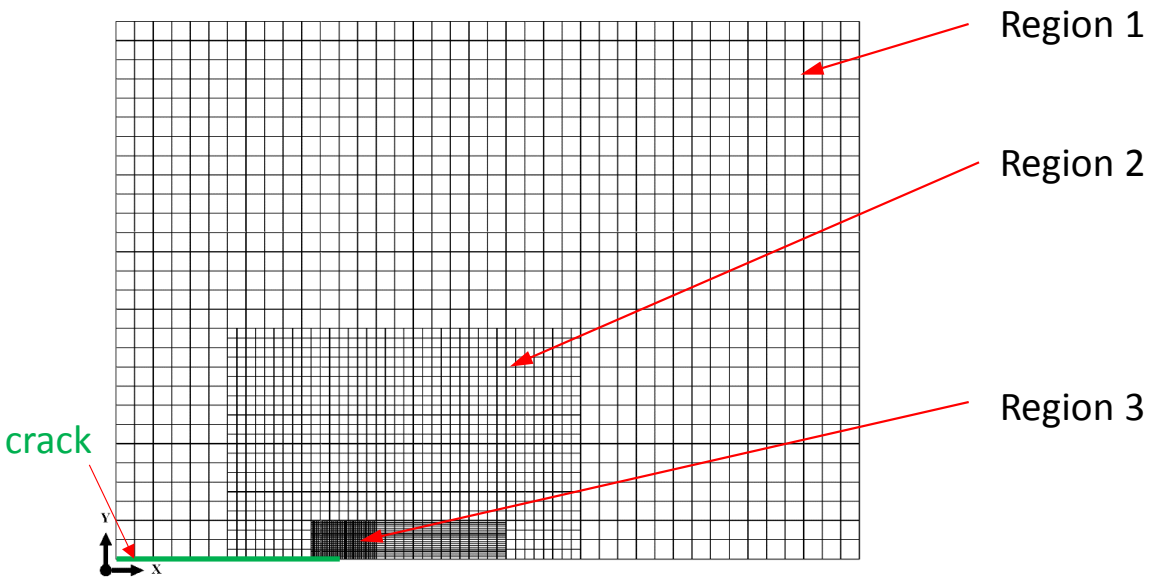

(a)

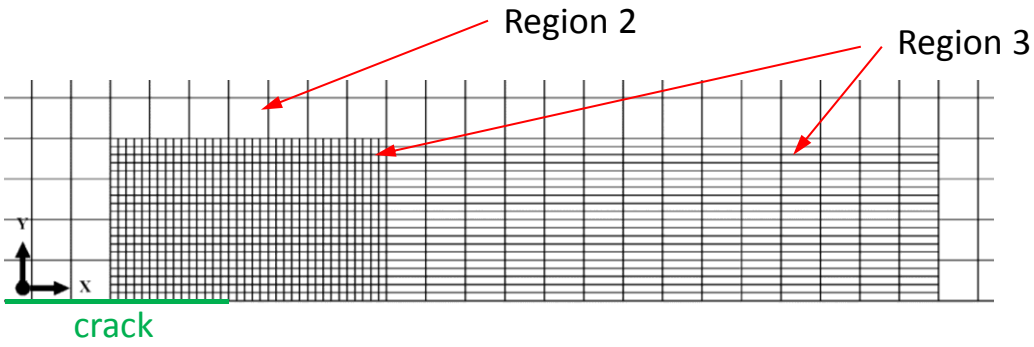

(b)

Figure 3-7. Partition of the regions of different element sizes on the $X-Y$ plane of the submodels.

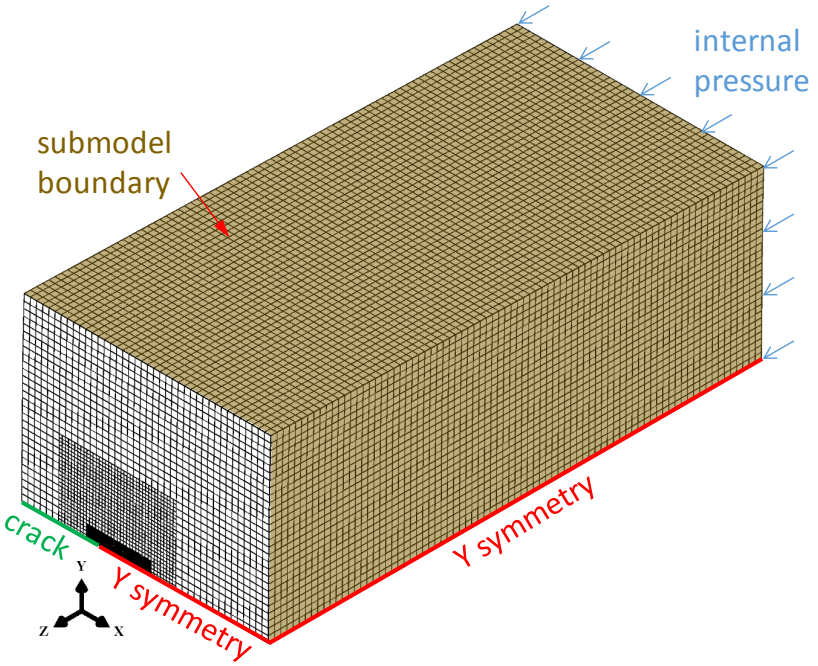

(a)

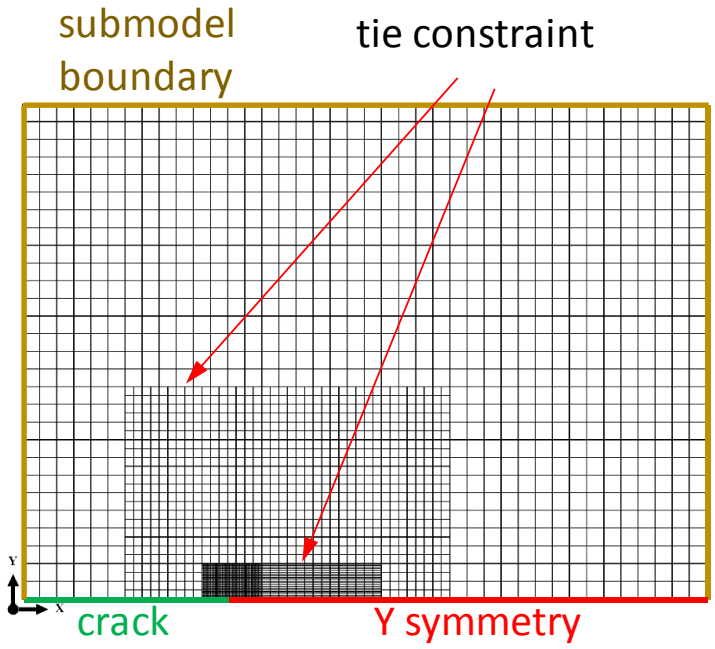

(b)

Figure 3-8. Boundary and constraint conditions of the three-dimensional submodels

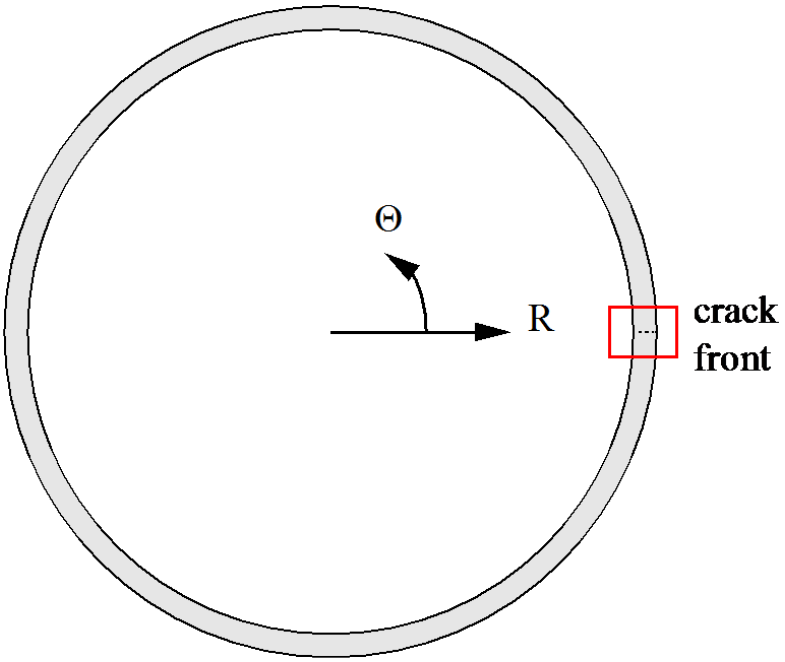

(a)

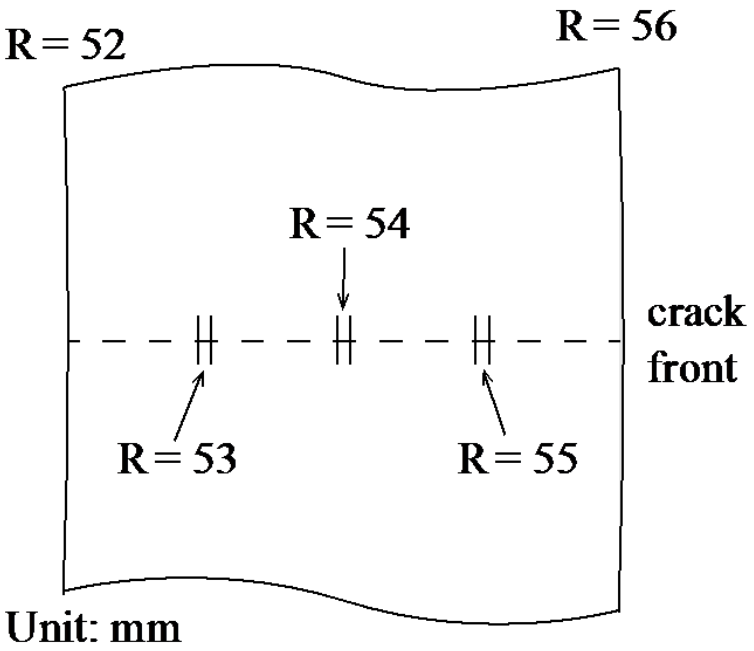

(b)

Figure 3-9. The locations of three pairs of split circumferential hydrides at $R = 53$ mm, $R = 54$ mm and $R = 55$ mm on the axial cross-sectional plane in the submodels.

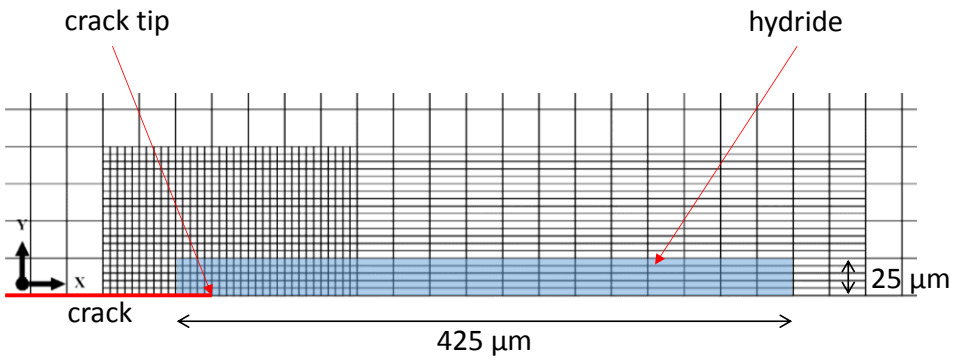

(a)

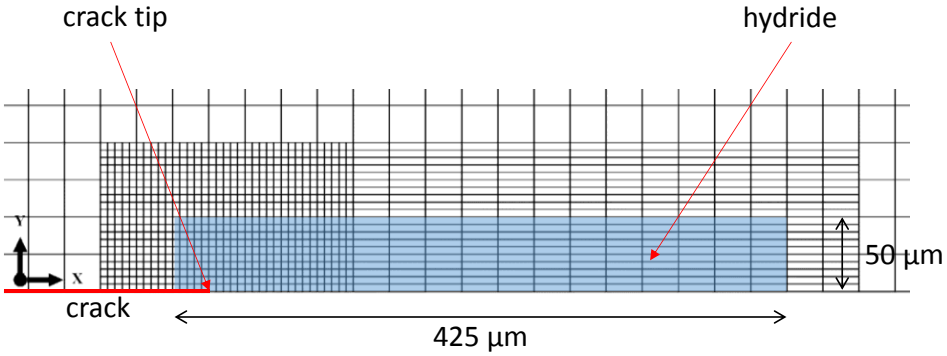

(b)

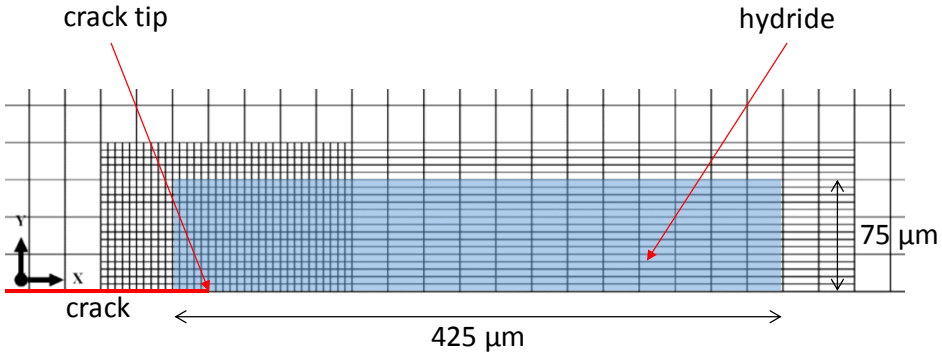

(c)

Figure 3-10. The locations and the sizes of split circumferential hydrides with the heights of (a) 50 µm, (b) 100 µm, and (c) 150 µm on the $X-Y$ plane in the submodels.

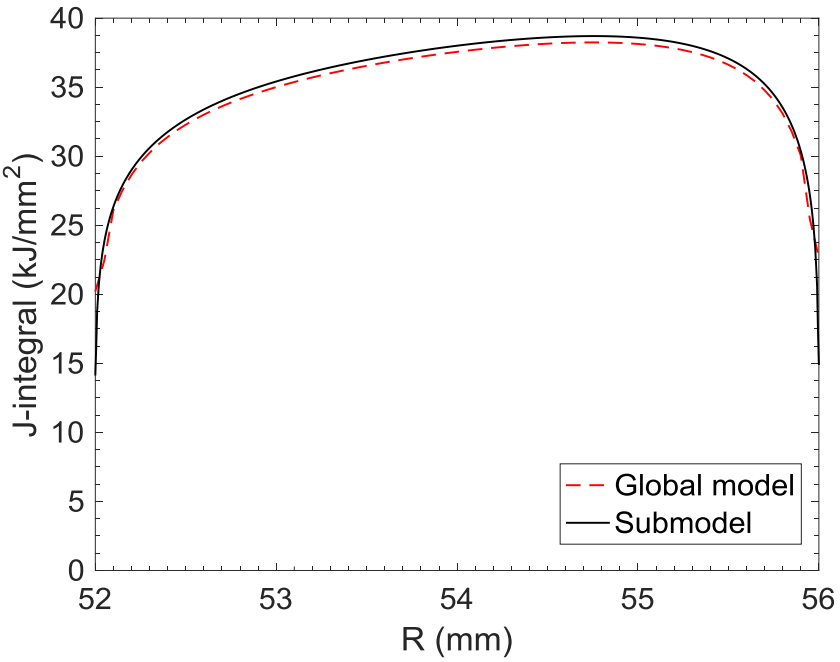

Figure 3-11. The distributions of the computational J-integrals of the global model and the submodel without split circumferential hydrides

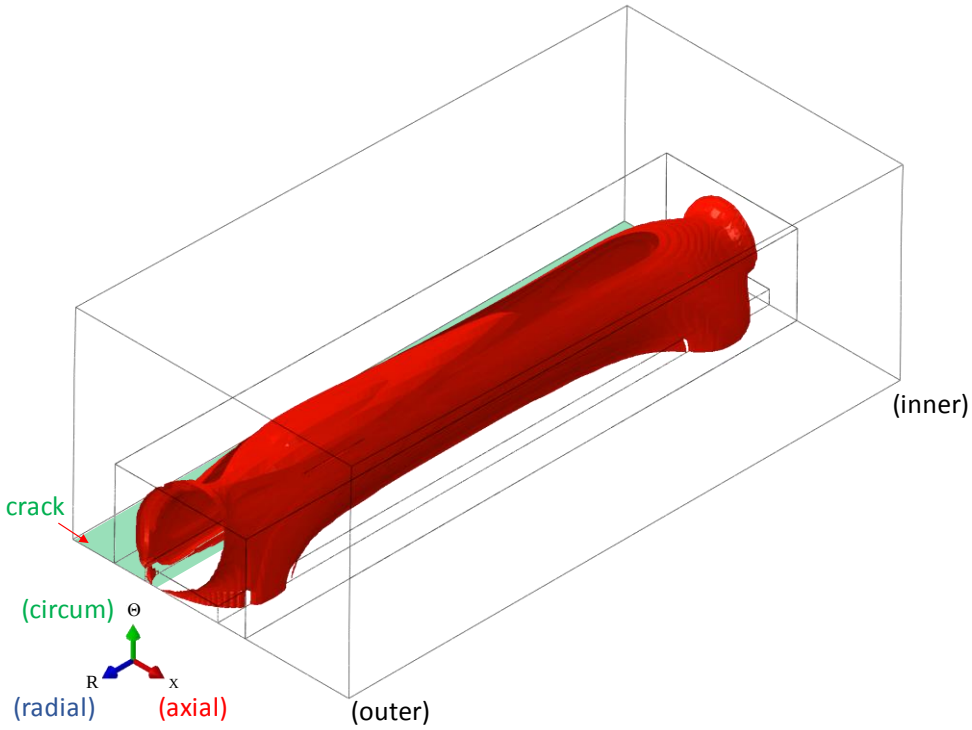

Figure 3-12. The envelope surface of the three-dimensional plastic zone of the submodel without split circumferential hydrides

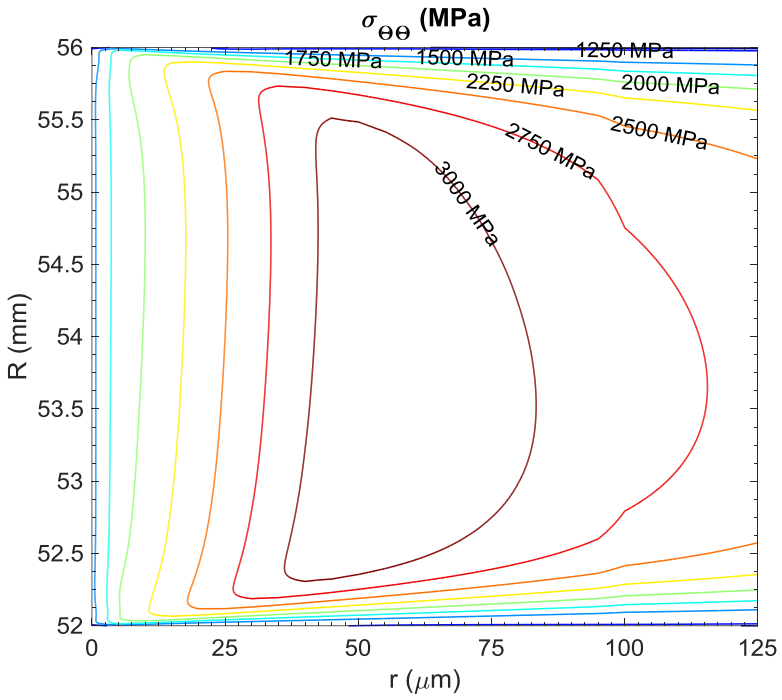

Figure 3-13. The contours of the opening stresses $\sigma_{\Theta\Theta}$ on the crack plane ahead of the crack front

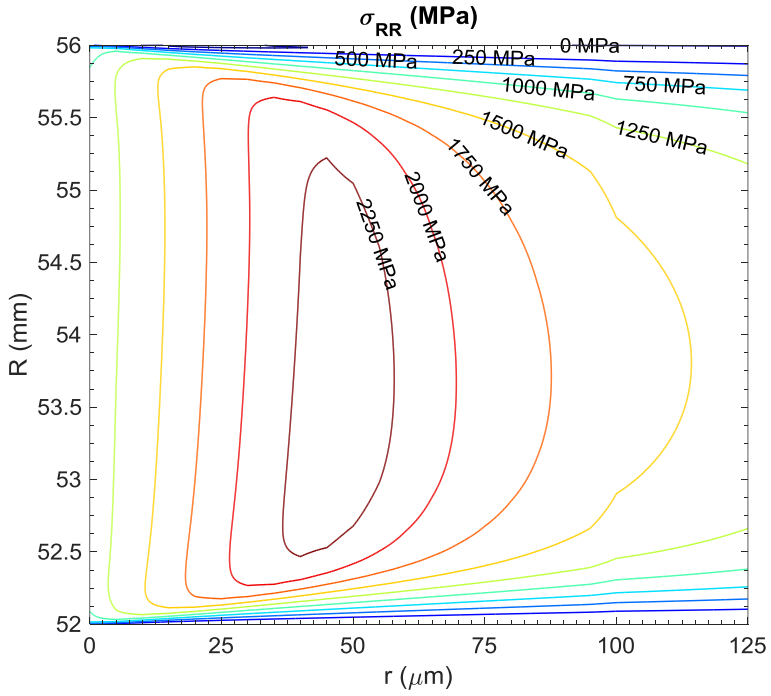

Figure 3-14. The contours of the out-of-plane normal stresses σ_{RR} on the crack plane ahead of the crack front

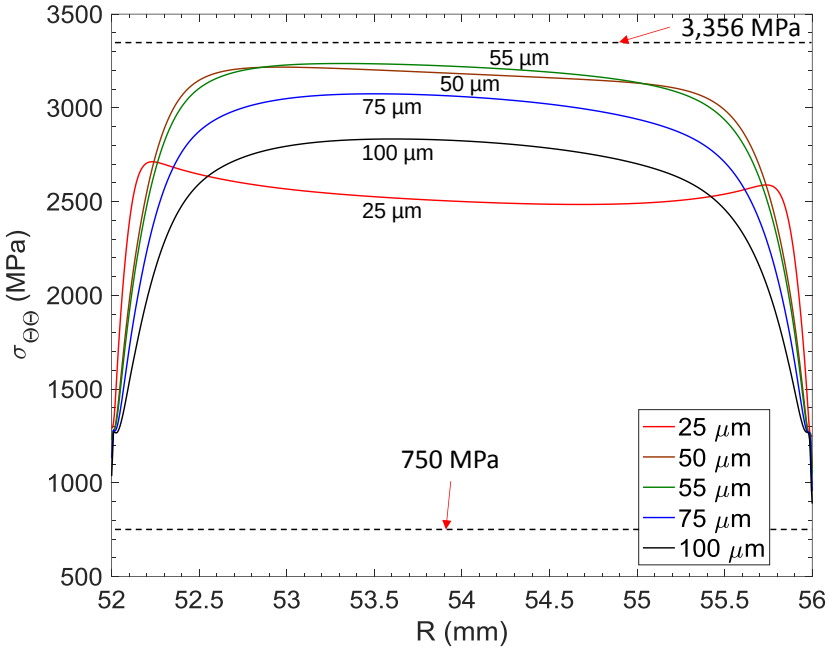

Figure 3-15. The distributions of the opening stresses $\sigma_{\Theta\Theta}$ at different r's in the thickness (R) direction ahead of the crack front.

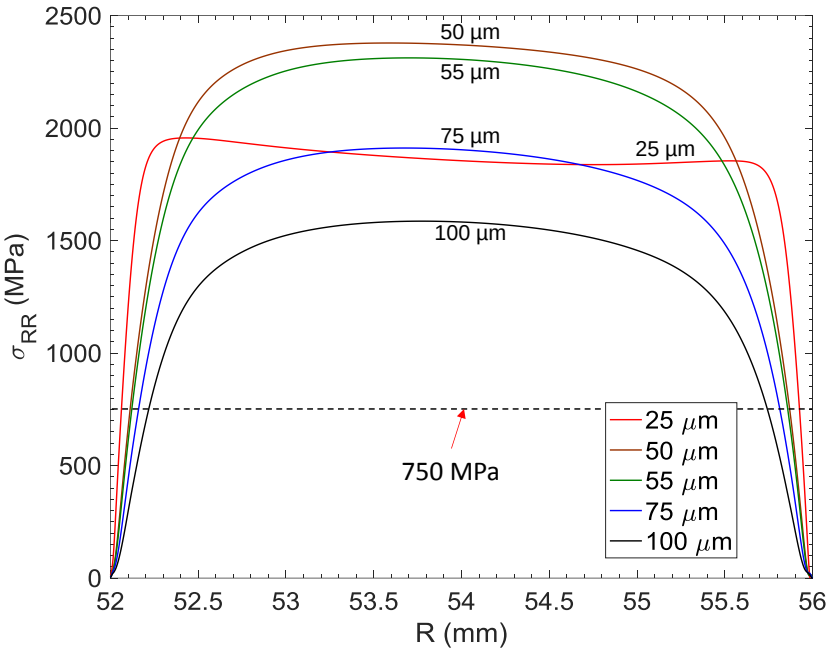

Figure 3-16. The distributions of the out-of-plane normal stresses σ_{RR} at different r's in the thickness (R) direction ahead of the crack front.

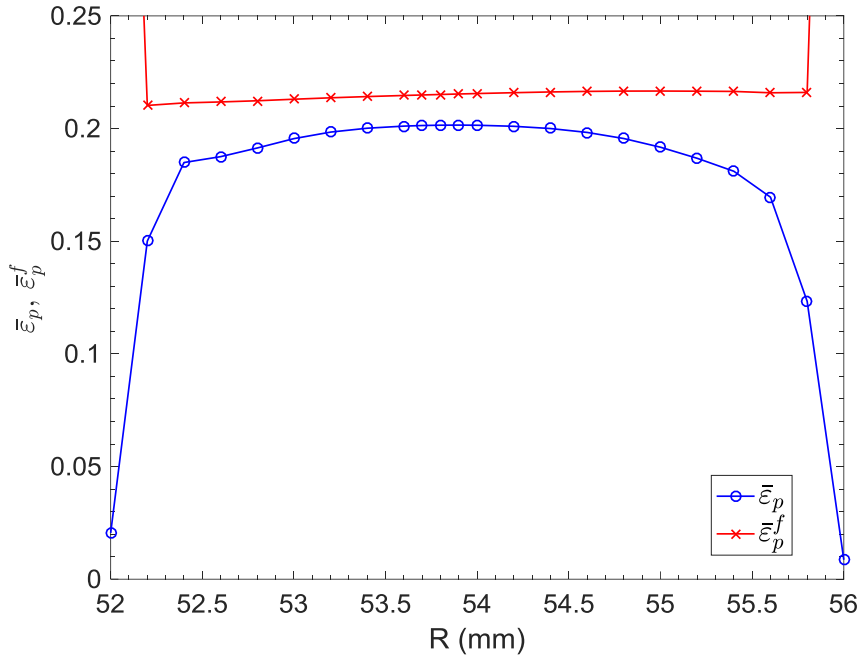

(a)

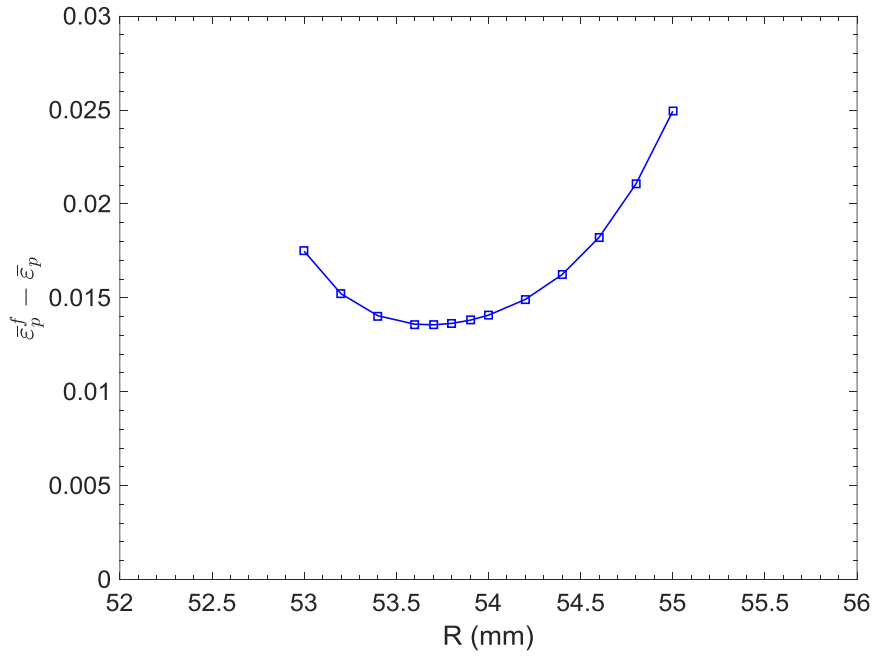

(b)

Figure 3-17. (a) The distributions and (b) the difference of the effective plastic strain $\bar{\varepsilon}_p$ and the failure effective plastic strain $\bar{\varepsilon}_p^f$ in the thickness (R) direction at the radial distance of $r = 15$ μm ahead of the crack front under the given internal pressure p_0.

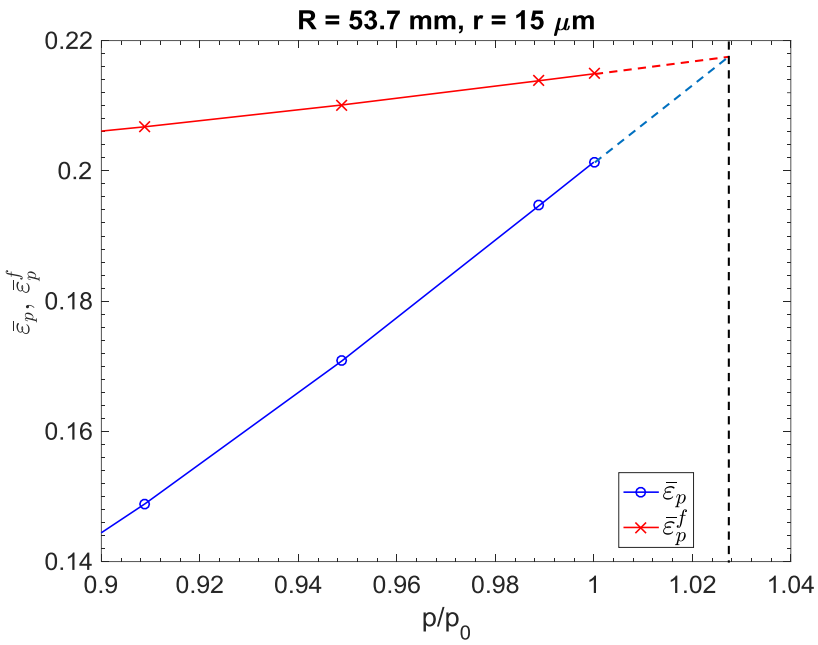

Figure 3-18. The histories of the effective plastic strain $\bar{\varepsilon}_p$ and the failure effective plastic strain $\bar{\varepsilon}_p^f$ at the radial distance of $r = 15$ μm and $R = 53.7$ mm near the end of the application of the normalized internal pressure p / p_0 for a PT specimen without hydride.

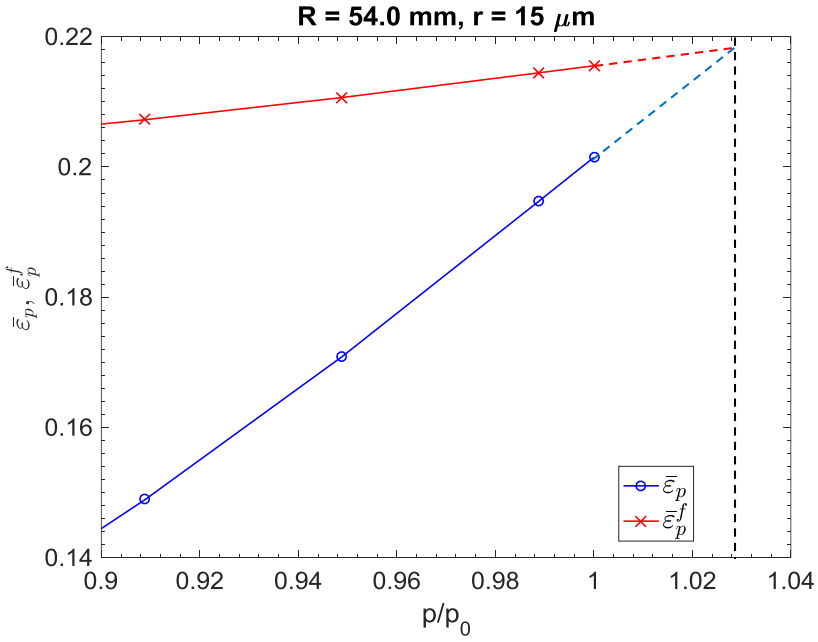

Figure 3-19. The histories of the effective plastic strain $\bar{\varepsilon}_p$ and the failure effective plastic strain $\bar{\varepsilon}_p^f$ at the radial distance of $r = 15$ μm and $R = 54$ mm near the end of the application of the normalized internal pressure p / p_0 for a PT specimen without hydride.

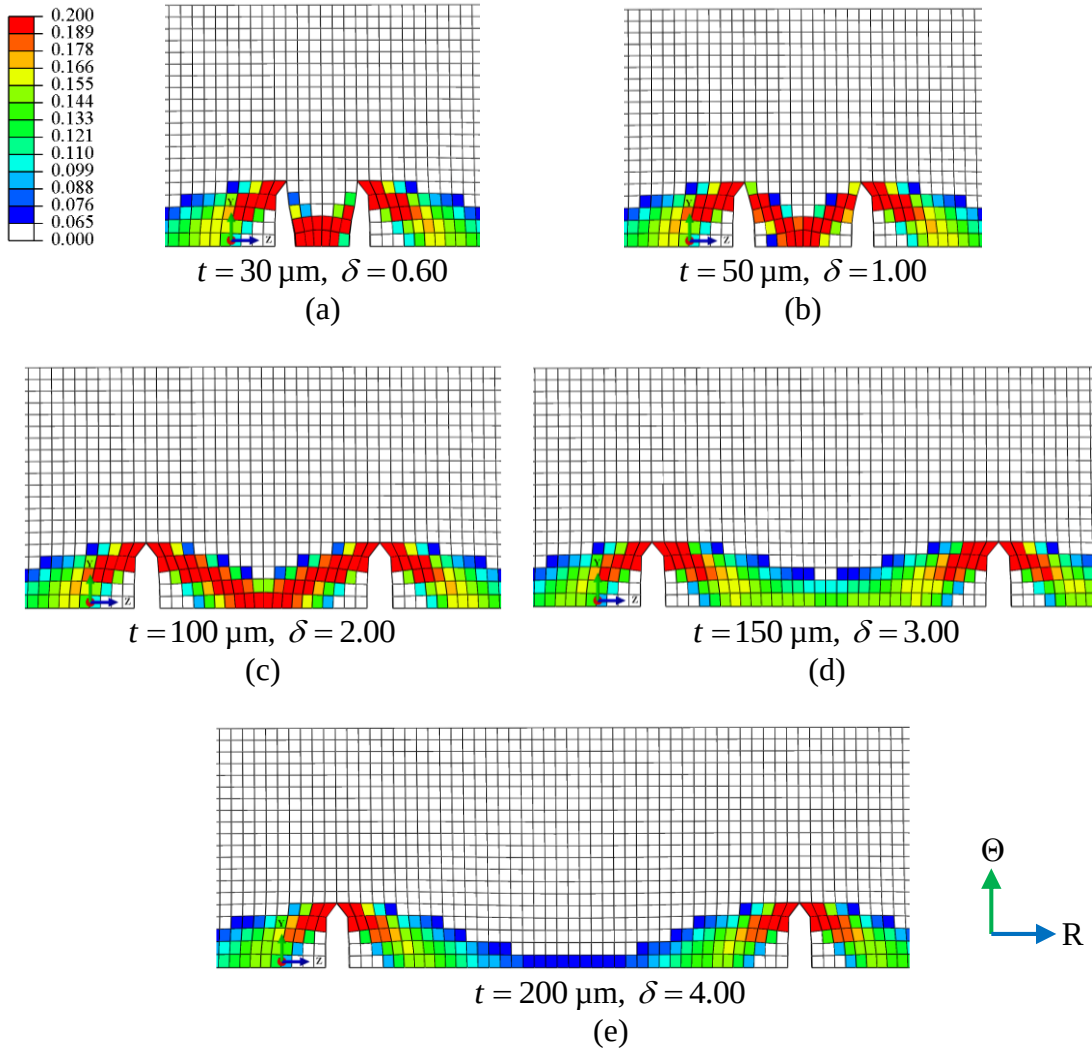

Figure 3-20. The deformed meshes with the magnitudes of the effective plastic strain $\bar{\varepsilon}_p$ for the finite elements marked in colors for the radial-circumferential plane near $R = 54$ mm at the radial distance $r = 15$ μm ahead of the crack front for the PT specimens with hydrides with the height of 50 μm under 60 percent of the applied internal pressure of 6.815 MPa. The ligament thicknesses are (a) 30 μm, (b) 50 μm, (c) 100 μm, (d) 150 μm, and (e) 200 μm.

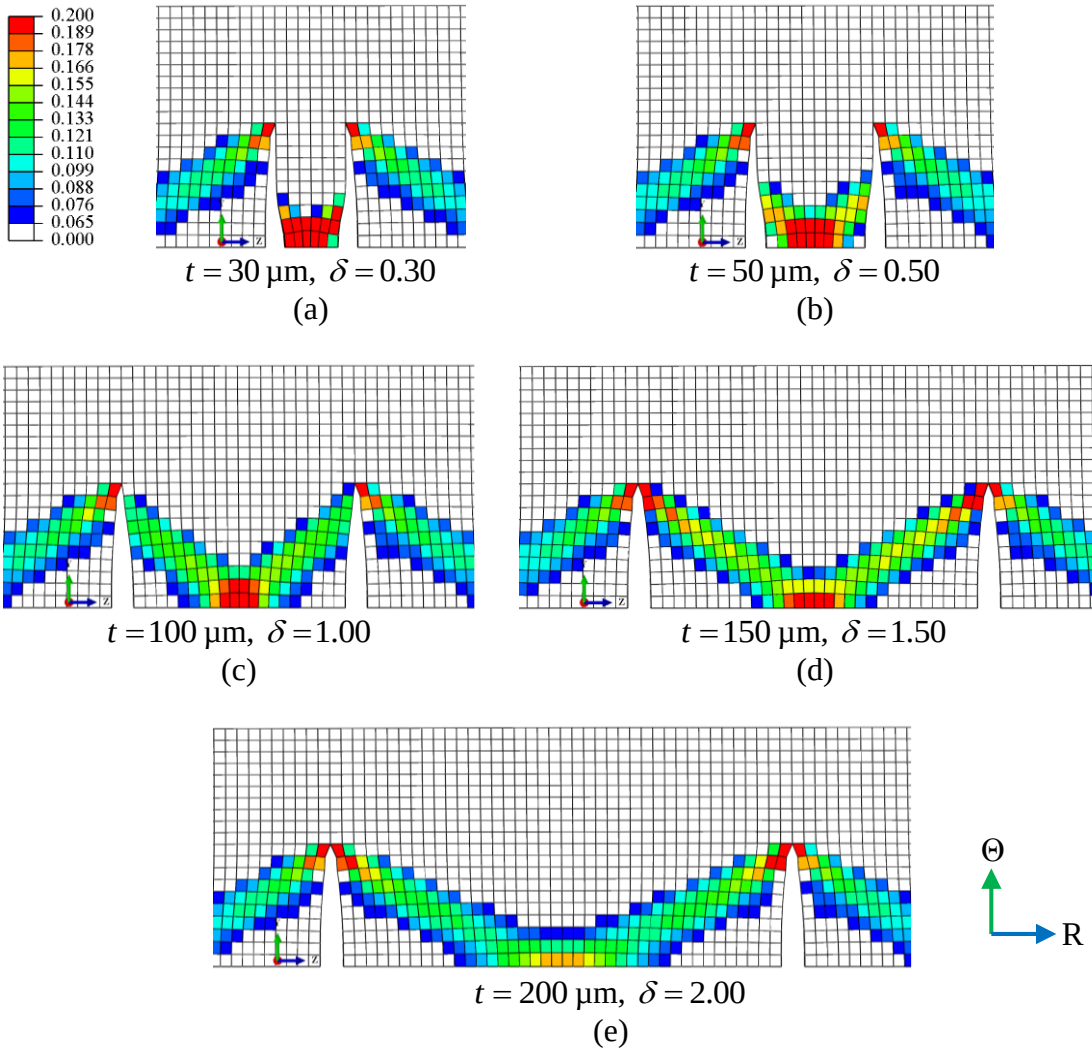

Figure 3-21. The deformed meshes with the magnitudes of the effective plastic strain $\bar{\varepsilon}_p$ for the finite elements marked in colors for the radial-circumferential plane $R = 54$ mm at the radial distance $r = 15$ µm ahead of the crack front for the PT specimens with hydrides with the height of 100 µm under 60 percent of the applied internal pressure of 6.815 MPa. The ligament thicknesses are (a) 30 µm, (b) 50 µm, (c) 100 µm, (d) 150 µm, and (e) 200 µm.

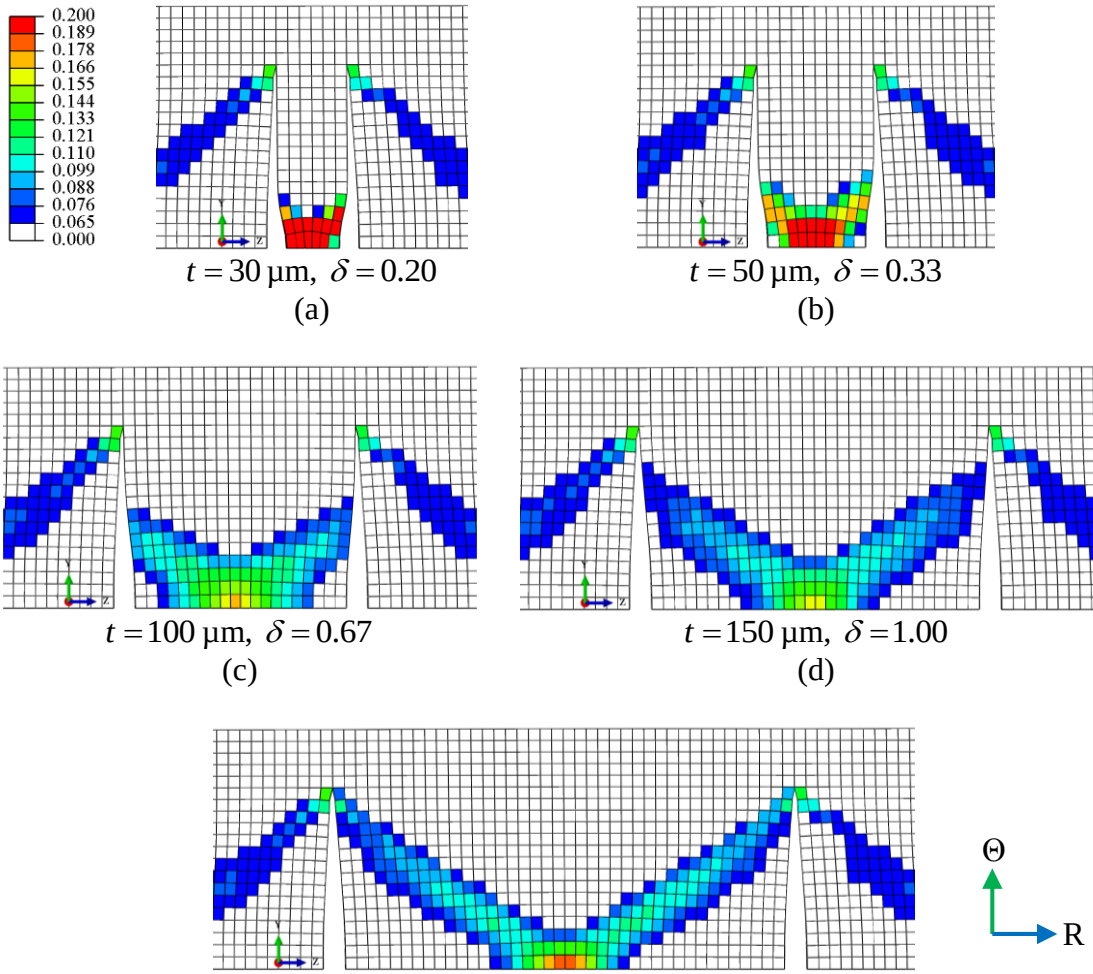

Figure 3-22. The deformed meshes with the magnitudes of the effective plastic strain $\bar{\varepsilon}_p$ for the finite elements marked in colors for the radial-circumferential plane near $R = 54$ mm at the radial distance $r = 15$ µm ahead of the crack front for the PT specimens with hydrides with the height of 150 µm under 60 percent of the applied internal pressure of 6.815 MPa. The ligament thicknesses are (a) 30 µm, (b) 50 µm, (c) 100 µm, (d) 150 µm, and (e) 200 µm.

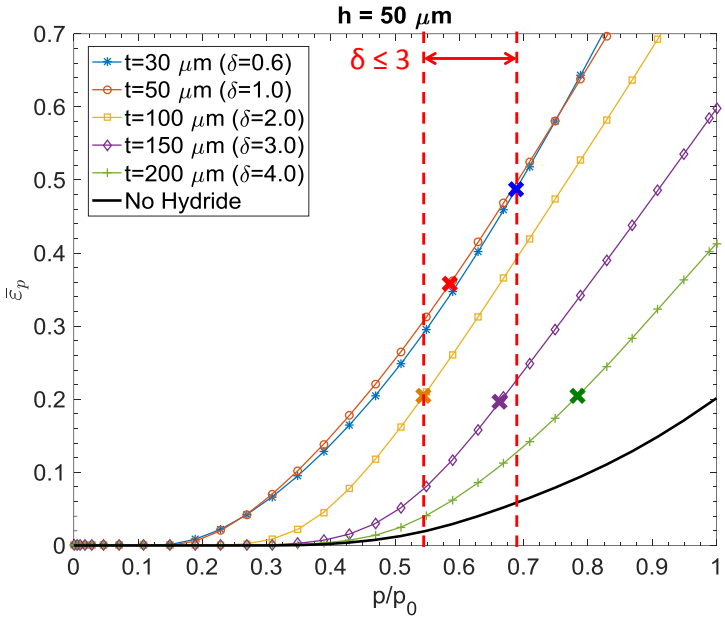

Figure 3-23. The histories of the effective plastic strain $\bar{\varepsilon}_p$ at the radial distance of $r = 15$ μm plotted as functions of the normalized internal pressure p / p_0 for a PT specimen without hydride and PT specimens with split circumferential hydrides with the height of 50 μm and different ligament thicknesses.

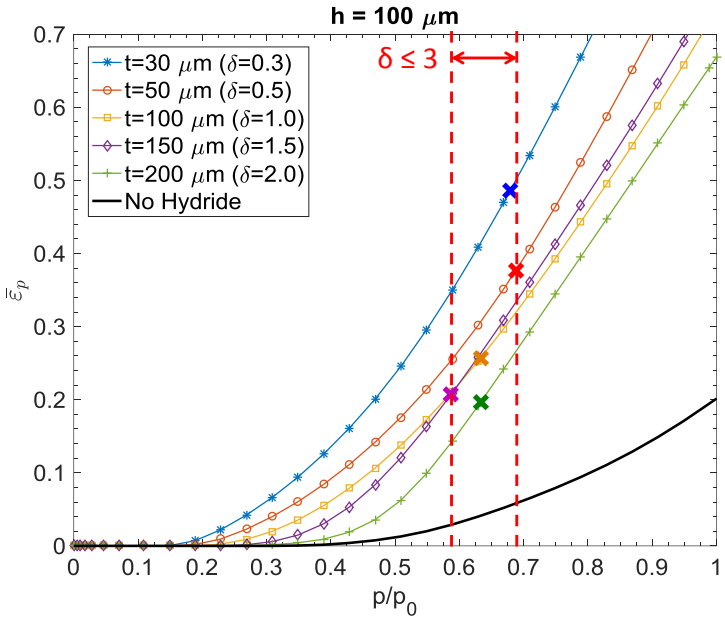

Figure 3-24. The histories of the effective plastic strain $\bar{\varepsilon}_p$ at the radial distance of $r = 15$ μm plotted as functions of the normalized internal pressure p / p_0 for a PT specimen without hydride and PT specimens with split circumferential hydrides with the height of 100 μm and different ligament thicknesses.

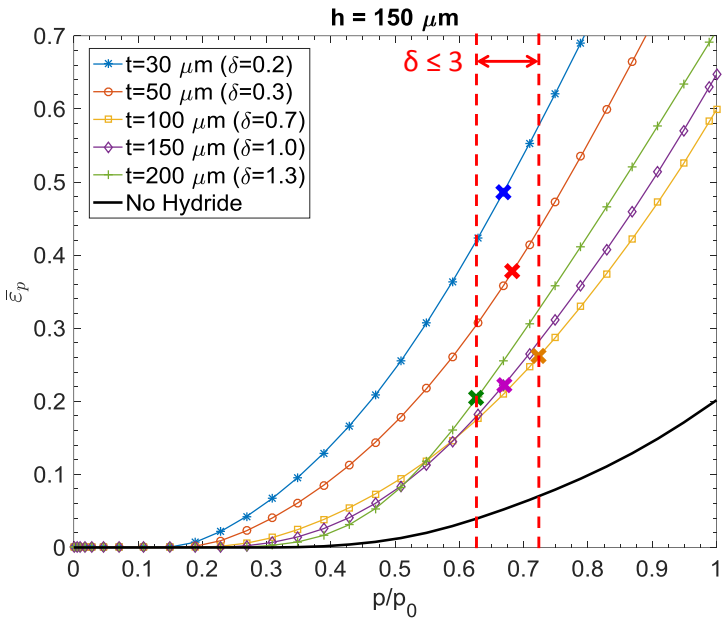

Figure 3-25. The histories of the effective plastic strain $\bar{\varepsilon}_p$ at the radial distance of $r = 15$ μm plotted as functions of the normalized internal pressure p / p_0 for a PT specimen without hydride and PT specimens with split circumferential hydrides with the height of 150 μm and different ligament thicknesses.

Chapter 4 Effects of Curvature on Ductile Fracture Initiation in Curved Compact Tension Specimens of Hydrided Irradiated Zr-2.5Nb Materials with Split Circumferential Hydrides

4.1 Introduction

Fracture toughness values of Zr-2.5Nb are needed for leak-before-break analyses of Zr-2.5Nb pressure tubes in CANDU (CANada Deuterium Uranium) reactors. Practically, the fracture toughness values of Zr-2.5Nb are usually determined by nonstandard curved compact tension (CCT) specimens, machined directly from pressure tubes. The fracture toughness values obtained from CCT specimens should be examined to show that the fracture toughness values obtained from CCT specimens can be used to predict the fracture of pressure tube (PT) specimens. Davies and Shewfelt [13] examined the crack growth resistance (J-R) curves for CCT and PT specimens of irradiated Zr-2.5Nb at 250°C with different concentrations of chlorine, which gave different fracture toughness values. The experimental results showed that the J-R curves are different for the CCT and PT specimens of irradiated Zr-2.5Nb at 250°C with a high concentration of chlorine, which gave low and intermediate fracture toughness, while the J-R curves are close to each other for both CCT and PT specimens of irradiated Zr-2.5Nb at 250°C with a low concentration of chlorine, which gave high fracture toughness. However, the fracture toughness values of PT specimens are significantly larger than those of CCT specimens at 250°C in all cases. St Lawrence [37] also showed that the similar trend of fracture toughness values of CCT and PT specimens of irradiated Zr-2.5Nb at 250°C. However, the experimental results of the fracture toughness values at room temperature are quite consistent, and the fracture

toughness values of PT specimens are only about 10 % larger than those of CCT specimens of irradiated Zr-2.5Nb.

In Chapters 2 and 3, the reduced fracture toughness associated with split circumferential hydrides at room temperature was examined by conducting three-dimensional finite element analyses of compact tension (CT) and PT specimens of irradiated Zr-2.5Nb materials without and with split circumferential hydrides. In Chapter 2, the author proposed a strain-based failure criterion with consideration of stress triaxiality, which can be used to account for the three-dimensional effects on the fracture initiation along the crack fronts in different specimen geometries and different types of loading. The proposed strain-based failure criterion can be used to explain the near 35% reduction of the fracture toughness K_C at room temperature obtained from hydrided irradiated CT and PT specimens when compared with that from unhydrided irradiated ones. However, in Chapters 2 and 3, the load or the internal pressure applied to the CT or PT specimens were calculated based on the same experimental fracture toughness K_C obtained from unhydrided irradiated CCT specimens [37]. A direct comparison of the fracture initiation in CT and CCT specimens based on the strain-based failure criterion with consideration of stress triaxiality has not been examined in Chapters 2 and 3 and will be examined here.

Chow and Simpson [9] experimentally examined the validity of using the nonstandard CCT specimens to determine the fracture toughness. They demonstrated that the values of fracture parameters (initiation toughness, initial tearing modulus and critical crack length) of flattened CT and CCT specimens of unirradiated Zr-2.5Nb were almost identical. They also showed that the front of the stable crack is nearly symmetric in the thickness direction of the CCT specimen. The nearly symmetric crack front profile indicated that the curvature did not

affect the fracture behavior along the crack front significantly in the CCT specimen. A simple elastic bending stress analysis was also presented to examine the effects of the curvature in Chow and Simpson [9]. The results of the elastic analysis indicated the curvature effects on the stress fields are not significant. However, they did not consider the singularities of the stresses and strains along the crack front, the constraint conditions such as the free surface effect and the possible reaction moments on the pin-holes from the loading pins due to the curvature. They did not perform finite element analyses to validate the results of their elastic bending stress analysis along the thickness direction.

In this chapter, a three-dimensional finite element analysis of a CCT specimen of irradiated Zr-2.5Nb materials without hydrides is first conducted with the submodeling strategy established in Sung et al. [39]. The elastic plastic stress-strain relation with a perfectly plastic behavior at large plastic strains used in this investigation is the same as that used for the earlier investigations of CT and PT specimens in Chapters 2 and 3. The computational results are used to examine the effects of the curvature on the J-integral distributions along the crack front, and the stress and strain states ahead of the crack front in the CCT specimen. The effects of the curvature on the plastic zone shapes and sizes along the crack front in the CCT specimen will also be examined for completeness. The critical location along the crack front is determined based on the strain-based failure criterion with consideration of stress triaxiality as established in Chapter 2. The computational results of the CCT specimen are then benchmarked with those of the CT specimen to investigate the effects of the curvature on the fracture initiation loads for the CCT specimens.

Next, three-dimensional finite element analyses of CCT specimens of irradiated Zr-2.5Nb materials with a pair of split circumferential hydrides with various hydride heights and ligament

thicknesses near the critical location along the crack front are then conducted to examine the effective plastic strains and the stress triaxiality in the ligaments between the split circumferential hydrides to determine the fracture initiation loads or fracture toughness values. Following the same strategy established in Chapter 2 with the strain-based failure criterion with consideration of stress triaxiality, the effects of the plastic strain concentration and stress triaxiality in the ligaments on the fracture initiation loads in the CCT specimens of irradiated Zr-2.5Nb materials with hydrides are examined and investigated. Based on the strain-based failure criterion with consideration of stress triaxiality, the fracture initiation loads are determined for CCT specimens with split circumferential hydrides with various heights and ligament thicknesses under the applied load corresponding to the fracture toughness K_C [37], which is the same as that used for CT and PT specimens. Finally, some conclusions are made.

4.2 Finite Element Models

The geometry of the three-dimensional finite element models in this study is based on the geometry of the curved compact tension (CCT) specimens [12] machined from irradiated pressured tubes. The irradiated pressured tube considered here has the inner radius of 51.9 mm and the outer radius of 56.1 mm, which is slightly thicker than that used in the earlier investigation of PT specimens in Chapter 3. Figure 4-1(a) shows a schematic view of a CCT specimen without hydrides. The specimen has the thickness of 4.2 mm and the width of 17 mm. The total crack length is 8.75 mm including the fatigue crack length of 2 mm. Figure 4-1(b) shows a schematic view of a CCT specimen with circumferential hydrides. The left figure in Figure 4-1(b) schematically shows a side view of the CCT specimen with a rectangular circumferential hydride. The right figure in Figure 4-1(b) schematically shows a front view of

the CCT specimen with a pair of circumferential hydrides. The circumferential hydrides are assumed to have already split so that the split circumferential hydrides are considered as transverse cracks. Due to the symmetry of the CCT specimen, only the upper half of a CCT specimen was modeled. In order to investigate the effects of split circumferential hydrides on the fracture behavior ahead of the front of a crack in a hydrided irradiated CCT specimen, submodeling strategy established in the earlier investigation of CT specimens [39] was used in this investigation.

In this investigation, finite element models were built based on the flat finite element models used for modeling a CT specimen without the curvature in Chapter 2. The additional nodal translation in the Z direction was performed to generate the required curvature. Figure 4-2 shows the geometry and the mesh of the global finite element model of the upper half of a CCT specimen for three-dimensional finite element analyses. The global X, Y and Z coordinates are also plotted in the figure. The Y symmetry boundary condition was imposed on the bottom surface of the model, as shown in Figure 4-3. For convenient presentation of the computational results, a polar coordinate system is introduced in Figure 4-3. The $R-\Theta$ coordinate system is defined on the axial cross-sectional planes of the original pressure tube. The inner surface is set at $R = 51.9$ mm and the outer surface is set at $R = 56.1$ mm. The details of the mesh design were already presented in Chapter 2 and will not be repeated here. The total number of the elements for the global model is 227,526. In order to study the effects of split circumferential hydrides with various hydride heights and ligament thicknesses on the fracture initiation in the CCT specimens, several submodels were built with the same geometry. The geometry and the mesh of a submodel are shown in Figure 4-4. The submodel boundaries, where the displacements are acquired from the analyses of the corresponding global model, and

the Y symmetry boundary condition are also shown in Figure 4-5. The determination of the size of submodels and the details of the mesh design were already discussed in Chapter 2 and will not be repeated here. The total number of elements for each submodel is 1,048,404.

Split circumferential hydrides are modeled by separating elements where the hydrides are located. A pair of split circumferential hydrides are assumed to be located where the earliest fracture initiation occurs near $R = 53.1$ mm based on the failure criterion defined in Chapter 2. The determination of the fracture initiation location will be discussed later in this paper. Since only a half of a CCT specimen is considered in this study, only the upper halves of split circumferential hydrides are modeled. The locations of the split circumferential hydrides with three different sizes of 425 μm by 50 μm, 425 μm by 100 μm and 425 μm by 150 μm on the $X-Y$ plane are shown in Figures 4-6(a), (b) and (c), respectively. The hydride dimensions were selected based on the experimental observations of the circumferential hydrides with the dimension in the axial direction larger than the dimensions in the other two directions [27,33]. Different ligament thicknesses between split circumferential hydrides considered in this investigation are 30, 50, 100, 150, and 200 μm. These different ligament thicknesses are simulated by controlling the distance between two split circumferential hydrides.

The irradiated Zr-2.5Nb material behavior used in this investigation is the same as that for CT and PT specimens in Chapters 2 and 3. The Young's modulus is taken to be 102.1 GPa and the Poisson's ratio is taken to be 0.4. The plastic hardening curve is based on fitting the experimental results of transverse tensile tests at room temperature by a three-dimensional finite element analysis as shown in Figure A-3. As show in Figure A-3, the plastic strain appears at the yield stress of 1,095 MPa and the material has some hardening at small plastic strain. When the plastic strain is large, the material behaves as perfectly plastic material with the maximum true

stress of 1,129 MPa. The plastic anisotropy of the irradiated Zr-2.5Nb material is not considered in this investigation and will be considered in the future. A load P_0 of 3,206 N is applied, which corresponds to K_C = 59.2 $\text{MPa}\cdot\sqrt{\text{m}}$ [37] based on the ASME E399 [4]. The same value of K_C was also used for CT and PT specimens in Chapters 2 and 3. The commercial finite element program ABAQUS was employed to perform the computations. First-order three-dimensional elements with reduced integration (C3D8R) were used exclusively in this study. The option of the geometric nonlinearity is set to off in the elastic analyses and is turned on in the elastic-plastic analyses.

4.3 Computational Results

4.3.1. Curved Compact Tension Specimen without hydrides

In Chapter 2, the author has already indicated that the set of the global model and submodel is adequate for the three-dimensional finite element analyses of the quarter CT specimen under the similar loading conditions. Due to the existence of the curvature, the set of the global model and submodel of the half CCT specimen should be examined again based on the submodeling strategy established in [39]. Figure 4-7 shows the consistency of the distributions of the computational J-integrals in the thickness direction from the elastic analyses of the global model and the submodel without hydrides under the applied load P_0 of 3,206 N. The horizontal axis R represents the location of the crack front in the thickness direction of the CCT specimen. As shown in Figure 4-7, the maximum value of the J-integral occurs close to the inner surface near $R = 53.1$ mm, not in the middle of the specimen thickness. Figure 4-8 shows the envelope surface of the three-dimensional plastic zone in the submodel from the elastic-plastic analysis. The plastic zone is enclosed in the fine mesh region of the submodel. Slight

discontinuities of the envelope surface of the plastic zone occur where the envelope surface crosses the interfaces between two regions with different mesh sizes. Based on the discussions above, this set of the global model and submodel is also adequate for the three-dimensional finite element analyses of the half CCT specimen [39]. As shown in Figure 4-8, the largest plastic zone size on the axial-circumferential plane is not located on the inner or outer surface. Instead, the largest plastic zone size is located near the inner surface.

The effect of the curvature is first investigated with the results of the elastic computational analyses. Figure 4-9(a) shows a comparison of the distributions of the computational J-integrals of the CT and CCT specimens without hydrides under the same load P_0. Near the middle of the specimens, the values of J-integrals of the CT and CCT specimens are quite consistent. However, due to the curvature, the distribution of the J-integral of the CCT specimen is asymmetric. The J-integral is higher in the inner half part and lower in the outer half part when compared to those of the CT specimen. In addition, the percentage of the difference of the maximum J-integrals is 3.97%. For completeness, the distributions of the mode I stress intensity factor K_I solutions along the crack front in the CT and CCT specimens are also plotted in Figure 4-9(b). As shown in the figure, the distributions of the K_I solutions are quite similar to those of the J-integrals with smaller values near the free surfaces. The percentage of the difference of the maximum K_I solutions is 1.97%. It should be mentioned that the elastic beam analysis of Chow and Simpson [9] indicated that the bending stress of CCT specimens can be 6.9% larger than that of CT specimens. Figures 4-10(a) and (b) show the differences of the J-integrals and K_I solutions, respectively, of the CCT and CT specimens without hydrides. The maximum differences are both located close to the inner surface. The nearly anti-symmetric difference indicates that an extra moment works on the crack plane ahead of the crack front, and

the extra moment is in the positive X (axial) direction, as shown in Figure 4-2. In addition, the action line of the extra resultant moment is not exactly located at the middle of the thickness (2.1 mm from the inner surface) but slightly closer to the outer surface (2.2 mm from the inner surface). Therefore, the effect of the curvature on J-integrals is slightly larger for the inner half part than the outer half part, as shown in Figure 4-10, from the viewpoint of the beam or plate bending theory.

The effect of the curvature is then investigated with the results of the elastic-plastic computational analyses. Figures 4-11 and 4-12 shows the contours of the opening stress $\sigma_{\Theta\Theta}$ and the out-of-plane normal stress σ_{RR} on the crack plane ahead of the crack front, respectively, from the computational elastic-plastic analyses. The magnitudes and locations of the maximum $\sigma_{\Theta\Theta}$ and σ_{RR} have also been marked in the figures. The radial distance r is the distance from the crack front in the X (axial) direction on the crack plane. The range of interest of r in this study is from $r = 0$ μm to $r = 125$ μm. As shown in Figures 4-11 and 4-12, the contours closer to the inner surface advance more in the X direction due to the curvature. The largest opening stress $\sigma_{\Theta\Theta}$ and the largest out-of-plane normal stress σ_{RR} occur at the radial distances of about $r = 60$ μm and $r = 50$ μm, respectively, and near the middle of the CCT specimen, which are very similar to those for the CT specimen in Chapter 2. This indicates that the magnitudes and locations of the largest opening stress $\sigma_{\Theta\Theta}$ and the largest out-of-plane normal stress σ_{RR} are not affected significantly by the curvature from the elastic-plastic computational analysis.

In order to clearly show the magnitudes of the stresses ahead of the crack front, the distributions of the opening stress $\sigma_{\Theta\Theta}$ and the out-of-plane normal stress σ_{RR} are also plotted at different radial distance r's ahead of the crack front in the thickness direction in Figures 4-13 and 4-14, respectively. The opening stress $\sigma_{\Theta\Theta}$ at $r = 60$ μm ranging from $R = 52.5$ mm to

$R = 55$ mm is quite close to the theoretical value of 3,351 MPa derived from the slip line theory for rigid perfectly plastic materials under plane strain conditions. For this case, the maximum stress of 1,129 MPa in Figure A-3 is taken as the yield stress of the perfectly plastic materials. The maximum opening stress is equal to 1,129 MPa times $(2+\pi)/\sqrt{3}$ [26]. This gives the maximum opening stress equal to 3,351 MPa. This means that the stress state near the middle portion of the crack front is close to that of the plane strain conditions under the applied load. With the hydride fracture stress of 750 MPa [28] plotted as dash lines in Figures 4-13 and 4-14, the distributions of the opening stress $\sigma_{\Theta\Theta}$ and the out-of-plane normal stress σ_{RR} indicate that all radial hydrides ahead of the crack front will fracture, and circumferential hydrides ahead of the crack front will split in the middle portion of specimen but they will not split near the inner and outer surfaces. The size of the zone without split circumferential hydrides increases with the increasing radial distance r from the crack front. The same phenomenon can also be observed in the corresponding micrograph of St Lawrence [36] as discussed in Chapter 2.

Due to the complicated distributions of the stresses ahead of the crack front and the J-integral along the crack front in the CCT specimen, the location of the earliest fracture initiation is not necessary in the middle of the specimen. In order to determine the location of the earliest fracture initiation, the strain-based failure criterion with consideration of stress triaxiality used in Chapters 2 and 3 is adopted in this investigation. The failure effective plastic strain $\bar{\varepsilon}_p^f$ as a function of the stress triaxiality α is plotted in Figure 2-24. The details for the development of the strain-based failure criterion with consideration of stress triaxiality based on the Gurson yield model and the work of Bao and Wierzbicki [5] are presented in Chapter 2. Only some necessary information will be repeated here for completeness. The stress triaxiality α is defined as

$$\alpha = \frac{\sigma_m}{\sigma_e} \tag{4-1}$$

where σ_m $(=\sigma_{kk}/3)$ represents the hydrostatic tension, and σ_e $(=\sqrt{3\sigma'_{ij}\sigma'_{ij}/2}\,)$ is the tensile effective stress which is based on the second invariant of the deviatoric stress tensor σ'_{ij} ($=\sigma_{ij}-\sigma_{kk}\delta_{ij}/3$). In order to account for the effect of changing stress triaxiality α during the deformation history for a material element of interest, the Gurson model approach or the average stress triaxiality approach of Bao and Wierzbicki [5] should be considered. In Chapter 2, the author has shown that the results of the Gurson model approach and the average stress triaxiality approach [5] are consistent with each other to correlate to the fracture initiation in CT specimens without hydrides. In this investigation, the average stress triaxiality approach is adopted for efficient post-processing.

The average stress triaxiality $\bar{\alpha}$ proposed in [5] is defined as

$$\bar{\alpha} = \frac{1}{\bar{\varepsilon}_p^{\,f}} \int_0^{\bar{\varepsilon}_p^{\,f}} \alpha \, d\bar{\varepsilon}_p \tag{4-2}$$

Here, $\bar{\varepsilon}_p^{\,f}$ represents the failure effective plastic strain. Figure 4-15(a) shows the effective plastic strain $\bar{\varepsilon}_p$ and the failure effective plastic strain $\bar{\varepsilon}_p^{\,f}$ (based on the average stress triaxiality $\bar{\alpha}$) plotted as functions of the distance to the inner surface ranging from 0 mm to 4.2 mm at the radial distance of $r = 15$ μm ahead of the crack front in the CT and CCT specimens without hydrides under the applied load P_0 of 3,206 N corresponding to K_C = 59.2 $\text{MPa}\cdot\sqrt{\text{m}}$. For the CCT specimen, the effective plastic strain $\bar{\varepsilon}_p$ is already larger than the failure effective plastic strain $\bar{\varepsilon}_p^{\,f}$ in the range of 0.5 mm to 2 mm in Figure 4-15(a). That means the CCT specimen fails before the applied load P_0 reaches 3,206 N. For the CT specimen, the effective plastic strain $\bar{\varepsilon}_p$

and the failure effective plastic strain $\bar{\varepsilon}_p^f$ are not equal to each other but have a small difference in the middle of the CT specimen, as shown in Figure 4-15(a). The small difference comes from that the strain-based failure criterion with consideration of stress triaxiality was fitted based on the Gurson model approach in Chapter 2. However, the average stress triaxiality approach is adopted in this investigation for calculating the failure effective plastic strain $\bar{\varepsilon}_p^f$ for efficient post-processing. Figure 4-15(b) clearly shows the differences between the effective plastic strain $\bar{\varepsilon}_p$ and the failure effective plastic strain $\bar{\varepsilon}_p^f$ ranging from 0.5 mm to 3.5 mm where the differences are relatively small. As shown in the figure, the minimum difference of -0.7% for the CCT specimen occurs at the radial distance of $r = 15$ μm and $R = 53.1$ mm. Due to the different methods between fitting and applying the failure criteria, the minimum difference of 0.4% for the CT specimen occurs at the radial distance of $r = 15$ μm and the middle of thickness. Both minimum differences are small.

In order to further quantify these small differences, the histories of the effective plastic strain $\bar{\varepsilon}_p$ and the failure effective plastic strain $\bar{\varepsilon}_p^f$ at the radial distance of $r = 15$ μm and $R = 53.1$ mm near the end of the application of the normalized load P / P_0 for a CCT specimen without hydrides was first plotted in Figure 4-16. As shown in Figure 4-16, only 98.7% of the applied load P_0 is enough for the effective plastic strain $\bar{\varepsilon}_p$ to reach the failure effective plastic strain $\bar{\varepsilon}_p^f$. Figure 4-17 shows the histories of the effective plastic strain $\bar{\varepsilon}_p$ and the failure effective plastic strain $\bar{\varepsilon}_p^f$ at the radial distance of $r = 15$ μm and the middle of thickness for a CT specimen without hydrides. Figure 4-17, the dashed red and blue lines represent the anticipated histories of $\bar{\varepsilon}_p^f$ and $\bar{\varepsilon}_p$, respectively, when the normalized load P / P_0 is larger than

1.0. As shown in Figure 4-17, only additional 0.7% of the applied load P_0 is enough for the effective plastic strain $\bar{\varepsilon}_p$ to reach the failure effective plastic strain $\bar{\varepsilon}_p^f$. This small difference of 0.7% of the applied load justifies the application of the average stress triaxiality approach, as discussed in Chapter 2. It should be mentioned that with the same strain-based failure criterion with consideration of stress triaxiality, the CT specimen almost fails (fails at 100.7% of the applied load) and the CCT specimen fails slightly earlier at 98.7% of the applied load under the same applied load of 3,206 N. It means that with consideration of the plastic deformation, the applied load for fracture initiation is 2% lower than that of the CT specimen based on the strain-based failure criterion with consideration of stress triaxiality. The value of 2% is very similar to the percentage of the difference of 1.97% of the maximum K_I solutions of the CCT and CT specimens as discussed earlier, although the physical bases and the fracture initiation locations are quite different for the two approaches.

In Chapter 3, the author has shown that with the same strain-based failure criterion used in this investigation, the fracture initiation of a pressure tube (PT) specimen requires additional 3% of the applied internal pressure corresponding to K_C = 59.2 $\mathrm{MPa}\cdot\sqrt{\mathrm{m}}$. The earlier discussion showed that the fracture initiation of a CCT specimen requires only 98.7% of the applied load corresponding to the same K_C. These two computational results indicate that the actual fracture toughness for fracture initiation in a PT specimen is about 4.3% higher than that for a CCT specimen. The trend of the percentage difference of 4.3% between the fracture toughness for CCT and PT specimens is the same as the trend of the experimental results of 10% [37]. This comparison demonstrates that the strain-based failure criterion with consideration of stress triaxiality can describe the slightly higher fracture toughness for fracture initiation in a PT specimen due to different constraint conditions, compared with that for a CCT specimen at room

temperature. In the later investigation of the CCT specimen with split circumferential hydrides, the location of $R = 53.1$ mm is chosen to represent where the earliest fracture initiation occurs in the thickness direction.

4.3.2. Curved Compact Specimen with Split Circumferential Hydrides

One pair of split circumferential hydrides with various heights and ligament thicknesses ahead of the crack fronts is considered at $R = 53.1$ mm, where the earliest fracture initiation occurs as discussed earlier. For the pair of split circumferential hydrides with various heights and ligament thicknesses, the deformed meshes with the magnitudes of the effective plastic strain $\bar{\varepsilon}_p$ for the finite elements marked in colors for the radial-circumferential ($Z-Y$ or $R-\Theta$) plane near $R = 53.1$ mm at the radial distance $r = 15$ μm ahead of the crack front under 60 percent of the applied load P_0 of 3,206 N are shown in Figures 4-18 to 4-20. Note that the radial distance of interest of $r = 15$ μm is three elements away from the crack front, which is consistent with that in the earlier investigation of CT and PT specimens in Chapters 2 and 3. Figures 4-18(a) to (e) show the deformed meshes, colored based on the magnitudes of the effective plastic strain $\bar{\varepsilon}_p$, for the CCT specimens with split circumferential hydrides with the height of 50 μm and the ligament thicknesses of 30, 50, 100, 150, and 200 μm, respectively. In Figure 4-18, the red color represents the regions where the effective plastic strain is larger than 20% while the white color represents the regions where the effective plastic strain is less than 6.5%. With the same designations of colors for the effective plastic strains for the finite elements, Figures 4-19 and 4-20 show the deformed meshes of the CCT specimens with hydrides with the heights of 100 μm and 150 μm, respectively. In Figures 4-18 to 4-20, the inner surface is on the left side of the figures and the outer surface is on the right side of the figures.

In the investigation of CT specimens in Chapter 2, three types of strain concentration were identified and discussed. In this investigation, the same three types of strain concentration can also be identified in Figures 4-18 to 4-20. The type of strain concentration can be categorized by the ligament thickness ratio δ. The ligament thickness ratio δ is defined as

$$\delta = \frac{t}{h} \tag{4-3}$$

where t represents the ligament thickness and h represents the hydride height. For small ligament thickness ratios with $\delta \leq 1$, strain concentration occurs in the middle of the ligament and then shear localization emanates from it, as shown in Figures 4-18(a) to (b), Figures 4-19(a) to (c) and Figures 4-20(a) to (d). For the cases of the ligament thickness t comparable to the hydride height h with $1 < \delta \leq 2$, in addition to the strain concentration in the middle of the ligament, shear localization also emanates from the tips of the split circumferential hydrides at the angle slightly smaller than 45 degrees with respect to the radial-axial plane. Two types of shear localization emanate from different sources and then connect with each other to cross the entire ligament, as shown in Figure 4-18(c), Figures 4-19(d) to (e) and Figure 4-20(e). For large ligament thickness ratios with $\delta > 2$, shear localization emanates only from the tips of the split circumferential hydrides at the angle slightly smaller than 45 degrees with respect to the radial-axial plane and ends just near the split circumferential hydrides, as shown in Figures 4-18(d) to (e). Since the general trends of different types of strain localization for different thickness ratios are exactly the same as those in Chapter 2, their conclusion can also be adopted such that the strain concentration with $\delta \leq 2$ can be assumed to be pronounced in a hydrided irradiated Zr-2.5Nb pressure tube based on the experimental observations of ligament thicknesses and heights of split circumferential hydrides as reported in [21]. It should be noted that for the ligament thickness ratio with $\delta = 3$ in Figures 4-18(d), the strain concentration in the middle of the

ligament is also moderate. As shown in Figures 4-18 to 4-20, the strain distributions in the ligaments are slightly asymmetric for the CCT specimens due to the curvature.

In order to consider the effect of strain concentration on the ductile fracture of ligaments, the same strain-based failure criterion with consideration of stress triaxiality used in Chapters 2 and 3 is considered. For a material element of interest ahead of the crack front, an average stress triaxiality $\overline{\alpha}$ can be determined during the deformation history. The failure effective plastic strain $\overline{\varepsilon}_p^f$ for the material element of interest can then be determined based on the same relationship between the failure effective plastic strain $\overline{\varepsilon}_p^f$ and the average stress triaxiality $\overline{\alpha}$ as shown in Figure 2-24. The histories of the effective plastic strain $\overline{\varepsilon}_p$ at the radial distance of $r = 15$ μm ahead of the crack front at $R = 53.1$ mm of a CCT specimen without hydrides and CCT specimens with hydrides with the heights of 50, 100 and 150 μm and different ligament thicknesses are plotted as functions of the normalized load P / P_0 with P_0 = 3,206 N in Figures 4-21 to 4-23, respectively. The values of the failure effective plastic strain $\overline{\varepsilon}_p^f$ are marked by the crosses with the corresponding colors in the figures. In these figures, the material elements in the middle of ligaments at the radial distance of $r = 15$ μm ahead of the crack front at $R = 53.1$ mm in CCT specimens with split circumferential hydrides with various heights and ligament thicknesses will achieve the failure effective plastic strain $\overline{\varepsilon}_p^f$ earlier than the one without hydrides due to different types of strain concentration as discussed earlier.

Based on the values of the failure effective plastic strain $\overline{\varepsilon}_p^f$ for the cases with $\delta \le 3$ as marked in Figures 4-21 to 4-23, the necessary normalized load for fracture initiation to reach the values of the failure effective plastic strain $\overline{\varepsilon}_p^f$ decreases to 0.60 to 0.70. For the cases with $\delta > 3$, the necessary normalized load for fracture initiation to reach the failure effective plastic

strain $\bar{\varepsilon}_p^f$ is between 0.70 to 1.00, depending on the value of the ligament thickness ratio δ. The necessary normalized loads for fracture initiation of the ligaments with various ligament thickness ratios are very similar to those for CT and PT specimens in Chapters 2 and 3. This means the specimen geometry does not affect the reduction of the normalized loads for fracture initiation of the ligaments between two split circumferential hydrides located near the critical location. It should be mentioned again that the values of the ligament thickness ratio δ are commonly no larger than 3 in a hydrided irradiated Zr-2.5Nb pressure tube as explained in Chapter 2. As shown in Figures 4-21 to 4-23, the computational results can be used to explain the near 35% reduction of the K_C at room temperature obtained from hydrided irradiated CCT specimens when compared with that from unhydrided irradiated ones as observed in [37].

4.4 Conclusions

In this investigation, simulations of curved compact tension (CCT) specimens without and with split circumferential hydrides were conducted using the submodeling technique. For a CCT specimen without hydrides, the computational results first show that the maximum J-integral occurs not in the middle of the crack front but at about one quarter of the thickness from the inner surface. A comparison of the distributions of the J-integrals of compact tension (CT) and CCT specimens without hydrides shows that due to the curvature, the distribution of the J-integral of the CCT specimen is asymmetric. The J-integral is higher in the inner half part and lower in the outer half part when compared to those of the CT specimen. For completeness, the distributions of the stress intensity factor K_I solutions along the crack front in the CT and CCT specimens are also compared. The distributions of the K_I solutions are quite similar to those of the J-integrals with smaller values near the free surfaces. The elastic beam bending theory [9]

indicates that the opening stress ahead of the crack front can increase 6.9% due to the curvature. However, when the crack is introduced, the results of the elastic computational analysis indicate that the maximum increase of K_I along the crack front does not occur on the inner wall as related to the linear distribution of the additional bending stress. The results also show that the maximum percentage of the difference of the maximum K_I is 1.97%. According to the linear elastic fracture mechanics, the applied load to the CCT specimen for fracture initiation is about 1.97% lower than that for a CT specimen based on the same fracture toughness K_C due to the curvature.

The distributions of the opening stress $\sigma_{\Theta\Theta}$ and the out-of-plane normal stress σ_{RR} on the crack plane ahead of the crack front in a CCT specimen are then obtained from the elastic-plastic computational analyses. The distributions show that the largest opening stress $\sigma_{\Theta\Theta}$ and the largest out-of-plane normal stress σ_{RR} occur at the radial distances of about $r = 60$ μm and $r = 50$ μm, respectively, not adjacent to the crack front, and near the middle of the specimen thickness. The magnitudes and locations of the largest opening stress $\sigma_{\Theta\Theta}$ and the largest out-of-plane normal stress σ_{RR} are not affected significantly by the curvature. The opening stress $\sigma_{\Theta\Theta}$ at $r = 60$ μm ranging from $R = 52.5$ mm to $R = 55$ mm is quite close to the theoretical value derived from the slip line theory for rigid perfectly plastic materials under plane strain conditions. This means that the stress state near the middle of the specimen thickness along the crack front is close to that of plane strain conditions under the applied load. With the hydride fracture stress of 750 MPa, the distributions of the opening stress $\sigma_{\Theta\Theta}$ and the out-of-plane normal stress σ_{RR} show that all radial hydrides ahead of the crack front will fracture, and circumferential hydrides ahead of the crack front will split in the middle portion of specimen but

they will not split near the inner and outer surfaces. The sizes of the zones without split circumferential hydrides increase with the increasing radial distance r from the crack front.

With the strain-based failure criterion with consideration of stress triaxiality developed in Chapter 2, the location of the earliest fracture initiation in the thickness direction can be determined to be at $R = 53.1$ mm. Under the same applied load, the CT specimen almost fails (or the CT specimen fails at 100.7% of the applied load) and the CCT specimen fails slightly earlier at 98.7% of the applied load, respectively, based on the same strain-based failure criterion. In Chapter 3, with the same failure criterion, the fracture initiation of a pressure tube (PT) specimen requires additional 3% of the applied internal pressure corresponding to the same K_C used in this investigation. It means that with consideration of the plastic deformation, the fracture initiation load or internal pressure corresponding to the same Kc based on the strain-based failure criterion with consideration of stress triaxiality for CCT specimens without hydrides is 2% lower than that for CT specimens without hydrides and is 4.3% lower than that for PT specimens without hydrides. It should be mentioned that the present strain-based failure criterion with consideration of stress triaxiality can be used to describe the slightly higher fracture toughness for a PT specimen due to different constraint conditions, compared with that for a CCT specimen at room temperature.

For CCT specimens with split circumferential hydrides with various heights and ligament thicknesses near $R = 53.1$ mm, strain concentration is observed in the middle of the ligament when the ratio of the ligament thickness to the hydride height is no larger than 3. With a strain-based failure criterion with consideration of stress triaxiality, the necessary normalized load P / P_0 for fracture initiation is about 0.60 to 0.70 to fracture the ligaments with low plastic work or energy types of strain concentration. The results show that the specimen geometry does not

affect the reduction of the normalized loads for fracture initiation of the ligaments between two split circumferential hydrides located near the critical location, compared with that for CT and PT specimens. With the experimental evidence [21] showing that the values of the ligament thickness ratio are commonly no larger than 3 in a hydrided irradiated Zr-2.5Nb pressure tube, the results suggest that low plastic work or energy types of strain concentration in ligaments are pronounced in a hydrided irradiated Zr-2.5Nb pressure tube. The computational results suggest that only 60% to 70% of the applied load for fracture initiation of an unhydrided irradiated CCT specimen is needed to fracture a hydrided irradiated CCT specimen with many randomly distributed split circumferential hydrides near the crack front. The computational results can be used to explain the near 35% reduction of the K_C at room temperature obtained from hydrided irradiated CCT specimens when compared with that from unhydrided irradiated ones.

Acknowledgement

The support of this work from CANDU Owners Group is greatly appreciated. Helpful discussions with Brian Leitch and Sterling St Lawrence of Canadian Nuclear Laboratories are greatly appreciated.

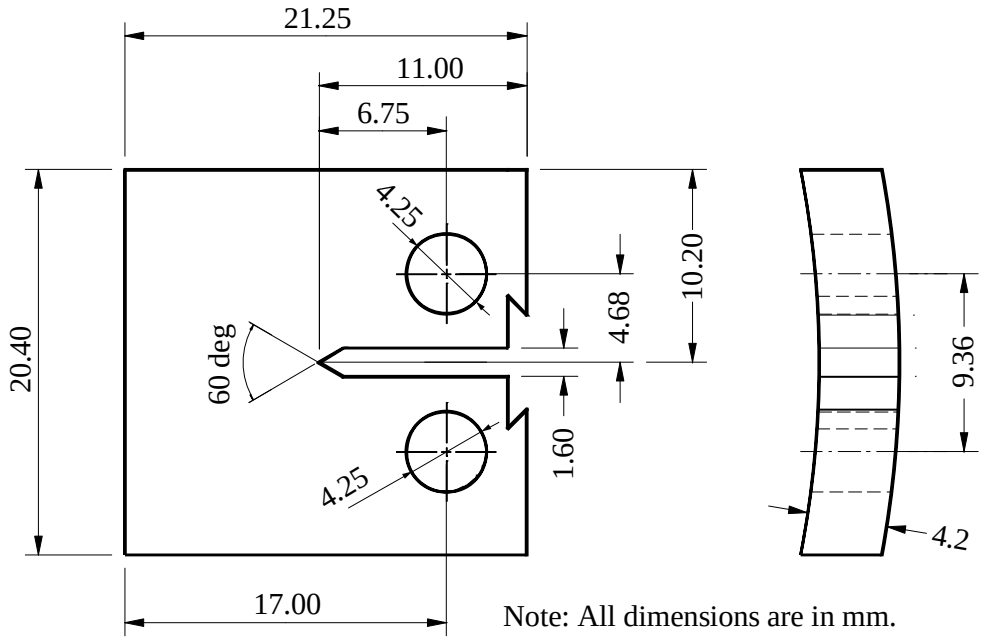

(a)

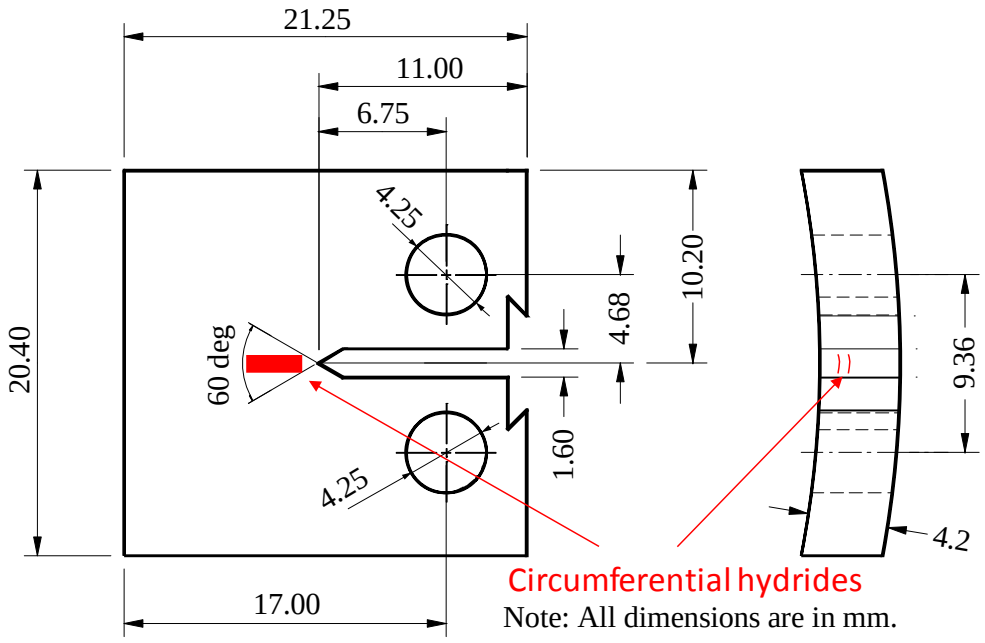

(b)

Figure 4-1. Schematic views of a curved compact tension (CCT) specimen (a) without and (b) with circumferential hydrides. The CCT specimen has a fatigue crack with a length of 2 mm ahead of the notch tip.

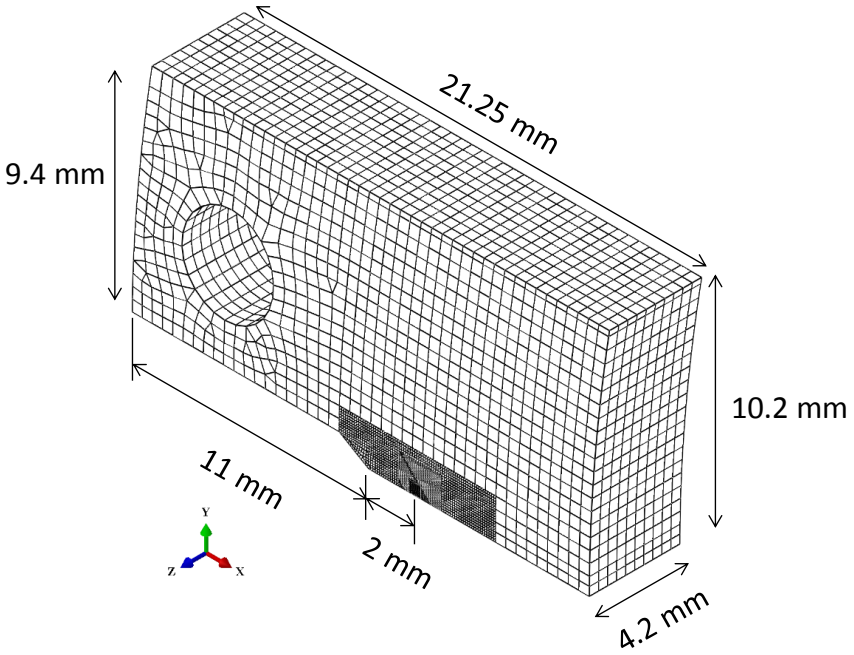

Figure 4-2. The geometry and the mesh of the three-dimensional global finite element model of the upper half of a CCT specimen.

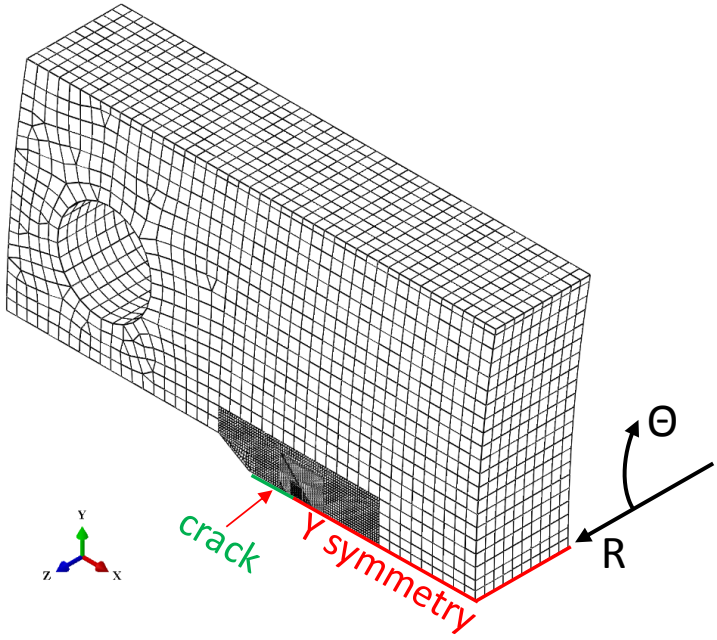

Figure 4-3. The boundary conditions of the three-dimensional global finite element model with the $R-\Theta$ coordinate system defined on the axial cross-sectional plane.

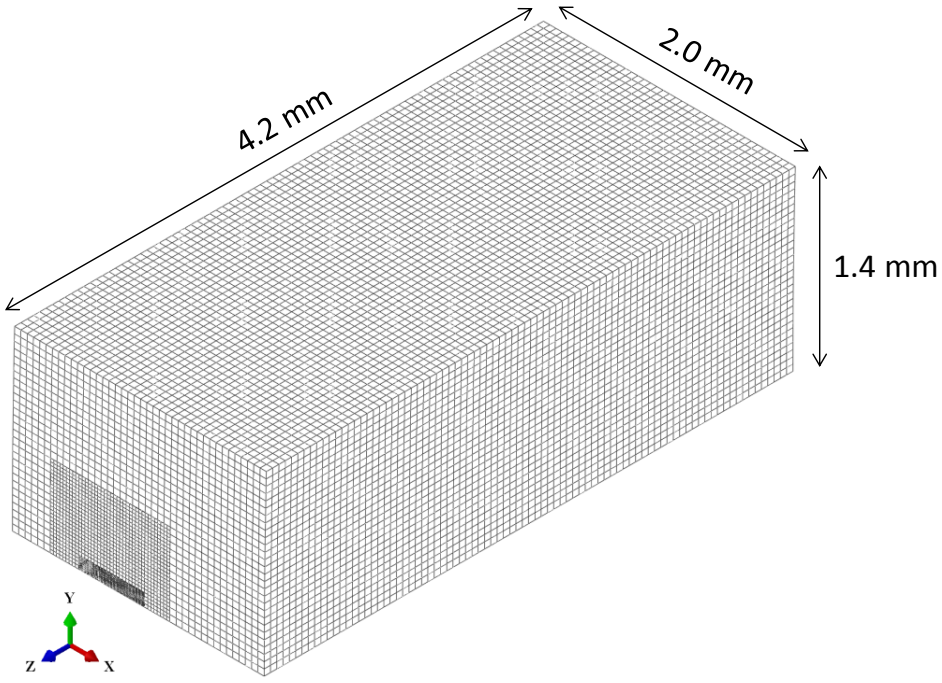

Figure 4-4. The geometry and the mesh of a submodel of the upper half of a CCT specimen.

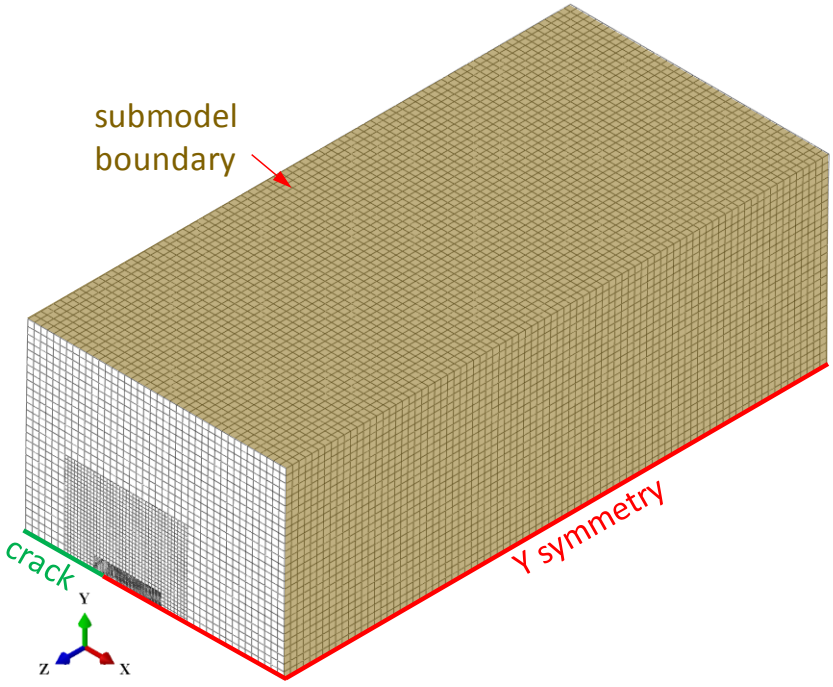

Figure 4-5. The boundary conditions of the three-dimensional submodels.

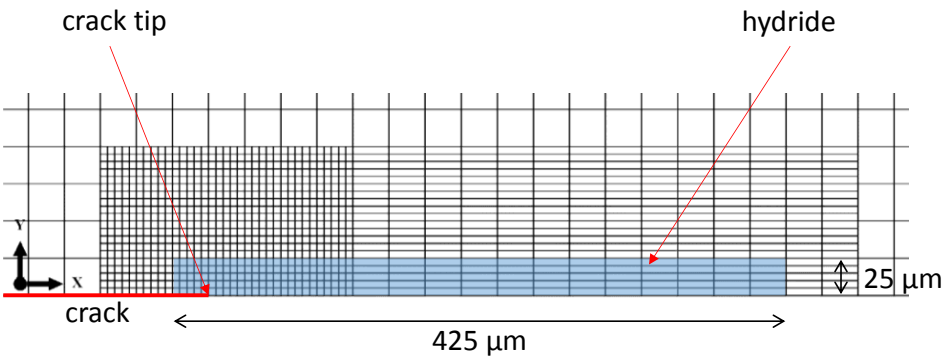

(a)

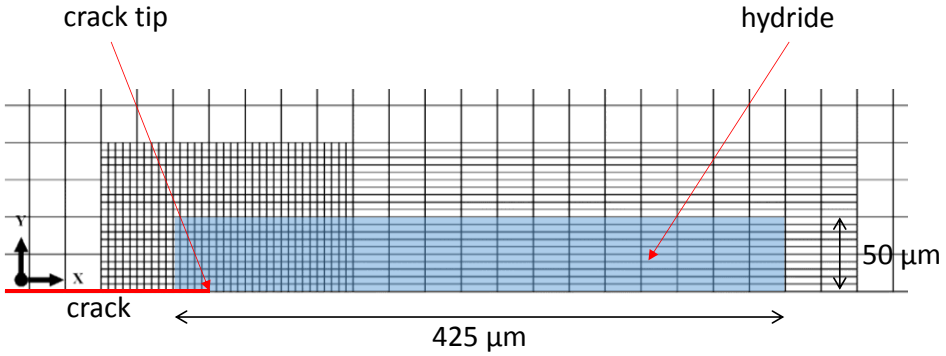

(b)

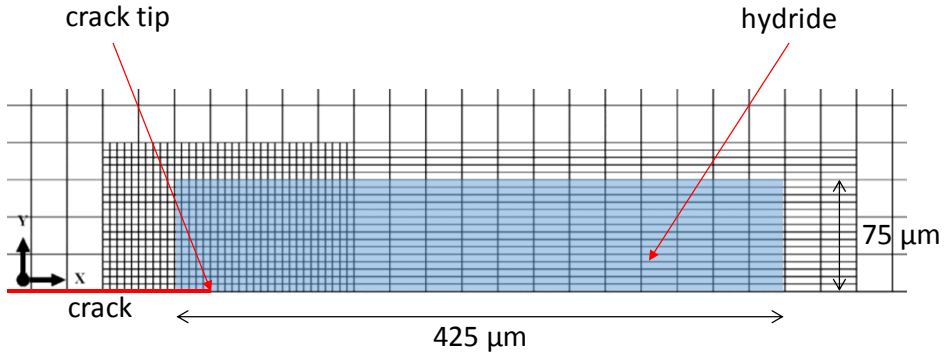

(c)

Figure 4-6. The locations and the sizes of split circumferential hydrides with the heights of (a) 50 µm, (b) 100 µm, and (c) 150 µm on the $X-Y$ plane in the submodels.

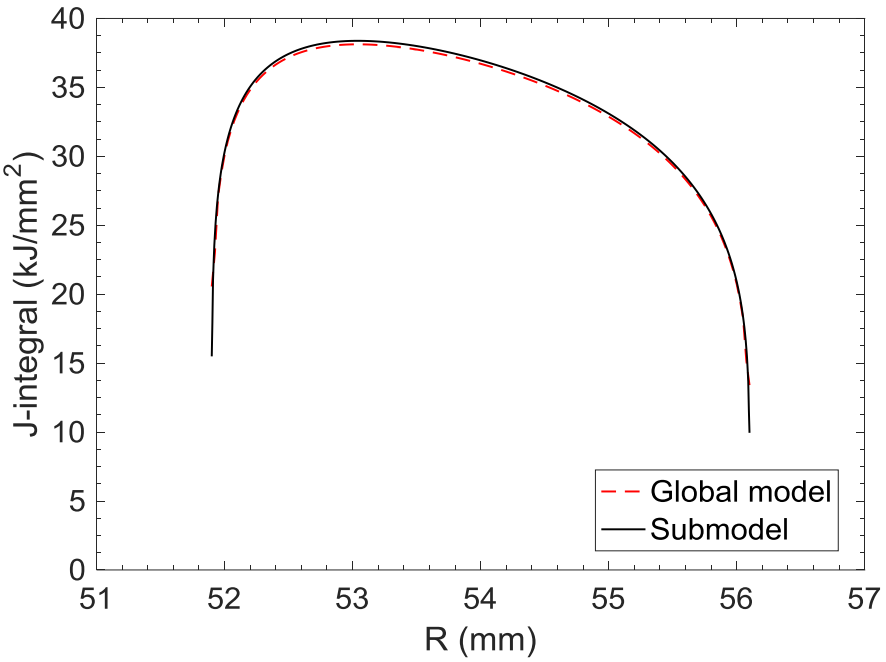

Figure 4-7. The distributions of the computational J-integrals of the global model and the submodel without hydrides.

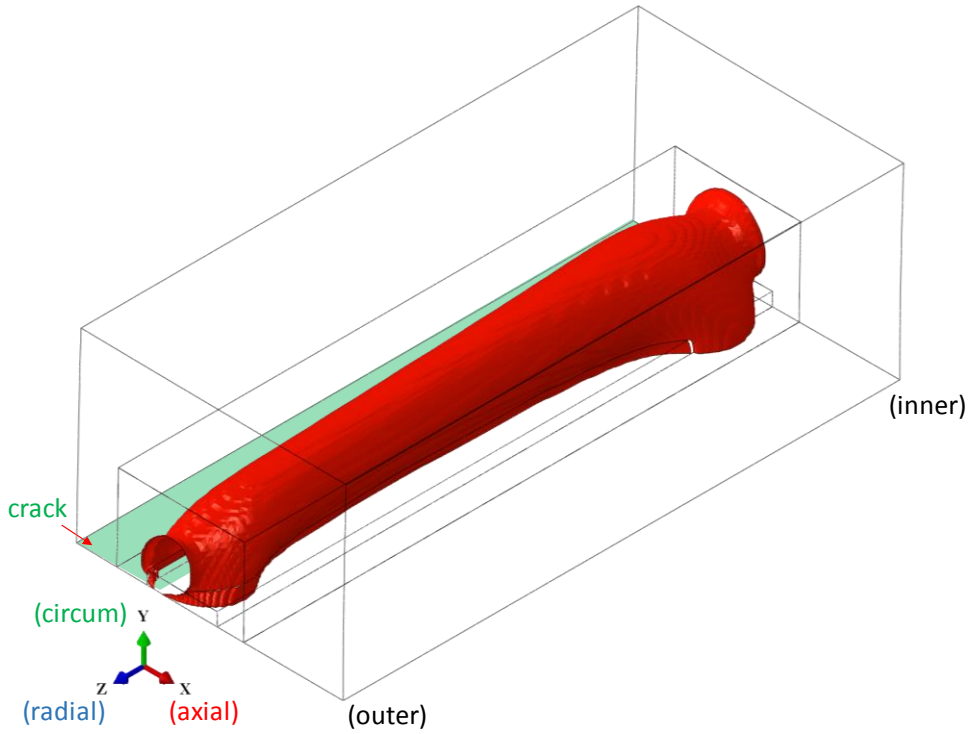

Figure 4-8. The envelope surface of the three-dimensional plastic zone of the submodel without hydrides.

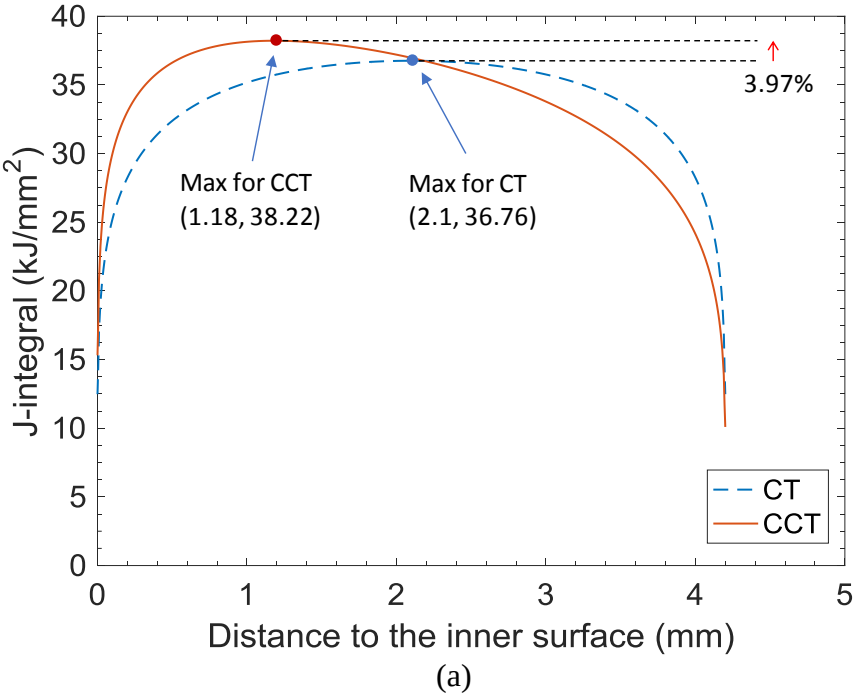

(a)

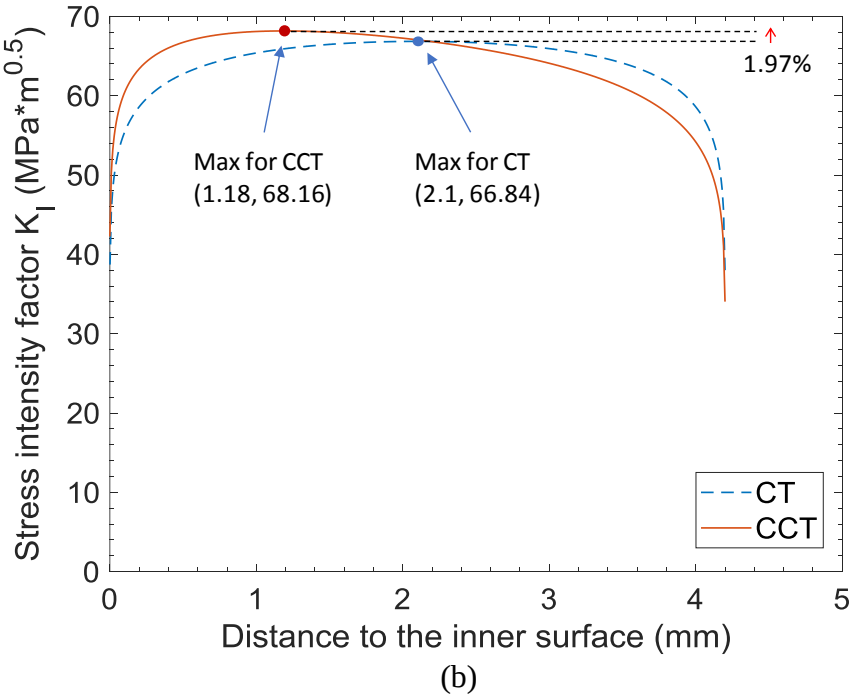

(b)

Figure 4-9. The comparison of the distributions of the computational (a) J-integrals and (b) stress intensity factor K_I solutions of the CT and CCT specimens without hydrides.

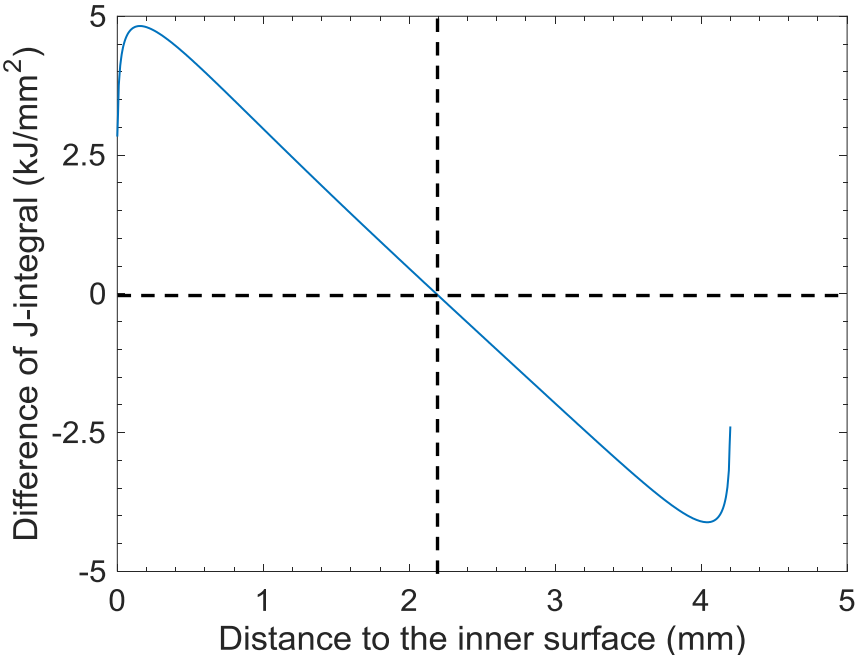

(a)

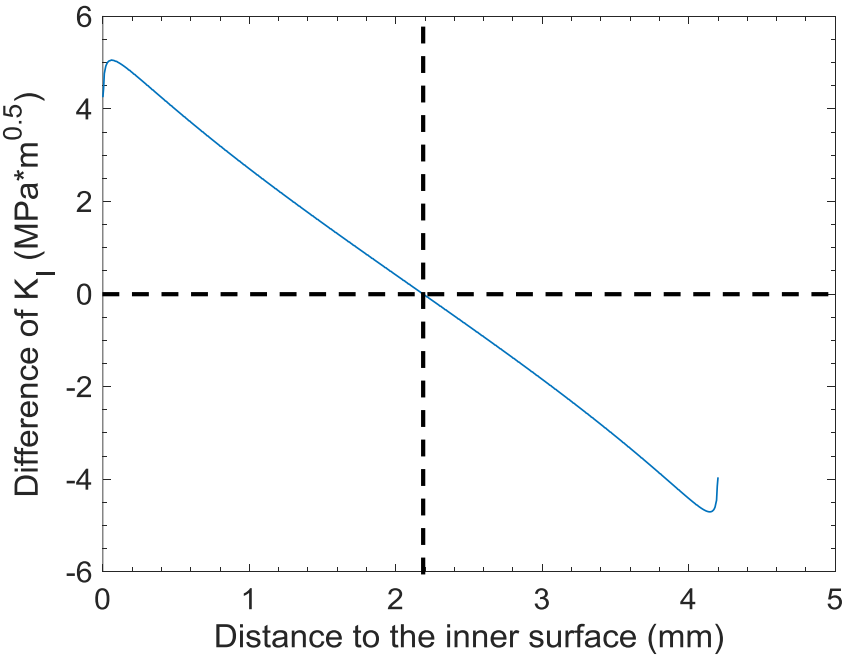

(b)

Figure 4-10. The differences between the computational (a) J-integrals and (b) stress intensity factor K_I solutions of the CCT and CT specimens without hydrides.

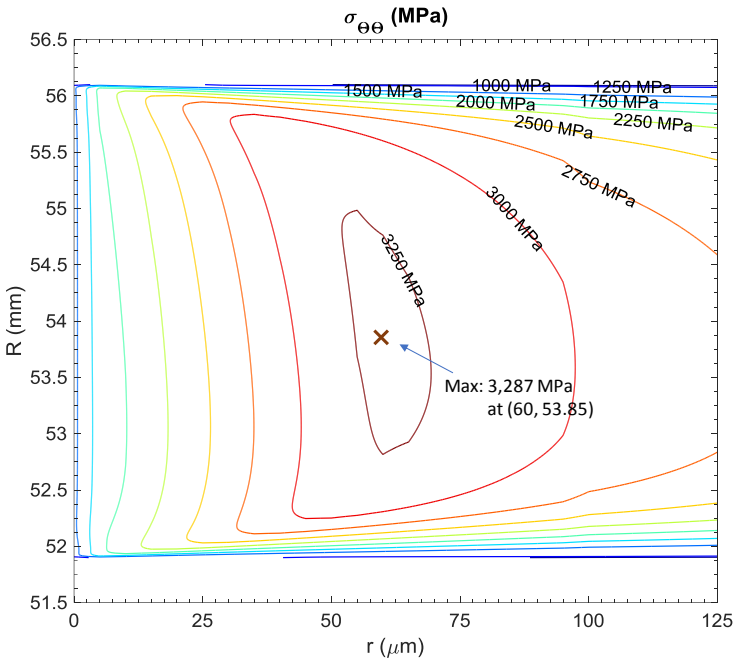

Figure 4-11. The contours of the opening stresses $\sigma_{\Theta\Theta}$ on the crack plane ahead of the crack front. The magnitude and location of the maximum $\sigma_{\Theta\Theta}$ have been marked.

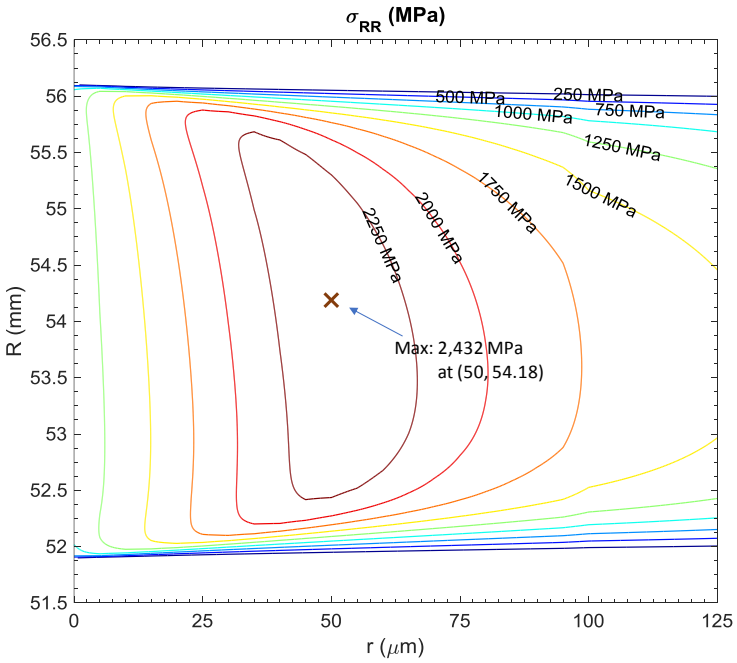

Figure 4-12. The contours of the out-of-plane normal stresses σ_{RR} on the crack plane ahead of the crack front. The magnitude and location of the maximum σ_{RR} have been marked.

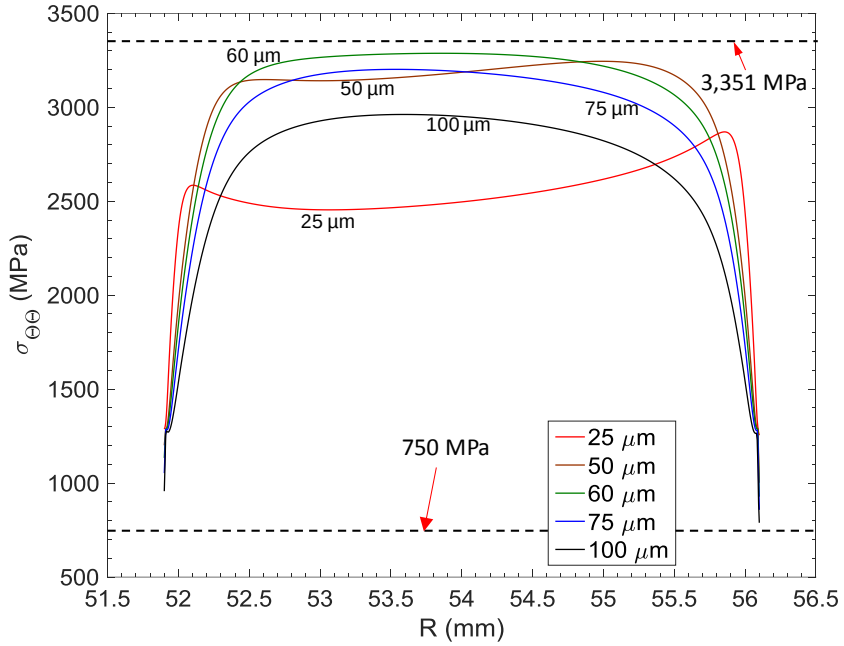

Figure 4-13. The distributions of the opening stresses $\sigma_{\Theta\Theta}$ at different r's in the thickness (R) direction ahead of the crack front.

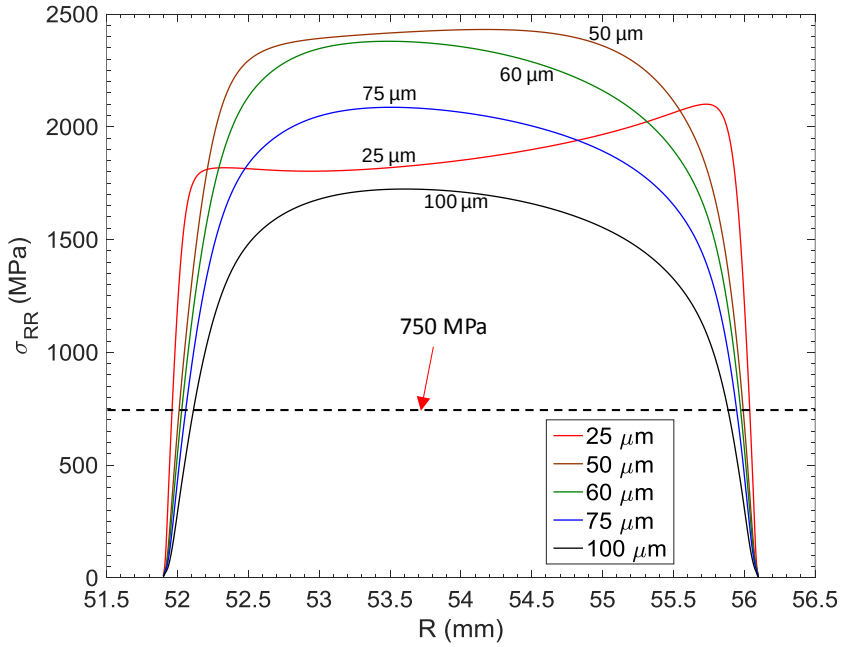

Figure 4-14. The distributions of the out-of-plane normal stresses σ_{RR} at different r's in the thickness (R) direction ahead of the crack front.

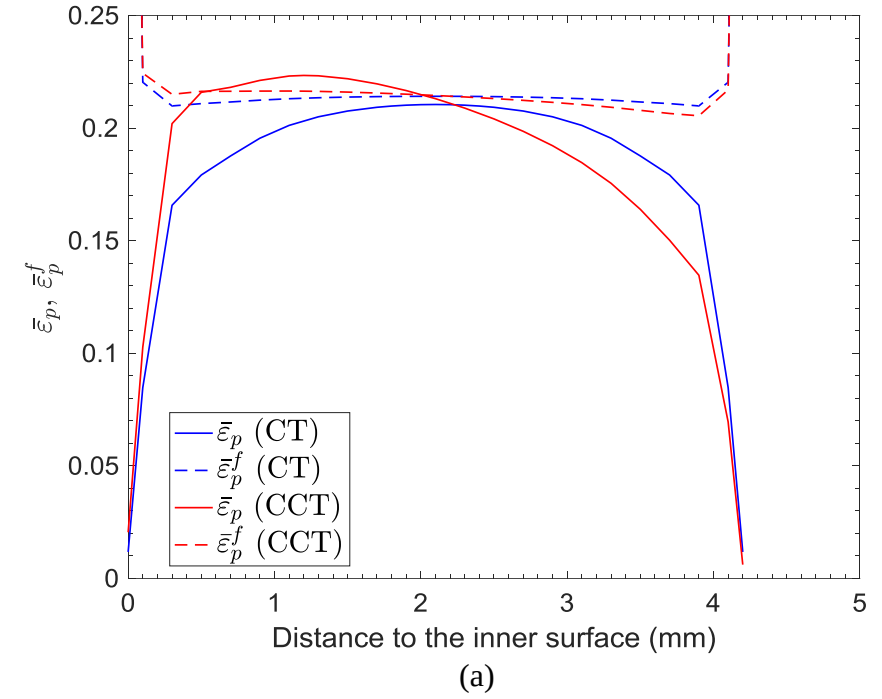

(a)

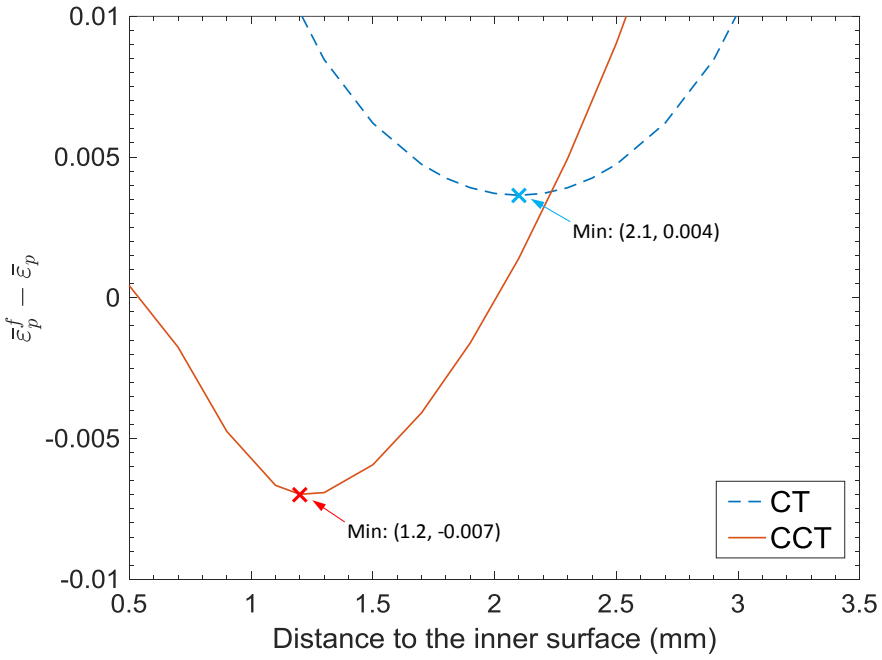

(b)

Figure 4-15. (a) The distributions and (b) the differences of the effective plastic strain $\bar{\varepsilon}_p$ and the failure effective plastic strain $\bar{\varepsilon}_p^f$ in the thickness (R) direction at the radial distance of $r = 15$ μm ahead of the crack front in CT and CCT specimens without hydrides under the applied load P_0.

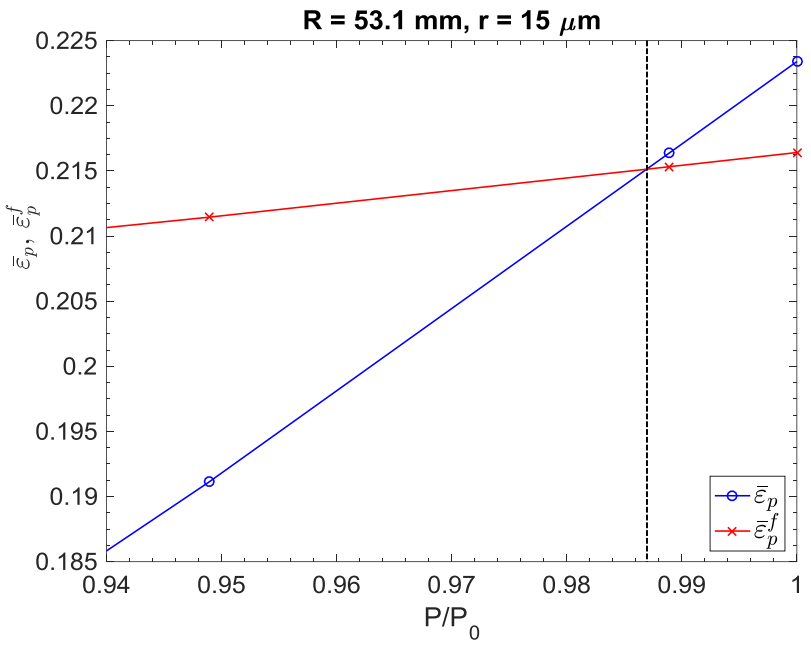

Figure 4-16. The histories of the effective plastic strain $\bar{\varepsilon}_p$ and the failure effective plastic strain $\bar{\varepsilon}_p^f$ at the radial distance of $r = 15$ μm and $R = 53.1$ mm near the end of the application of the normalized load P/P_0 for a CCT specimen without hydrides.

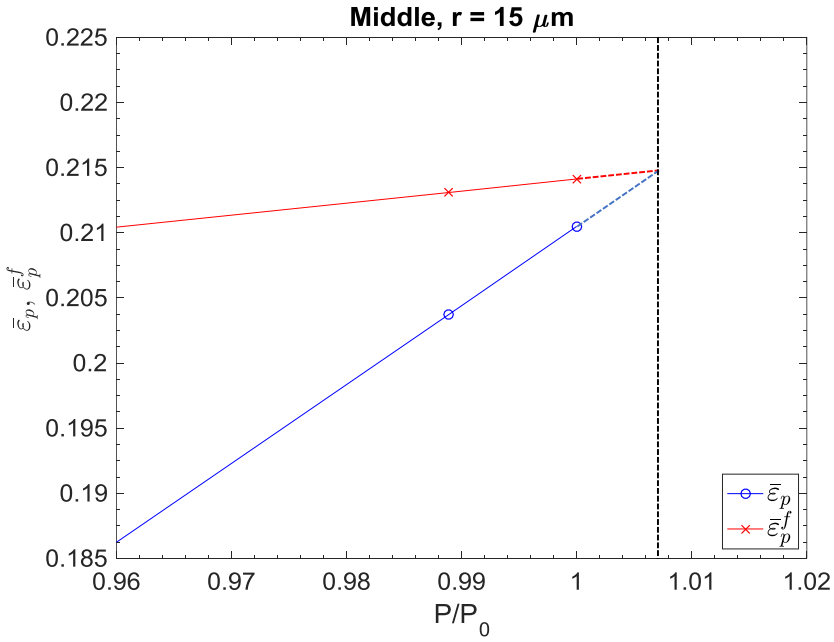

Figure 4-17. The histories of the effective plastic strain $\bar{\varepsilon}_p$ and the failure effective plastic strain $\bar{\varepsilon}_p^f$ at the radial distance of $r = 15$ μm and the middle of thickness near the end of the application of the normalized load P/P_0 for a CT specimen without hydrides.

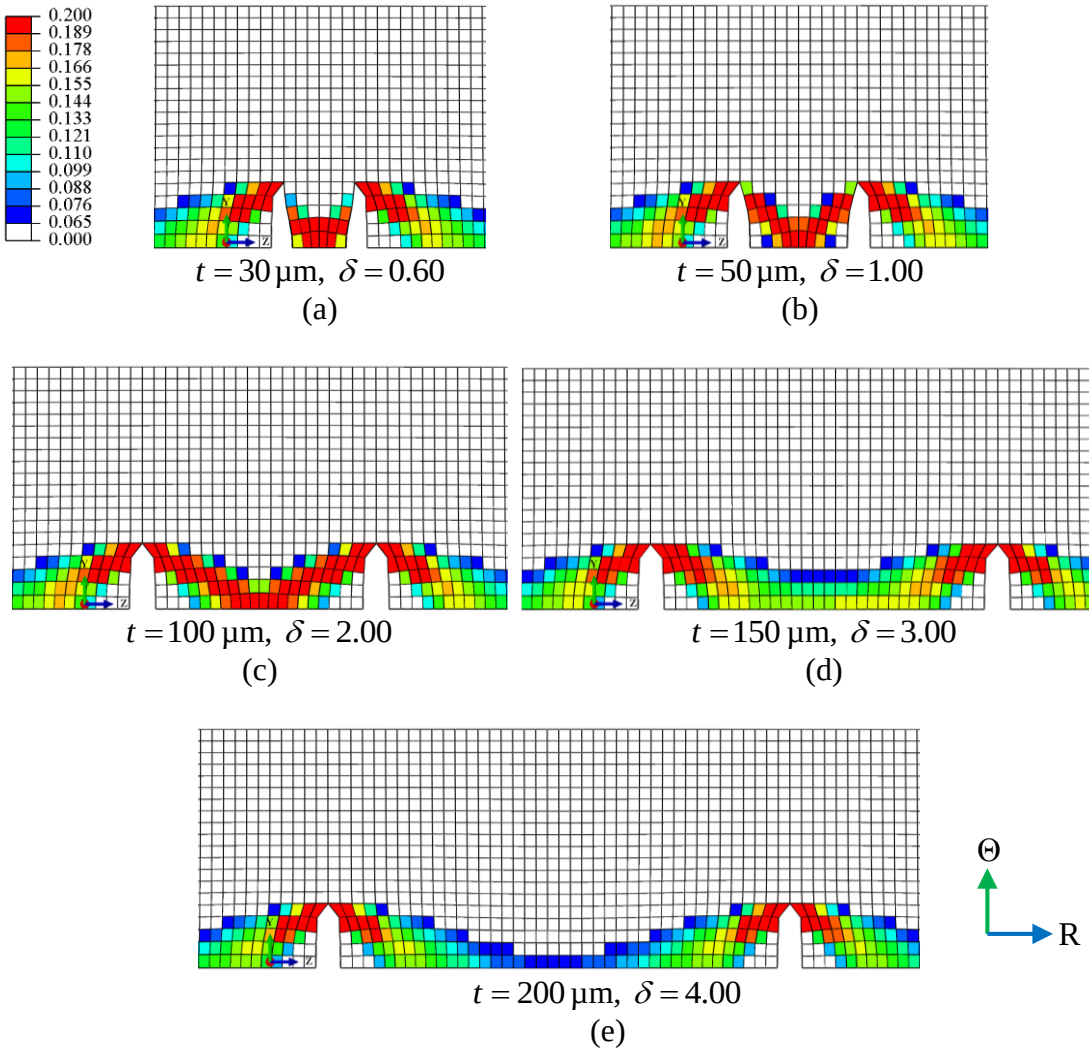

Figure 4-18. The deformed meshes with the magnitudes of the effective plastic strain $\bar{\varepsilon}_p$ for the finite elements marked in colors for the radial-circumferential plane near $R = 53.1$ mm at the radial distance $r = 15$ μm ahead of the crack front for the CCT specimens with hydrides with the height of 50 μm under 60 percent of the applied load of 3,206 N. The ligament thicknesses are (a) 30 μm, (b) 50 μm, (c) 100 μm, (d) 150 μm, and (e) 200 μm.

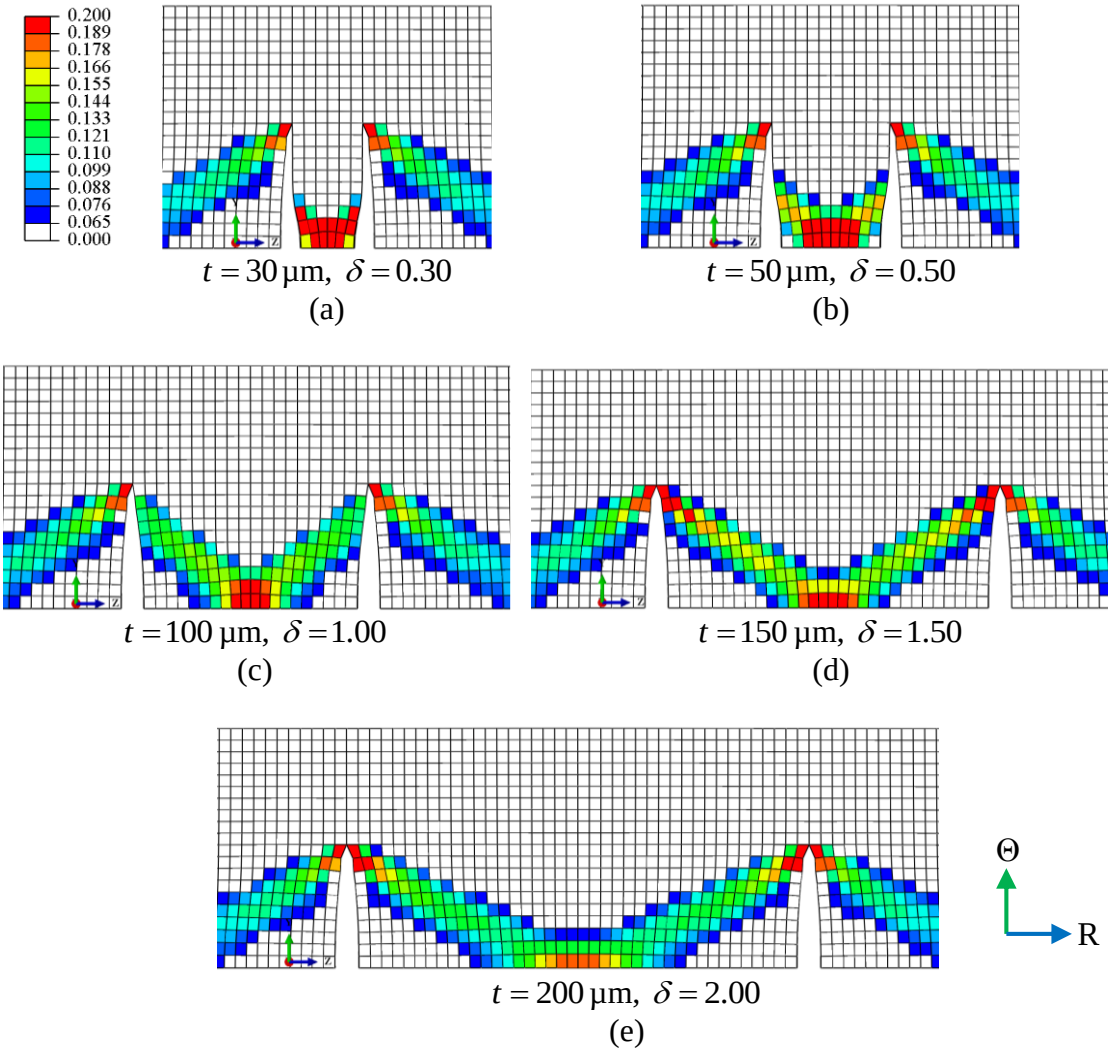

Figure 4-19. The deformed meshes with the magnitudes of the effective plastic strain $\bar{\varepsilon}_p$ for the finite elements marked in colors for the radial-circumferential plane near $R = 53.1$ mm at the radial distance $r = 15$ µm ahead of the crack front for the CCT specimens with hydrides with the height of 100 µm under 60 percent of the applied load of 3,206 N. The ligament thicknesses are (a) 30 µm, (b) 50 µm, (c) 100 µm, (d) 150 µm, and (e) 200 µm.

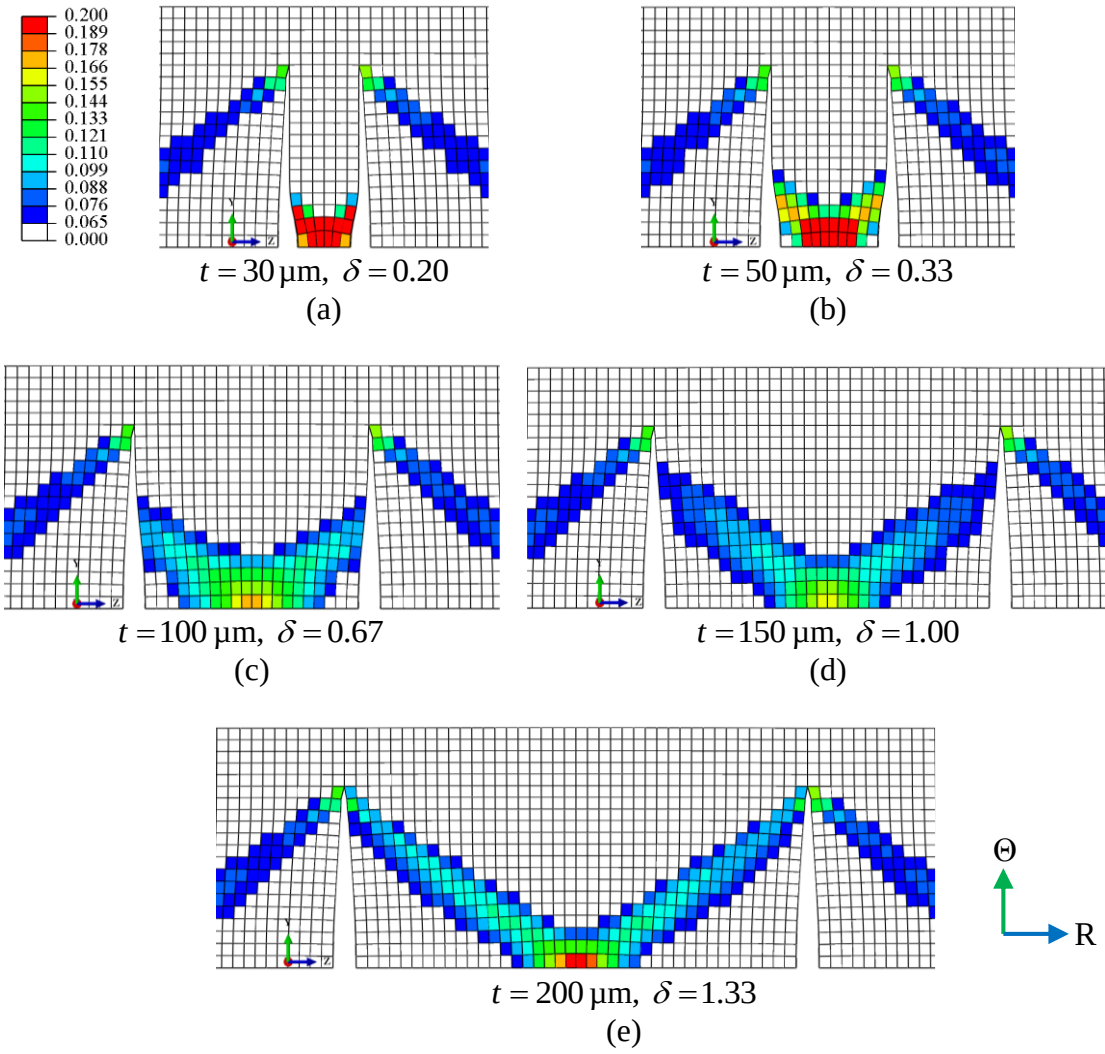

Figure 4-20. The deformed meshes with the magnitudes of the effective plastic strain $\bar{\varepsilon}_p$ for the finite elements marked in colors for the radial-circumferential plane near $R = 53.1$ mm at the radial distance $r = 15$ µm ahead of the crack front for the CCT specimens with hydrides with the height of 150 µm under 60 percent of the applied load of 3,206 N. The ligament thicknesses are (a) 30 µm, (b) 50 µm, (c) 100 µm, (d) 150 µm, and (e) 200 µm.

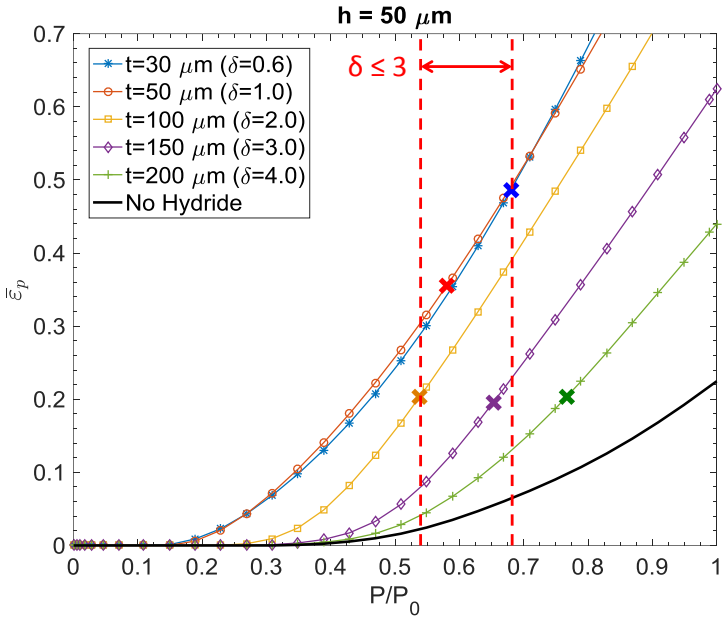

Figure 4-21. The histories of the effective plastic strain $\bar{\varepsilon}_p$ at the radial distance of $r = 15$ μm plotted as functions of the normalized load P/P_0 for a CCT specimen without hydrides and CCT specimens with split circumferential hydrides with the height of 50 μm and different ligament thicknesses.

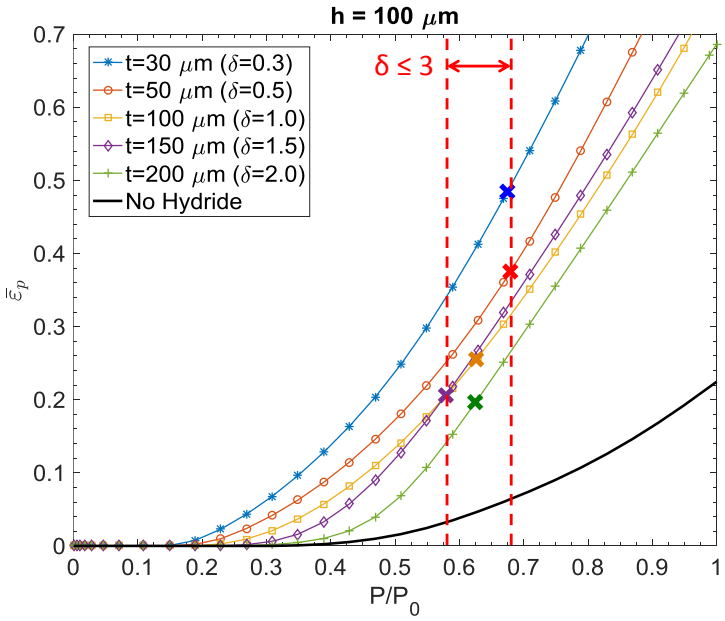

Figure 4-22. The histories of the effective plastic strain $\bar{\varepsilon}_p$ at the radial distance of $r = 15$ μm plotted as functions of the normalized load P/P_0 for a CCT specimen without hydrides and CCT specimens with split circumferential hydrides with the height of 100 μm and different ligament thicknesses.

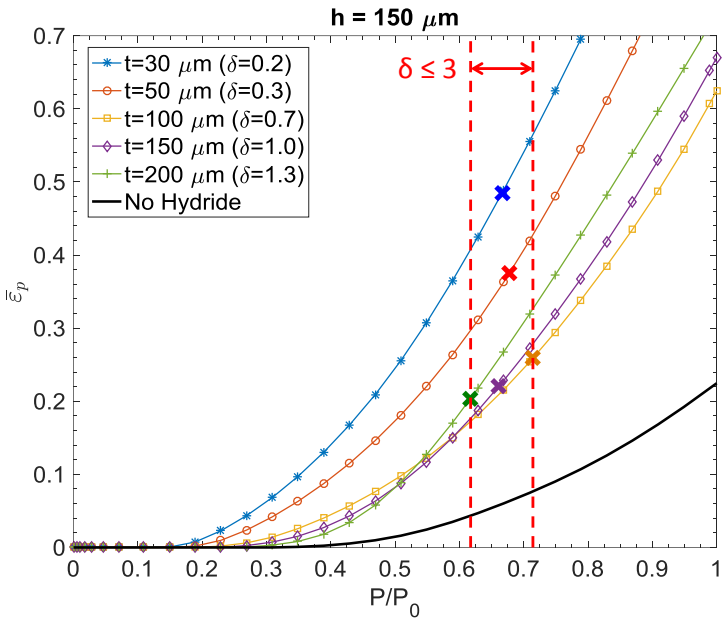

Figure 4-23. The histories of the effective plastic strain $\bar{\varepsilon}_p$ at the radial distance of $r = 15$ μm plotted as functions of the normalized load P/P_0 for a CCT specimen without hydrides and CCT specimens with split circumferential hydrides with the height of 150 μm and different ligament thicknesses.

Chapter 5 Conclusions

In this investigation, simulations of compact tension (CT), pressure tube (PT) and curved compact tension (CCT) specimens without and with split circumferential hydrides were conducted using the submodeling technique in Chapters 2, 3 and 4, respectively. The choices of the mesh sizes and geometric sizes of the global model and the submodels follow the guidelines established in [39].

5.1 Specimens without Split Circumferential Hydrides

In Chapter 2, for a CT specimen without split circumferential hydrides, the distributions of the opening stress σ_{yy} and the out-of-plane normal stress σ_{zz} on the half crack plane ahead of the crack front are presented. The computational results show that in the middle of the specimen, the largest opening stress σ_{yy} and the largest out-of-plane normal stress σ_{zz} occur at the radial distances of about $r = 60$ μm and $r = 50$ μm, respectively, not adjacent to the crack front at fracture initiation. The largest opening stress σ_{yy} is quite close to the theoretical value derived from the slip-line theory for rigid perfectly plastic materials under plane strain conditions. This means that the stress state near the middle portion of the crack front is close to that of the plane strain conditions at fracture initiation. With the hydride fracture stress of 750 MPa, the distributions of the opening stress σ_{yy} and the out-of-plane normal stress σ_{zz} show that all radial hydrides ahead of the crack front will fracture, and circumferential hydrides ahead of the crack front split in the middle portion of specimen but they do not split near the free surface. The size

of the zone without split circumferential hydrides increases with the increasing radial distance r from the crack front. A strain-based failure criterion with consideration of stress triaxiality is developed using the Gurson yield model with two fitting parameters of the initial void volume fraction f_0 and the failure void volume fraction f_f. The two fitting parameters are determined by the failure engineering plastic strain of the transverse tensile tests and the failure effective plastic strain for the material element at $r = 15$ μm ahead of the crack front in the CT specimen without hydride at K_C. The location of the earliest fracture initiation in the thickness direction can be determined to be in the middle of the thickness.

In Chapter 3, for a PT specimen without split circumferential hydrides, the computational results first show that the maximum J-integral occurs not in the middle of the crack front but at about one quarter of the tube thickness from the outer tube surface. The distributions of the opening stress $\sigma_{\Theta\Theta}$ and the out-of-plane normal stress σ_{RR} on the crack plane ahead of the crack front are then obtained. The distributions show that the largest opening stress $\sigma_{\Theta\Theta}$ and the largest out-of-plane normal stress σ_{RR} occur at the radial distances of about $r = 55$ μm and $r = 50$ μm, respectively, not adjacent to the crack front, at about one quarter of the tube thickness from the inner tube surface at fracture initiation. The largest opening stress $\sigma_{\Theta\Theta}$ is quite close to the theoretical value derived from the slip-line theory for rigid perfectly plastic materials under plane strain conditions. This means that the stress state near about one quarter thickness from the inner surface along the crack front is close to that of plane strain conditions at fracture initiation. With the hydride fracture stress of 750 MPa, the distributions of the opening stress $\sigma_{\Theta\Theta}$ and the out-of-plane normal stress σ_{RR} show that all radial hydrides ahead of the crack front will fracture, and circumferential hydrides ahead of the crack front split in the middle portion of specimen but they do not split near the inner and outer surfaces. The sizes of the

zones without split circumferential hydrides increase with the increasing radial distance r from the crack front. With the same strain-based failure criterion with consideration of stress triaxiality, the location of the earliest fracture initiation in the thickness direction can be determined to be at $R = 53.7$ mm near the middle of the crack front. Under the same K_C, the CT specimen fails and the PT specimen almost fails (requires additional 3% of the applied internal pressure), respectively, based on the same failure criterion.

In Chapter 4, for a CCT specimen without hydrides, the computational results first show that the maximum J-integral occurs not in the middle of the crack front but at about one quarter of the thickness from the inner surface. A comparison of the distributions of the J-integrals of CT and CCT specimens without hydrides shows that the J-integral is higher in the inner half part and lower in the outer half part when compared to those of the CT specimen. For completeness, the distributions of the stress intensity factor K_I solutions along the crack front in the CT and CCT specimens are also compared. The distributions of the K_I solutions are quite similar to those of the J-integrals with smaller values near the free surfaces. The elastic beam bending theory [9] indicates that the opening stress ahead of the crack front can increase 6.9% due to the curvature. However, when the crack is introduced, the results of the elastic computational analysis indicate that the maximum increase of K_I along the crack front does not occur on the inner wall as related to the linear distribution of the additional bending stress. The results also show that the maximum percentage of the difference of the maximum K_I is 1.97%. According to the linear elastic fracture mechanics, the applied load to the CCT specimen for fracture initiation is about 1.97% lower than that for a CT specimen based on the same fracture toughness K_C due to the curvature.

The distributions of the opening stress $\sigma_{\Theta\Theta}$ and the out-of-plane normal stress σ_{RR} on the crack plane ahead of the crack front in a CCT specimen are then obtained from the elastic-plastic computational analyses. The distributions show that the largest opening stress $\sigma_{\Theta\Theta}$ and the largest out-of-plane normal stress σ_{RR} occur at the radial distances of about $r = 60$ μm and $r = 50$ μm, respectively, not adjacent to the crack front, and near the middle of the specimen thickness. The magnitudes and locations of the largest opening stress $\sigma_{\Theta\Theta}$ and the largest out-of-plane normal stress σ_{RR} are not affected significantly by the curvature. The opening stress $\sigma_{\Theta\Theta}$ at $r = 60$ μm ranging from $R = 52.5$ mm to $R = 55$ mm is quite close to the theoretical value derived from the slip-line theory for rigid perfectly plastic materials under plane strain conditions. This means that the stress state near the middle of the specimen thickness along the crack front is close to that of plane strain conditions at fracture initiation. With the hydride fracture stress of 750 MPa, the distributions of the opening stress $\sigma_{\Theta\Theta}$ and the out-of-plane normal stress σ_{RR} show that all radial hydrides ahead of the crack front will fracture, and circumferential hydrides ahead of the crack front will split in the middle portion of specimen but they will not split near the inner and outer surfaces. The sizes of the zones without split circumferential hydrides increase with the increasing radial distance r from the crack front.

With the same strain-based failure criterion with consideration of stress triaxiality, the location of the earliest fracture initiation in the thickness direction can be determined to be at $R = 53.1$ mm. Under the same applied load, the CT specimen almost fails (or the CT specimen fails at 100.7% of the applied load) and the CCT specimen fails slightly earlier at 98.7% of the applied load, respectively, based on the same strain-based failure criterion. In Chapter 3, with the same failure criterion, the fracture initiation of a pressure tube (PT) specimen requires

additional 3% of the applied internal pressure corresponding to the same K_C used in this investigation. It means that with consideration of the plastic deformation, the fracture initiation load or internal pressure corresponding to the same Kc based on the strain-based failure criterion with consideration of stress triaxiality for CCT specimens without hydrides is 2% lower than that for CT specimens without hydrides and is 4.3% lower than that for PT specimens without hydrides. It should be mentioned that the present strain-based failure criterion with consideration of stress triaxiality can be used to describe the slightly higher fracture toughness for a PT specimen due to different constraint conditions and different types of loading, compared with that for a CCT specimen at room temperature.

5.2 Specimens with Split Circumferential Hydrides

For CT, PT and CCT specimens with split circumferential hydrides with various heights and ligament thicknesses near the critical location, strain concentration is observed in the middle of the ligament when the ratio of the ligament thickness to the hydride height is no larger than 3. With the strain-based failure criterion with consideration of stress triaxiality, the necessary normalized load P/P_0 or p/p_0 for fracture initiation is about 0.60 to 0.70 to fracture the ligaments with low plastic work or energy types of strain concentration. The results show that the specimen geometry does not affect the reduction of the normalized loads for fracture initiation of the ligaments between two split circumferential hydrides located near the critical locations. With the experimental evidence [21] showing that the values of the ligament thickness ratio are commonly no larger than 3 in a hydrided irradiated Zr-2.5Nb pressure tube, the results suggest that low plastic work or energy types of strain concentration in ligaments are pronounced in a hydrided irradiated Zr-2.5Nb pressure tube. The computational results suggest that only

60% to 70% of the applied load or internal pressure for fracture initiation of an unhydrided irradiated CT, PT or CCT specimen is needed to fracture a hydrided irradiated CT, PT or CCT specimen with many randomly distributed split circumferential hydrides near the crack front. The computational results can be used to explain the near 35% reduction of the experimental K_C's at room temperature obtained from hydrided irradiated PT and CCT specimens when compared with those from unhydrided irradiated ones.

Appendices

Appendix A. Transverse Tensile Behavior of Zr-2.5Nb Material

The stress-strain relation of the irradiated Zr-2.5Nb materials at room temperature in this investigation is obtained from transverse tensile tests. Figure A-1 shows a schematic of a transverse tensile specimen machined from an as-received pressure tube [38]. As shown in the figure, the specimen has a gauge length of 10 mm, a width of 4 mm, and a thickness of 2 mm. Due to symmetry, only one eighth of the gauge section of the transverse tensile specimen is modeled and the finite element model has the size of 5 mm by 2 mm by 1 mm. Figure A-2 shows the three-dimensional finite element model with the smallest element size of 0.1 mm by 0.05 mm by 0.1 mm near the center of the model. The three-dimensional linear element with reduced integration (C3D8R) was used for the analysis in ABAQUS. A uniform displacement was applied to the top surface of the finite element model. The left back, bottom, and right back surfaces represent the X, Y, and Z symmetry planes, respectively. The right and left front surfaces represent the free surfaces. A reduced width in the X direction for the bottom area with the size of 1.99 mm by 1 mm is used to trigger the necking behavior in the X and Z directions in the middle of the tensile specimen. Finite element analyses were also conducted with the reduced bottom surface of the size of 1.995 mm by 1 mm. The computational results are quite the same and, therefore, only the results based on the reduced bottom area of 1.99 mm by 1 mm are reported in this study.

The Young's modulus of 102.122 GPa and Poisson's ratio of 0.4, as provided in [27] for irradiated Zr-2.5Nb materials, are used in this study. Figure A-3 shows the input true stress-plastic strain curve for the irradiated Zr-2.5Nb material at room temperature. The input curve was derived by fitting the nominal stress-plastic strain curve to the experimental data up to a stress corresponding to the tensile strength and then assuming a perfectly plastic behavior for the plastic strain values larger than the plastic strain at the tensile strength, as in Amodeo et al. [3]. The curve does not exactly represent an elastic perfectly plastic material. But at large plastic strains, a perfectly plastic behavior is assumed.

Figure A-4 shows a comparison of the nominal stress-plastic strain curves from the experiments [38] and the finite element analysis for the irradiated Zr-2.5Nb material at room temperature. As shown in the figure, the results of the finite element analysis perfectly fit the experimental data. Figure A-5 shows the necking in the thickness direction (Z direction) and in the width direction (X direction) for the one-eighth tensile specimen at room temperature. The good fit suggests that the softening behavior of the tensile specimen from the nominal stress-plastic strain curve is mostly due to necking, not material softening. It also suggests that an elastic perfectly plastic material behavior can be used to represent the elastic plastic behavior of the irradiated Zr-2.5Nb material at large plastic strains.

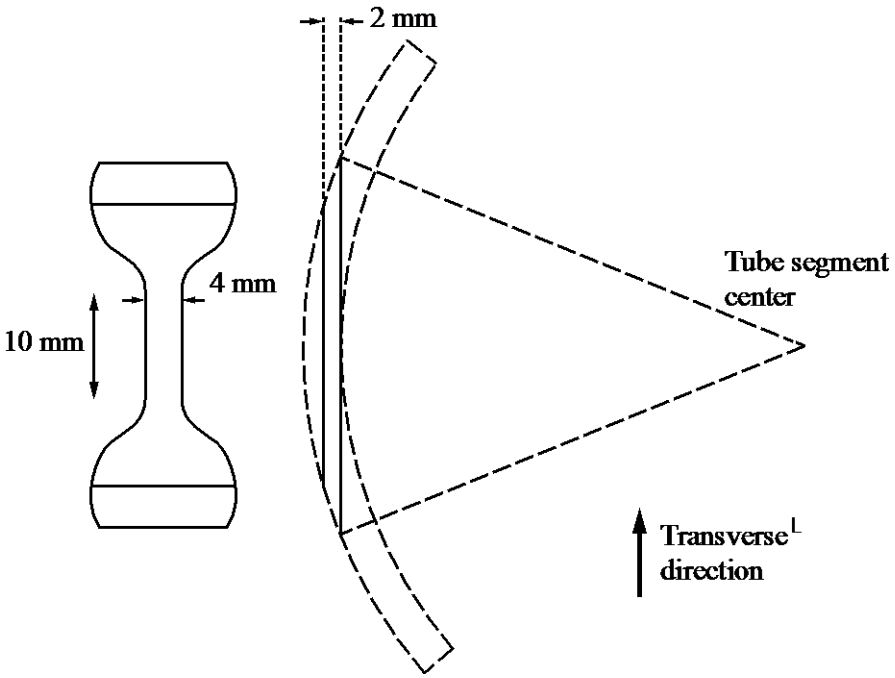

Figure A-1. A schematic of a transverse tensile specimen machined from an as-received pressure tube

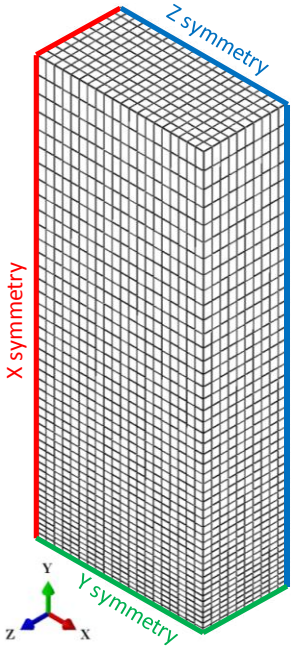

Figure A-2. A three-dimensional finite element model of one eighth of the gauge section of a transverse tensile specimen

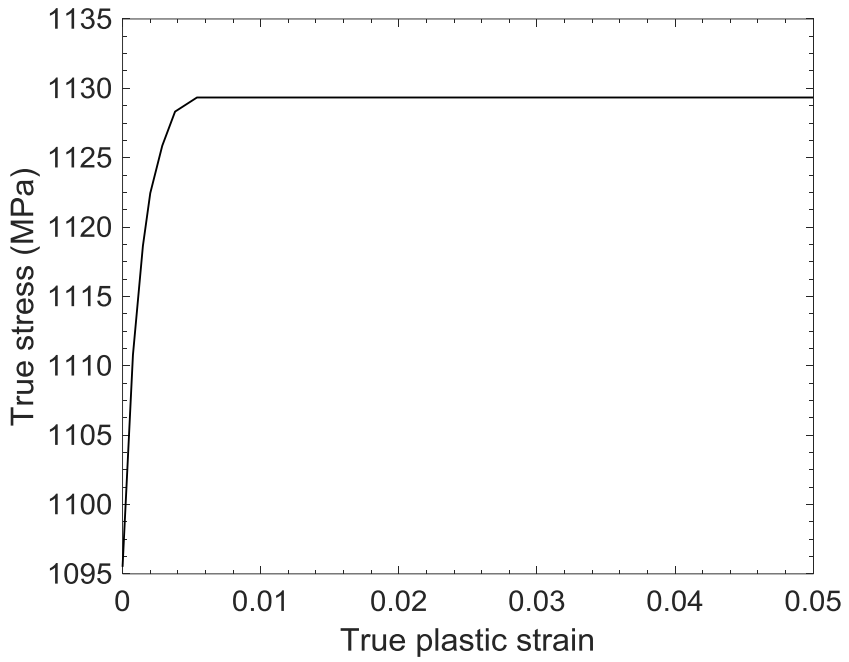

Figure A-3. The input true stress-plastic strain curve for the irradiated Zr-2.5Nb material at room temperature

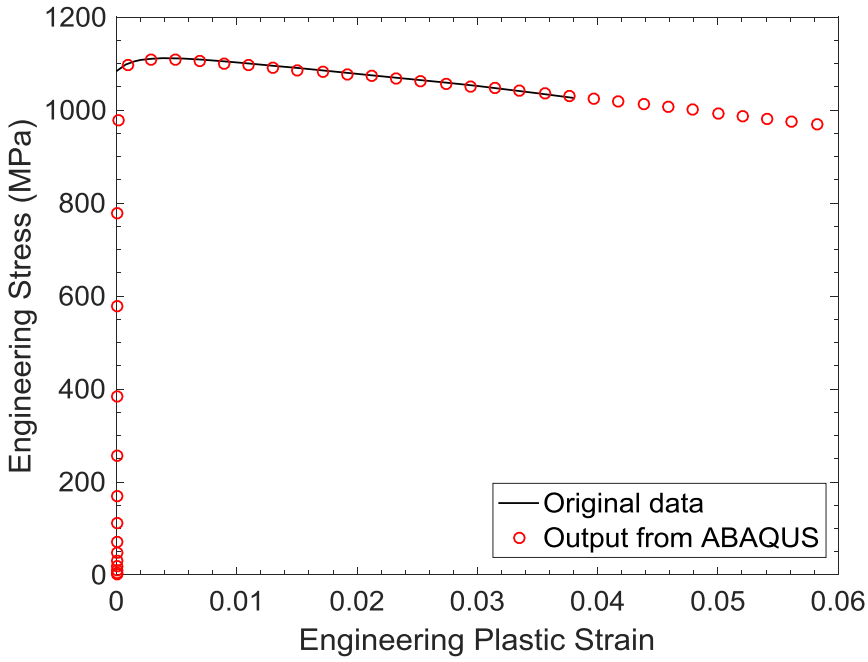

Figure A-4. A comparison of the nominal stress-plastic strain curves from the experiment and the finite element analysis for the irradiated Zr-2.5Nb material at room temperature

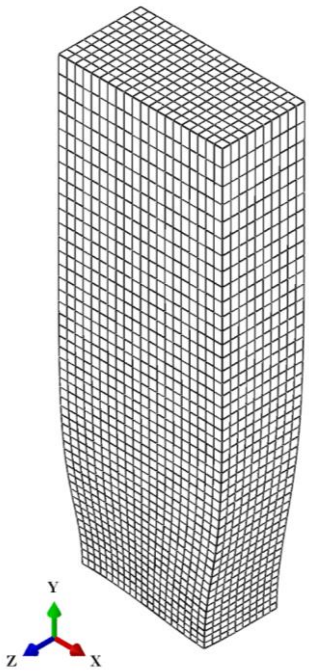

Figure A-5. Necking for the one-eighth tensile specimen at room temperature

Appendix B. Stress Triaxiality ahead of Crack Front

In this appendix, we examine systematically the states of the stress triaxiality α ahead of the crack front for a CT specimen without hydride and a CT specimen with hydrides. Figure B-1(a) shows the states of the stress triaxiality α for the material elements ahead of the crack front up to 50 μm on the mid-planes of the CT specimen without hydride and with hydrides with the height of 50 μm and different ligament thicknesses at $P/P_0 = 0.63$. As shown in the figure, the stress triaxiality α increases and then decreases as the radial distance r decreases for the CT specimen without hydride, whereas the stress triaxiality α increases as the radial distance r decreases for the CT specimen with hydrides with the ligament thicknesses of 30 and 50 μm. For the CT specimens with hydrides with larger ligament thicknesses, as the ligament thickness increases, the distribution of the stress triaxiality α as a function of the radial distance r approaches to that for the CT specimen without hydride. Figure B-1(b) shows the states of the stress triaxiality α for the material elements ahead of the crack front up to 50 μm on the mid-plane of the CT specimen without hydride at $P/P_0 = 0.63$ and $P/P_0 = 1.00$. As shown in the figure, the distributions of the states of the stress triaxiality α ahead of the crack front varies with the normalized load P/P_0 and the peak of the distribution moves away from the crack front (not shown due to the range of the radial distance shown in this figure) when P/P_0 increases.

Figures B-2(a) and (b) shows the distributions of the effective plastic strain $\bar{\varepsilon}_p$ as functions of the radial distance r ahead of the crack front for the cases as discussed above. As shown in Figure B-2(a), the effective plastic strains $\bar{\varepsilon}_p$ increases significantly for the CT

specimen without hydrides as the radial distance r decreases, whereas the values of the effective plastic strain $\bar{\varepsilon}_p$ are very large in the range of the radial distance r from 0 to 20 μm (0.02 mm) for the CT specimens with hydrides with the ligament thicknesses of 30 and 50 μm under the given load. For the CT specimens with hydrides with larger ligament thicknesses, as the ligament thickness increases, the distribution of the effective plastic strain $\bar{\varepsilon}_p$ as a function of the radial distance r approaches to that for the CT specimen without hydride, where the effective plastic strain $\bar{\varepsilon}_p$ becomes large as the crack front is approached, at the given load. As shown in Figure B-2(b), the effective plastic strain $\bar{\varepsilon}_p$ ahead of the crack front for the CT specimen without hydride increases substantially when the normalized load increases from $P/P_0 = 0.63$ to $P/P_0 = 1.00$. Due to the singular nature of the crack front, the material elements at a finite radial distance r from the crack front are selected as the reference points to analyze the ductile fracture. As shown in Figure B-1, the distributions of the states of stress triaxiality α ahead of the crack front on the mid-planes of the CT specimen without hydride and with hydrides depend on the normalized load P/P_0 and the ligament thickness. It should be noted that in Section 2.3.2, the strain-based failure criterion is assumed without consideration of the stress triaxiality α. Therefore, a systematic analysis of the effects of the stress triaxiality α on the fracture initiation load needs to be performed.

First, the histories of the stress triaxiality α for the material elements at the radial distance of $r = 15$ μm ahead of the crack front on the mid-plane of the CT specimen without hydride and with hydrides with the heights of 50, 100, and 150 μm are plotted as functions of the normalized load P/P_0 and the effective plastic strain $\bar{\varepsilon}_p$ in Figures B-3 to B-5, respectively. As shown in the figures, after the initial elastic loading stages, the value of the stress triaxiality α in

general increases and then decreases as the effective plastic strain $\bar{\varepsilon}_p$ increases for the CT specimen without hydride. However, for the CT specimens with the small ligament thicknesses of 30 and 50 μm, the stress triaxiality α increases almost monotonically as the effective plastic strain $\bar{\varepsilon}_p$ increases. As shown in the figures, the values of the stress triaxiality α for all cases are all larger than 0.7 for the effective plastic strain $\bar{\varepsilon}_p$ larger than a small value such as 0.001. Therefore, the material elements ahead of the crack front for these cases should be fractured by the ductile fracture mechanism of void nucleation, growth and coalescence as suggested in Bao and Wierzbicki [5].

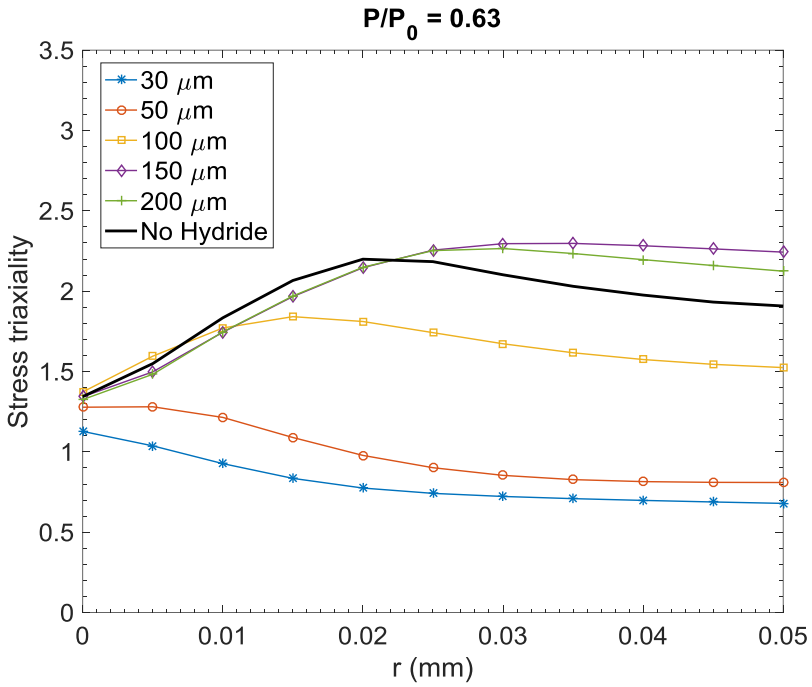

(a)

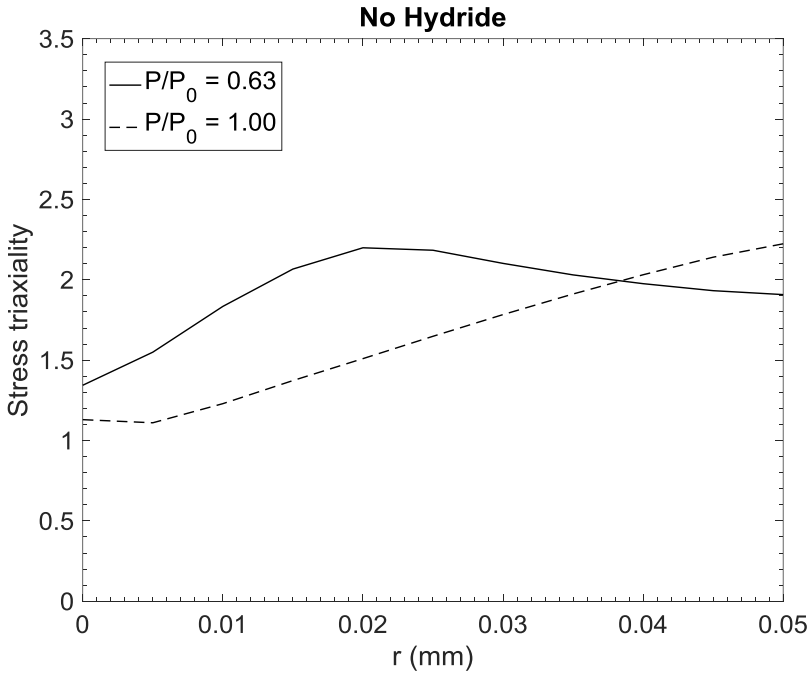

(b)

Figure B-1. The states of the stress triaxiality α for the material elements ahead of the crack front on the mid-planes of the CT specimen (a) without hydride and with hydrides with the height of 50 μm and different ligament thicknesses at $P/P_0 = 0.63$ and (b) without hydride at $P/P_0 = 0.63$ and $P/P_0 = 1.00$.

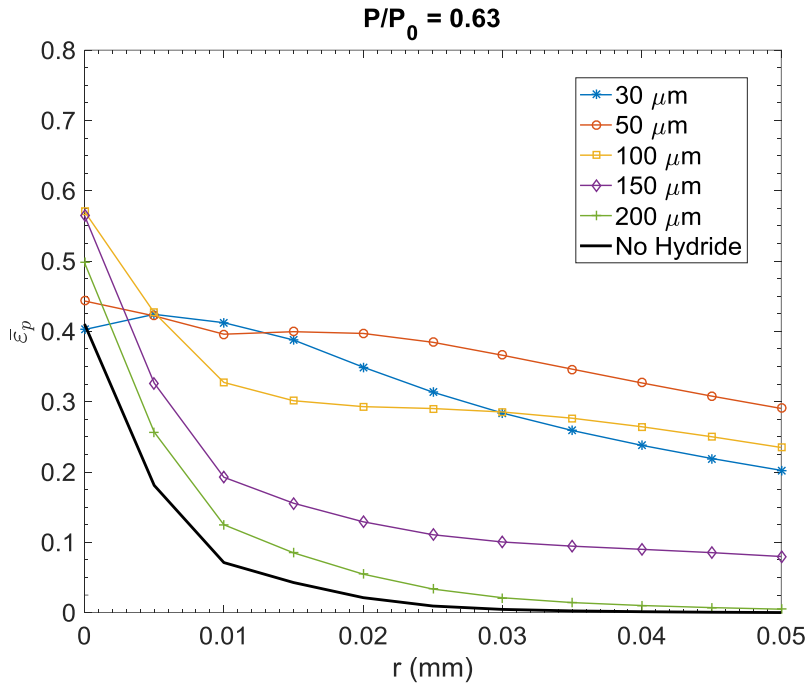

(a)

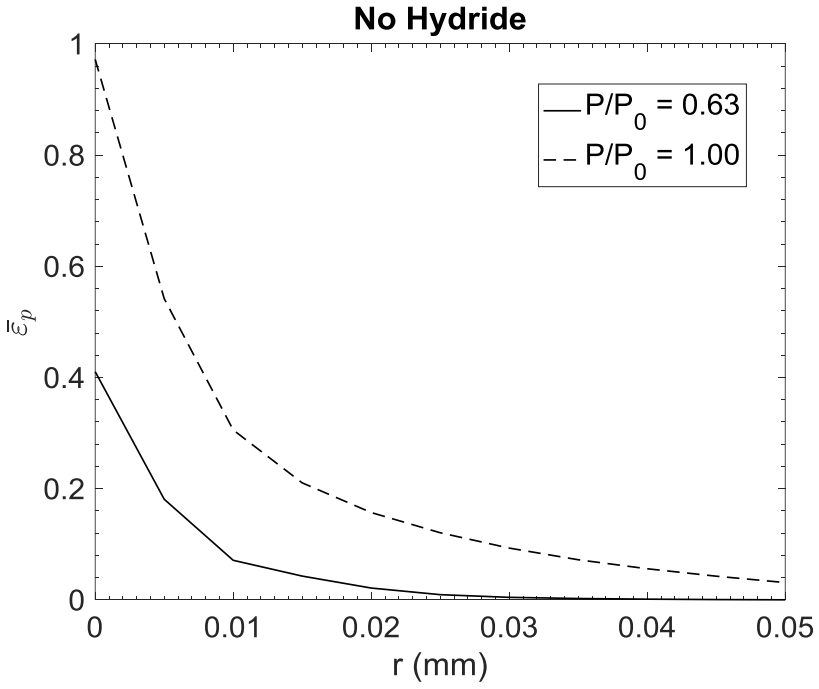

(b)

Figure B-2. The distributions of the effective plastic strain $\bar{\varepsilon}_p$ for the material elements ahead of the crack front on the mid-planes of the CT specimen (a) without hydride and with hydrides with the height of 50 μm and different ligament thicknesses at $P/P_0 = 0.63$ and (b) without hydride at $P/P_0 = 0.63$ and $P/P_0 = 1.00$.

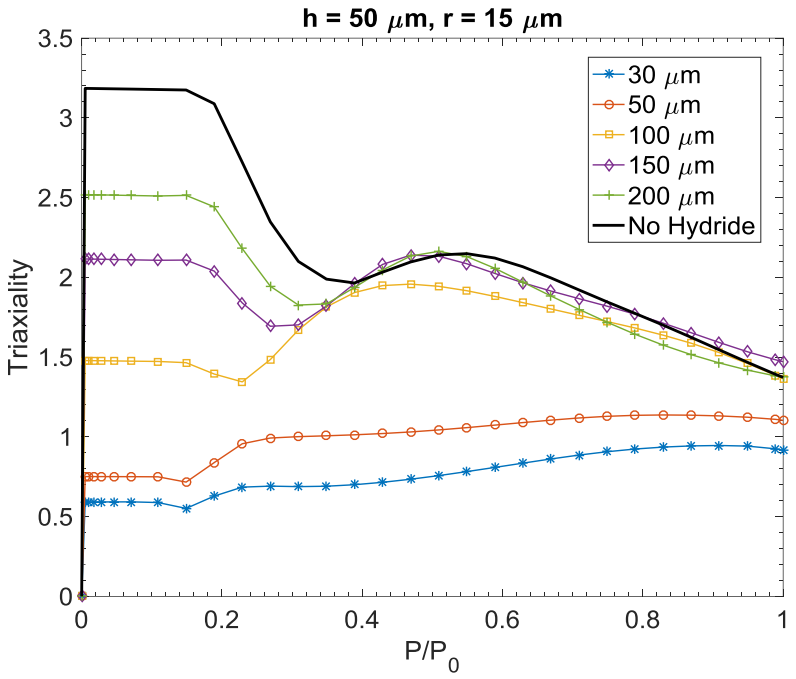

(a)

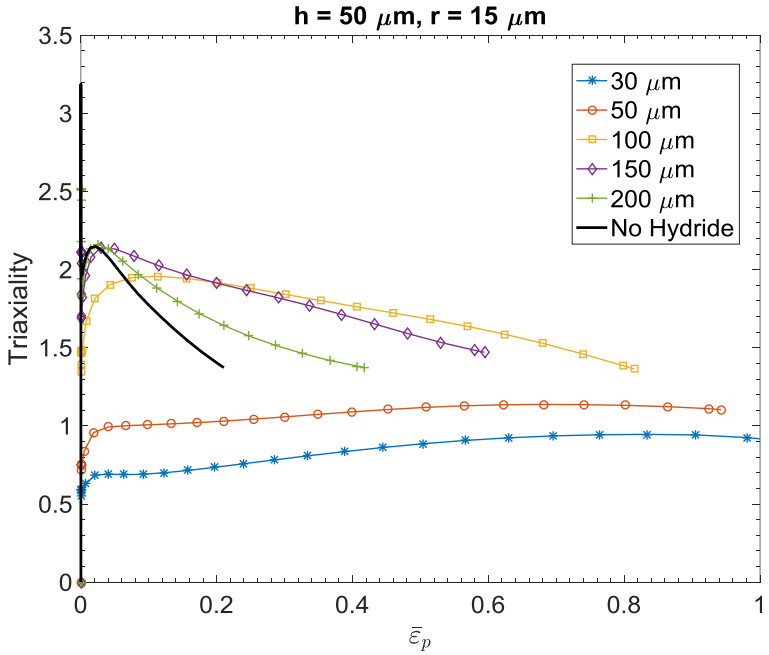

(b)

Figure B-3. The histories of the stress triaxiality α for the material elements at the radial distance of $r = 15$ μm ahead of the crack front on the mid-plane of the CT specimen without hydride and with hydrides of the height of 50 μm are plotted as functions of (a) the normalized load P / P_0 and (b) the effective plastic strain $\bar{\varepsilon}_p$.

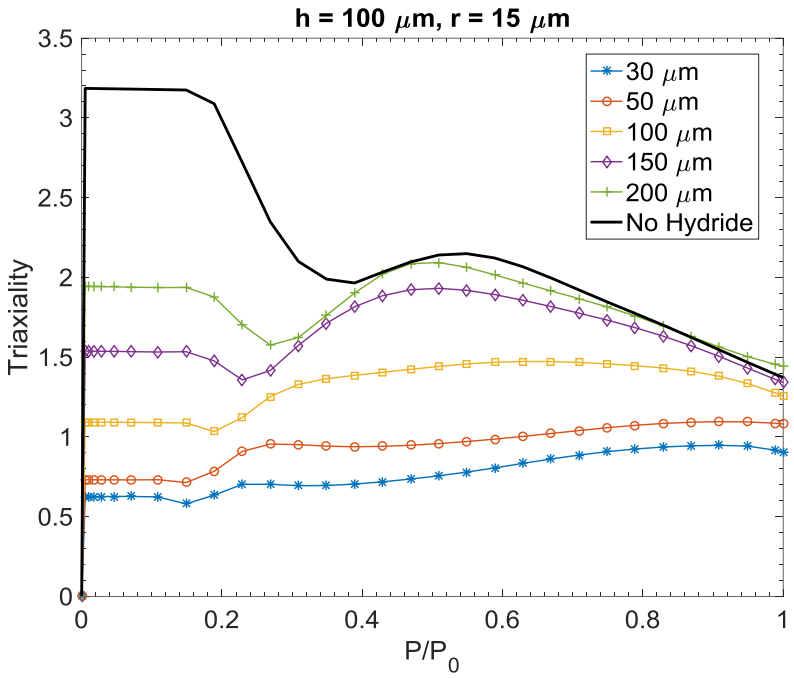

(a)

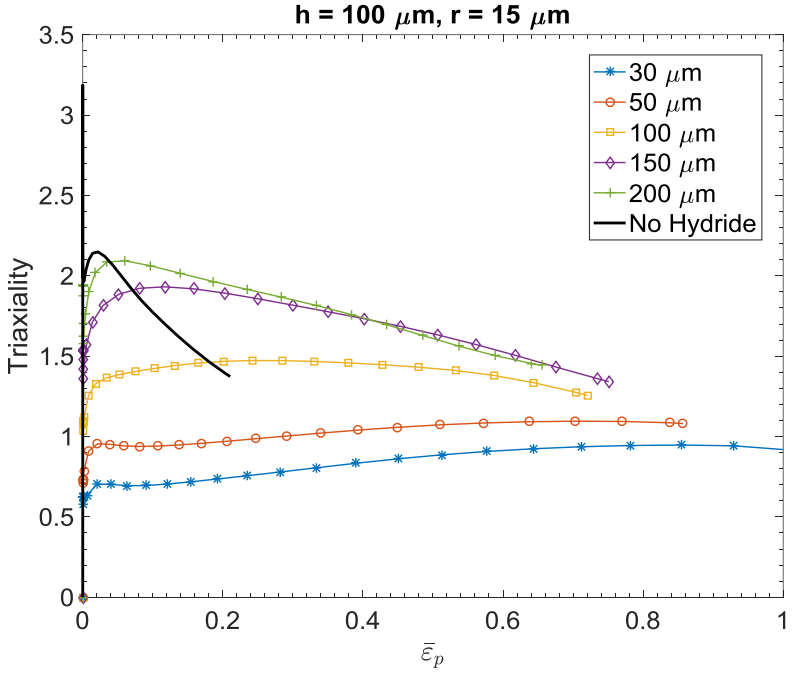

(b)

Figure B-4. The histories of the stress triaxiality α for the material elements at the radial distance of $r = 15$ μm ahead of the crack front on the mid-plane of the CT specimen without hydride and with hydrides of the height of 100 μm are plotted as functions of (a) the normalized load P/P_0 and (b) the effective plastic strain $\bar{\varepsilon}_p$.

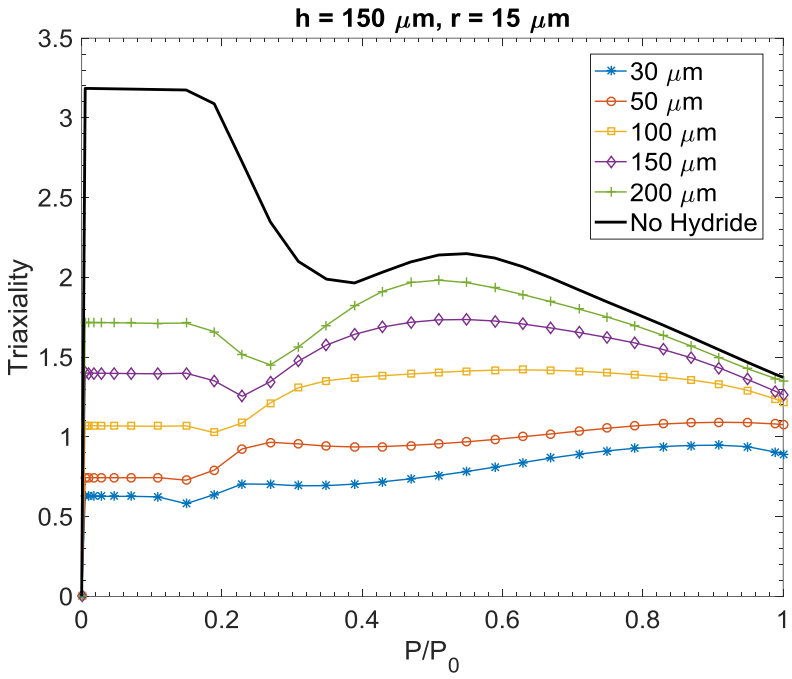

(a)

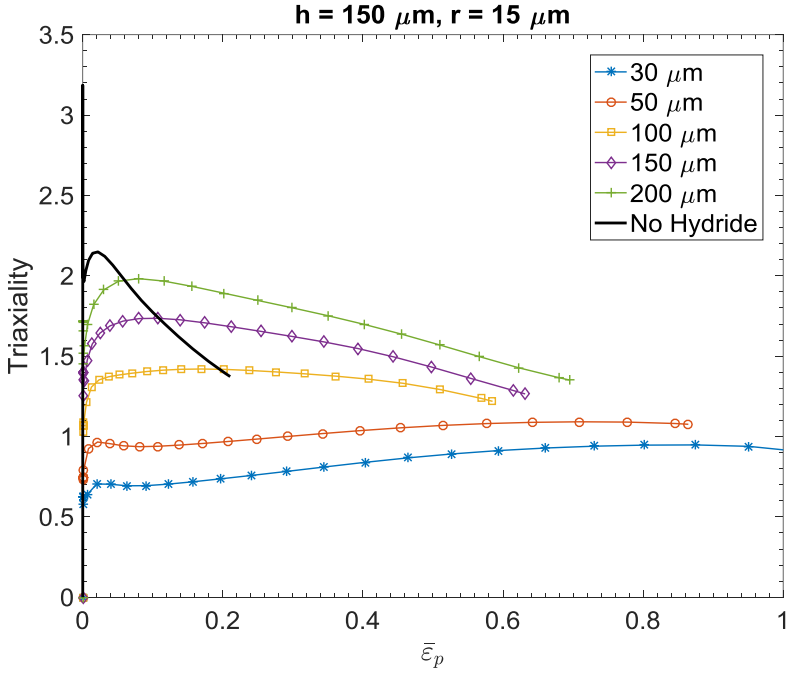

(b)

Figure B-5. The histories of the stress triaxiality α for the material elements at the radial distance of $r = 15$ μm ahead of the crack front on the mid-plane of the CT specimen without hydride and with hydrides of the height of 150 μm are plotted as functions of (a) the normalized load P/P_0 and (b) the effective plastic strain $\bar{\varepsilon}_p$.

Appendix C. Development of Strain Failure Criterion based on Gurson Model

The governing equations of the Gurson model to determine the failure effective plastic strain $\bar{\varepsilon}_p^f$ is derived and presented in this appendix. The Gurson yield function for voided materials is expressed as

$$\Phi = \left(\frac{\Sigma_e}{\sigma_f}\right)^2 + 2q_1 f \cosh\left(q_2 \frac{3\Sigma_m}{2\sigma_f}\right) - \left(1 + q_3 f^2\right) = 0 \qquad \text{(C-1)}$$

where f is the void volume fraction, Σ_m $(=\Sigma_{kk}/3)$ is the macroscopic hydrostatic tension based on the macroscopic stress Σ_{ij}, Σ_e $(=\sqrt{3\Sigma'_{ij}\Sigma'_{ij}/2})$ is the macroscopic effective stress which is based on the second invariant of the macroscopic deviatoric stress tensor Σ'_{ij} $(=\Sigma_{ij}-\Sigma_{kk}\delta_{ij}/3)$, and σ_f represents the matrix flow stress. The three parameters q_1, q_2 and q_3 were set to 1.5, 1.0 and 2.25, respectively, as in Tvergaard [44,45]. The matrix flow stress σ_f is set up as the tensile flow stress of the matrix material from the uniaxial tensile tests. The matrix flow stress σ_f is a function of the tensile plastic strain ε_p of the matrix material from the uniaxial tensile tests. Within the context of the Mises plasticity theory, ε_p is equal to the effective plastic strain $\bar{\varepsilon}_p$ during the deformation history. Here, σ_f as a function of ε_p (or $\bar{\varepsilon}_p$) is defined by the input tensile plastic hardening curve in Figure A-3 for our analyses. When the void volume fraction is set to zero, the Mises yield function is recovered from Equation (C-1). For this case, σ_f can be identified as the tensile effective stress σ_e and ε_p can be identified as the effective plastic strain $\bar{\varepsilon}_p$.

In our finite element analyses of the CT specimens, the Mises yield function is used to characterize the elastic-plastic behavior of irradiated Zr-2.5Nb materials. The failure effective plastic strain $\bar{\varepsilon}_p^f$ as a function of the stress triaxiality α for irradiated Zr-2.5Nb materials as that for aluminum alloy 2024-T351 in Bao and Wierzbicki [5] is needed and developed for determination of the fracture initiation load from the results of the finite element analyses based on the Mises plasticity theory. Within the context of the Gurson model, the macroscopic stress triaxiality α is defined as the ratio of the macroscopic hydrostatic tension Σ_m to the macroscopic effective stress Σ_e as

$$\alpha = \frac{\Sigma_m}{\Sigma_e} \tag{C-2}$$

The boundary conditions to use the Gurson model to develop the strain-based failure criterion in this investigation is to consider a material element with voids characterized by the Gurson yield function in Equation (C-1) with the void volume fraction f as an imperfection or a damage parameter under a given macroscopic stress triaxiality α history as a function of the effective plastic strain $\bar{\varepsilon}_p$. The void volume fraction f within the context of the Gurson model can also be viewed as a damage parameter. For example, the crack tip location for the investigation of crack growth resistances based on the Gurson model in Xia et al. [46] is selected at where the void volume fraction f is arbitrarily chosen as $f = 0.1$. In order to use the Gurson model to account for the effects of the stress triaxiality α on the failure effective plastic strain $\bar{\varepsilon}_p^f$, an initial void volume fraction f_0 and a critical failure void volume fraction f_f are needed as two fitting material parameters.

With the use of the Gurson model, the initial void volume fraction f_0 and the failure void volume fraction f_f are selected as 0.03 and 0.113, respectively, for the effective plastic strain $\bar{\varepsilon}_p$ of 0.21 with the corresponding stress triaxiality $\alpha(\bar{\varepsilon}_p)$ history for the material element at the radial distance of $r = 15$ μm ahead of the crack front on the mid-plane of the CT specimen without hydride at $K_C = 59.2\ \text{MPa}\cdot\sqrt{\text{m}}$. The selection of $f_0 = 0.03$ and $f_f = 0.113$ also gives the average failure engineering plastic strain of 0.093 of three transverse tensile tests of irradiated Zr-2.5Nb materials, as detailed in Appendix D. Based on the selection of $f_0 = 0.03$ and $f_f = 0.113$, different values of the failure effective plastic strain $\bar{\varepsilon}_p^f$ can be obtained for different stress triaxiality $\alpha(\bar{\varepsilon}_p)$ histories.

Essentially, a perturbation analysis is performed here based on the unperturbed solution which is the finite element solution of the CT specimen without hydride based on the Mises yield function with the material stress-strain curve defined in Appendix A. Here, the stress triaxiality α as a function of the effective plastic strain $\bar{\varepsilon}_p$ from the finite element analysis based on the Mises yield function is adopted for the Gurson model with consideration of voids as the imperfection or the damage parameter that will lead to ductile fracture from the initial void volume fraction f_0 to the failure void volume fraction f_f, which essentially is viewed as a critical damage parameter.

Based on the associated flow rule, the macroscopic plastic strain increments dE_{ij}^p can be expressed as

$$dE_{ij}^p = d\Lambda \frac{\partial \Phi}{\partial \Sigma_{ij}} = d\Lambda \left[\frac{2\Sigma_e}{\sigma_f^2} \frac{\partial \Sigma_e}{\partial \Sigma_{ij}} + \frac{q_1 q_2}{\sigma_f} f \sinh(q_2 \frac{3}{2} \frac{\Sigma_m}{\sigma_f}) \delta_{ij} \right] \tag{C-3}$$

where $d\Lambda$ is the proportionality factor. Based on Equation (C-3), the macroscopic volumetric plastic strain increment dE_{kk}^{p} can be expressed as

$$dE_{kk}^{p} = d\Lambda\left[3\frac{q_1 q_2}{\sigma_f} f \sinh(q_2 \frac{3}{2}\frac{\Sigma_m}{\sigma_f})\right] \tag{C-4}$$

and the macroscopic plastic work increment dW_p can be written as

$$dW_p = \Sigma_{ij} dE_{ij}^{p} = d\Lambda\left[2(\frac{\Sigma_e}{\sigma_f})^2 + 3\frac{\Sigma_m}{\sigma_f} q_1 q_2 f \sinh(q_2 \frac{3}{2}\frac{\Sigma_m}{\sigma_f})\right] \tag{C-5}$$

Also, the matrix plastic work increment can be related to the macroscopic plastic work increment dW_p by

$$dW_p = \Sigma_{ij} dE_{ij}^{p} = (1-f)\sigma_f d\bar{\varepsilon}_p \tag{C-6}$$

where $d\bar{\varepsilon}_p$ is the effective plastic strain increment and it can be determined as a function of $d\Lambda$ by combining Equations (C-5) and (C-6) as

$$d\bar{\varepsilon}_p = \frac{1}{1-f}\frac{d\Lambda}{\sigma_f}\left[2(\frac{\Sigma_e}{\sigma_f})^2 + 3\frac{\Sigma_m}{\sigma_f} q_1 q_2 f \sinh(q_2 \frac{3}{2}\frac{\Sigma_m}{\sigma_f})\right] \tag{C-7}$$

The void volume fraction increment df can also be related to the macroscopic volumetric plastic strain increment dE_{kk}^{p} through the current void volume fraction f as

$$df = (1-f)dE_{kk}^{p} = (1-f)\frac{d\Lambda}{\sigma_f}\left[3q_1 q_2 f \sinh(q_2 \frac{3}{2}\frac{\Sigma_m}{\sigma_f})\right] \tag{C-8}$$

where the macroscopic volumetric plastic strain increment dE_{kk}^{p} is replaced by the expression in Equation (C-4). It should be mentioned that the void volume fraction increment df in Equation (C-8) is also a function of $d\Lambda$.

The relationship between the effective plastic strain increment $d\bar{\varepsilon}_p$ and the void volume fraction increment df can be obtained by combining Equations (C-7) and (C-8) as

$$d\bar{\varepsilon}_p = \left\{ \frac{1}{f(1-f)^2} \frac{2(\frac{\Sigma_e}{\sigma_f})^2}{3q_1 q_2 \sinh(q_2 \frac{3}{2}\frac{\alpha\Sigma_e}{\sigma_f})} + \frac{\alpha \frac{\Sigma_e}{\sigma_f}}{(1-f)^2} \right\} df \tag{C-9}$$

where α is the macroscopic stress triaxiality. With the initial void volume fraction denoted as f_0 and the failure void volume fraction denoted as f_f, the failure effective plastic strain $\bar{\varepsilon}_p^f$ can now be written as an integral equation as

$$\bar{\varepsilon}_p^f = \int_0^{\bar{\varepsilon}_p^f} d\bar{\varepsilon}_p = \int_{f_0}^{f_f} F(f, \sigma_f(\bar{\varepsilon}_p), \alpha(\bar{\varepsilon}_p)) df \tag{C-10}$$

where

$$F(f, \sigma_f(\bar{\varepsilon}_p), \alpha(\bar{\varepsilon}_p)) = \frac{1}{f(1-f)^2} \frac{2(\frac{\Sigma_e}{\sigma_f})^2}{3q_1 q_2 \sinh(q_2 \frac{3}{2}\frac{\alpha\Sigma_e}{\sigma_f})} + \frac{\alpha \frac{\Sigma_e}{\sigma_f}}{(1-f)^2} \tag{C-11}$$

It should be mentioned that in the integrand $F(f, \sigma_f, \alpha)$ in Equation (C-11), the stress triaxiality α and the matrix flow stress σ_f are both functions of the effective plastic strain $\bar{\varepsilon}_p$. The function $\sigma_f(\bar{\varepsilon}_p)$ is the material stress-strain curve defined in Appendix A. The function $\alpha(\bar{\varepsilon}_p)$ is the stress triaxiality history as a function of the effective plastic strain $\bar{\varepsilon}_p$ for the element of interest from the finite element analyses based on the Mises yield function, as shown in Figures B-3 to B-5. Under the plastic loading conditions with $d\bar{\varepsilon}_p > 0$, the Gurson yield function Φ identically equals 0. Therefore, the macroscopic effective stress Σ_e in the integrand $F(f, \sigma_f, \alpha)$ can be determined by the yield function of $\Phi = 0$ if the void volume fraction f and the effective

tensile plastic strain $\bar{\varepsilon}_p$ are given. A numerical integration scheme with consideration of iterations in each integration step is adopted to solve Equations (C-10) and (C-11).

In order to show the effects of the stress triaxiality α on the failure effective plastic strain $\bar{\varepsilon}_p^f$, $\bar{\varepsilon}_p^f$ as a function of α under constant α conditions is plotted in Figure 2-24. As shown in the figure, $\bar{\varepsilon}_p^f$ decreases as α increases. The curve shown in Figure 2-24 can be fitted by a 6th order polynomial as listed below

$$f(\alpha) = 0.125\alpha^6 - 1.16\alpha^5 + 4.50\alpha^4 - 9.32\alpha^3 + 11.2\alpha^2 - 7.71\alpha + 2.75 \quad \text{(C-12)}$$

The fitted function of $\bar{\varepsilon}_p^f$ can be used conveniently when the average stress triaxiality $\overline{\alpha}$ of Bao and Wierzbicki [5] is used to determine the failure of the irradiated Zr-2.5Nb materials.

Appendix D. Strain-Based Failure Criterion of Transverse Tensile Tests

The strain-based failure criterion for the transverse tensile tests is determined by three-dimensional finite element analyses in this appendix. The detailed geometry, boundary conditions and material definition of the three-dimensional finite element model for the transverse tensile specimens are already described in Appendix A and will not be repeated here. In order to assess the mesh sensitivity of the computational results, two meshes with different element sizes as shown in Figures A-2 and D-1 are considered. The coarse mesh in Figure A-2 has the smallest element size of 0.1 mm by 0.05 mm by 0.1 mm while the fine mesh in Figure D-1 has the smallest element size of 0.01 mm by 0.01 mm by 0.01 mm near the center of the transverse tensile specimen. The three-dimensional linear element with reduced integration (C3D8R) was used for the analysis in ABAQUS. A displacement of 0.55 mm was applied to the top surface of the finite element model. The displacement results in the engineering strain of 11% for the specimen.

Figures D-2(a) and (b) show the histories of the stress triaxiality α for the material elements of the two meshes at the center of the transverse tensile specimen, plotted as functions of the engineering plastic strain and the effective plastic strain $\bar{\varepsilon}_p$, respectively. In the figures, the stress triaxiality α monotonically increase from 0.33 (uniaxial tension) to 0.86 at the displacement of 0.55 mm. Only a small amount of mesh sensitivity is observed in Figures D-2 (a) and (b). Therefore, only the computational results with the fine mesh will be discussed here.

With the governing equations based on the Gurson model as presented in Appendix C, the failure effective plastic strains $\bar{\varepsilon}_p^f$ can now be calculated from the stress triaxiality history

$\alpha(\bar{\varepsilon}_p)$ for the center element of the tensile specimen as presented in Figure D-2(b) and the material stress-strain curve $\sigma_f(\bar{\varepsilon}_p)$ presented in Appendix A. The failure effective plastic strains $\bar{\varepsilon}_p^f$ is determined as 0.636 based on the governing equations of the Gurson model with the initial void volume fraction $f_0 = 0.03$ and the failure void volume fraction $f_f = 0.113$. When the effective plastic strain $\bar{\varepsilon}_p$ at the center element of the transverse tensile specimen reaches to 0.636, the engineering plastic strain is 0.093, which can be treated as the failure engineering plastic strain. The failure engineering plastic strain of 0.093 from the simulation equals the average of the three transverse tensile tests with the failure engineering plastic strains of 0.089, 0.091 and 0.098 [38]. Note the selection of $f_0 = 0.03$ and $f_f = 0.113$ represents the best fit to both the failure engineering plastic strain of the transverse tensile tests and the failure effective plastic strain of 0.21 for the material element at $r = 15$ μm ahead of the crack front in the CT specimen without hydride at K_C.

In order to show the average stress triaxiality $\bar{\alpha}$ and the corresponding failure effective plastic strain $\bar{\varepsilon}_p^f$ for the center element in the transverse tensile specimen, the approach of Bao and Wierzbicki [5] is also adopted with the use of the average stress triaxiality $\bar{\alpha}$ defined in Equation (2-3). The average stress triaxiality $\bar{\alpha}$ can be calculated as a function of the effective plastic strain $\bar{\varepsilon}_p$ based on the stress triaxiality history $\alpha(\bar{\varepsilon}_p)$ for the center element. With the relation of the failure effective plastic strain $\bar{\varepsilon}_p^f$ under the constant stress triaxiality α as shown in Figure 2-24, the failure effective plastic strains $\bar{\varepsilon}_p^f$ can also be expressed as a function of the effective plastic strain $\bar{\varepsilon}_p$ with the average stress triaxiality $\bar{\alpha}$ as shown in Figure D-3. In the figure, when the curves of $\bar{\varepsilon}_p^f$ and $\bar{\varepsilon}_p$ intercept ($\bar{\varepsilon}_p^f(\bar{\varepsilon}_p) = \bar{\varepsilon}_p$), the failure condition is met. As

shown in the figure, the results are almost the same for the fine and coarse meshes. In the transverse tensile tests, the average stress triaxiality $\bar{\alpha}$ for the material element at the center of the transverse tensile specimen is 0.603 when the effective plastic strain $\bar{\varepsilon}_p$ reaches the failure effective plastic strains $\bar{\varepsilon}_p^f$ of 0.634 for the fine mesh. The corresponding failure engineering plastic strain is also about 0.093. The data point is plotted as a solid square in Figure 2-24. As shown in Figure 2-24, the results of the Gurson model approach presented in Appendix C and the average stress triaxiality approach of Bao and Wierzbicki [5] are consistent with each other to correlate to the results of the transverse tensile tests.

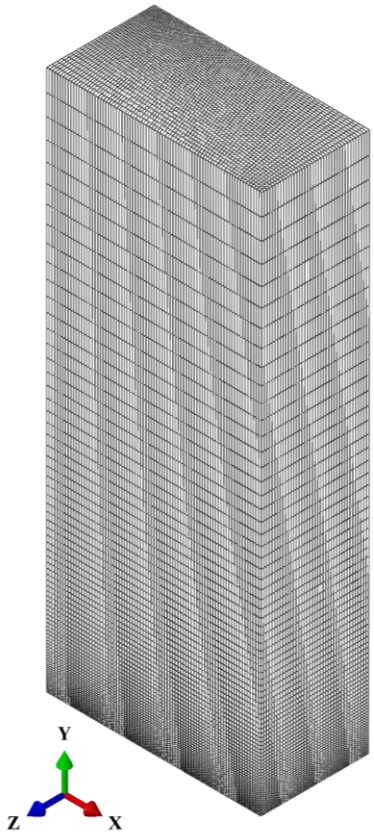

Figure D-1. A three-dimensional finite element model with a fine mesh for one eighth of the gauge section of a transverse tensile specimen.

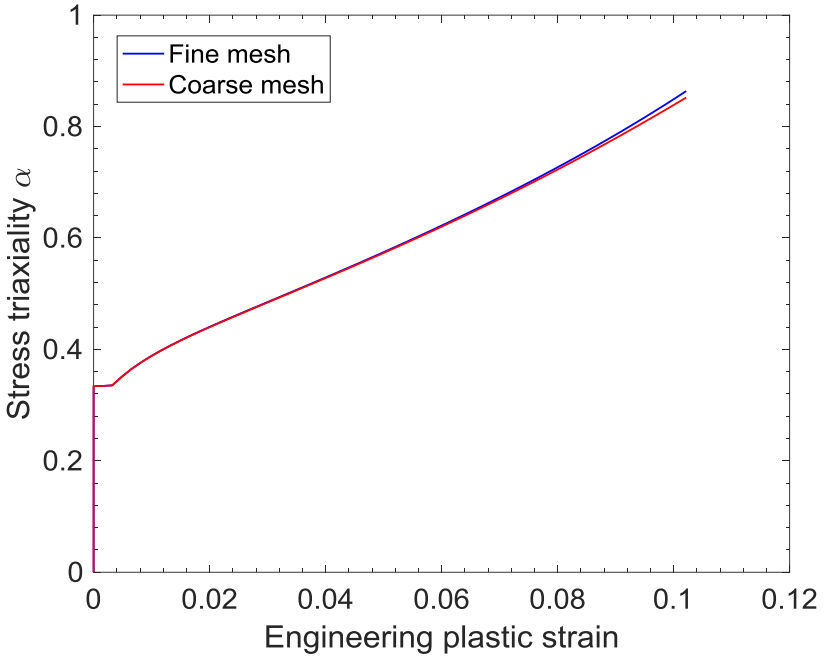

(a)

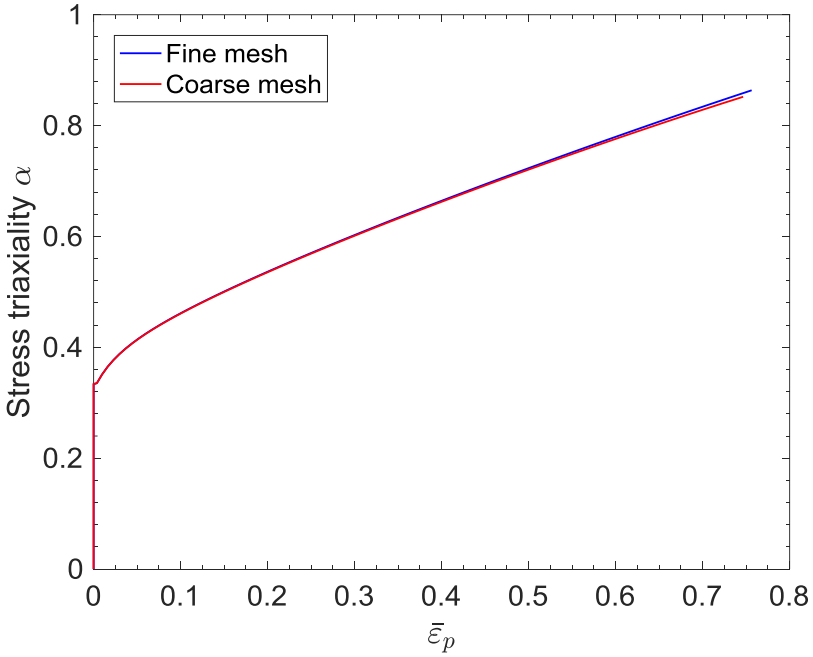

(b)

Figure D-2. The histories of the stress triaxiality α for the material elements of two different meshes at the center of the transverse tensile specimen are plotted as functions of (a) the engineering plastic strain and (b) the effective plastic strain $\bar{\varepsilon}_p$.

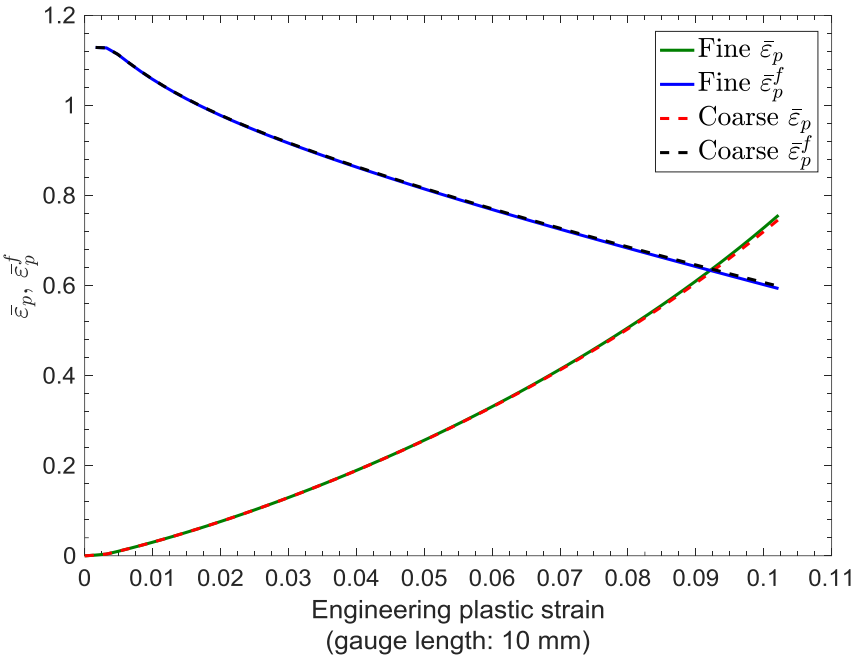

Figure D-3. The histories of the effective plastic strain $\bar{\varepsilon}_p$ and the corresponding failure effective plastic strain as functions of the engineering plastic strain for the finite element models with the fine and coarse meshes.

Appendix E. Derivation of the Applied Internal Pressure

In order to calculate the stress intensity factor for an axial crack in a cylindrical or spherical shell, a geometric factor called the bulging factor should be considered to account for the effects of bending resulting from the curvature of a tube wall. Folias [16] provided an asymptotic expression of the integral equation for the bulging factor. However, the asymptotic expression is feasible only for a large pipe with a relatively small crack. Later, Erdogan and Kibler [15] numerically tabulated the solution of the integral equation and expanded its applicability. Barrois [6] fitted the tabulated solutions with a linear equation in a certain applicable range of the shell parameter λ. In this investigation, the works of Erdogan and Kibler [15] and Barrois [6] are followed to calculate the bulging factor.

In Barrois [6], the bulging factor F is expressed as a linear function of the shell parameter λ as

$$F(\lambda) = 0.64 + 0.49\lambda \tag{E-1}$$

where the shell parameter λ is

$$\lambda = \left[12\left(1-\nu^2\right)\right]^{0.25} \frac{a}{\sqrt{R_m T}} \tag{E-2}$$

Here, ν is the Poisson's ratio, a is the half-crack length, R_m is the mean radius, and T is the shell thickness. The applicable range of the shell parameter λ in Equation (E-1) is between 2 to 6. In this investigation, the pressure tube specimen has the half crack length a of 27.5 mm, the mean radius R_m of 54 mm, the thickness T of 4 mm and the Poisson's ratio ν of 0.4. Based on Equations (E-1) and (E-2), the bulging factor can be calculated as 2.2737 based on the shell

parameter of λ of 3.334, which is in the applicable range between 2 to 6. It should be noted that the bulging factor $F = 2.2737$ is quite close to the one listed in the stress analysis of cracks handbook [41], which does not explicitly consider the effect of Poisson's ratio.

With consideration of the bulging factor $F = 2.2737$, the mode I stress intensity factor solution for an axial crack in a pressure tube can be expressed as

$$K_I = F(\lambda)\sigma_h\sqrt{\pi a} \tag{E-3}$$

where the hoop stress σ_h is

$$\sigma_h = p\frac{R_i}{T} \tag{E-4}$$

and p is the internal pressure, T is the thickness of the pressure tube, and R_i is the inner radius, which is 52 mm. In order to have the same K_C (= 59.2 $\text{MPa}\cdot\sqrt{\text{m}}$) as that in the earlier investigation of CT specimens in Chapter 2, the internal pressure p should reach 6.815 MPa and the corresponding hoop stress σ_h is calculated as 88.595 MPa. When a pressure tube is closed, the tensile stress σ_a in the axial direction of the pressure tube is

$$\sigma_a = p\frac{R_i^2}{R_o^2 - R_i^2} \tag{E-5}$$

where R_o is the outer radius, and R_o is 56 mm. With the internal pressure p of 6.815 MPa, the inner radius R_i of 52 mm and the outer radius R_o of 56 mm, the corresponding axial tensile stress is calculated as 42.657 MPa.

Bibliography

[1] Aitchison, I., 1969, "The Effect of Orientation of Hydride Precipitates on the Fracture Toughness of Cold-Rolled Zircaloy-2 and 2.5Nb Zirconium," *Applications-Related Phenomena in Zirconium and its Alloys*, STP43826S, B. Committee, Ed., ASTM International, West Conshohocken, PA, 1969, pp. 160-178. https://doi.org/10.1520/STP43826S

[2] Aitchison, I. and Davies, P.H., 1993, "Role of Microsegregation in Fracture of Cold-Worked Zr-2.5Nb Pressure Tubes," Journal of Nuclear Materials, **203**, pp. 206–220. https://doi.org/10.1016/0022-3115(93)90377-B

[3] Amodeo, C. M., Lai, W.-J., Lee, J., and Pan, J., 2014, "Failure Modes of Gas Metal Arc Welds in Lap-Shear Specimens of High Strength Low Alloy (HSLA) Steel," Engineering Fracture Mechanics, **131**, pp. 74–99. https://doi.org/10.1016/j.engfracmech.2014.07.009

[4] ASTM Standard E399, 2013, "Standard Test Method for Linear-Elastic Plane-Strain Fracture Toughness K_{Ic} of Metallic Materials," ASTM International, West Conshohocken, PA. https://doi.org/10.1520/E0399

[5] Bao, Y. and Wierzbicki, T., 2004, "On Fracture Locus in the Equivalent Strain and Stress Triaxiality Space," International Journal of Mechanical Sciences, **46**(1), pp. 81–98. https://doi.org/10.1016/j.ijmecsci.2004.02.006

[6] Barrois, W., 1975, "Practical Use of the 'Equivalent' Measured Stress Intensity Factor to Control Fatigue Crack Propagation Rates in Aircraft Full-Scale Fatigue Tests—First Assessment of the Method in Testing of a Pressurized Aircraft Fuselage," Engineering Fracture Mechanics, **7**(4), pp. 673–688. https://doi.org/10.1016/0013-7944(75)90023-5

[7] Cheadle, B. A., Coleman, C. E. and Licht, H., 1982, "CANDU-PHW Pressure Tubes: Their Manufacture, Inspection, and Properties," Nuclear Technology, **57**, pp. 413–425. https://doi.org/10.13182/NT82-A26307

[8] Choubey, R. and Puls, M. P., 1994, "Crack Initiation at Long Radial Hydrides in Zr-2.5Nb Pressure Tube Material at Elevated Temperatures," Metallurgical and Materials Transactions A, **25A**, pp. 993–1004. https://doi.org/10.1007/BF02652274

[9] Chow, C. K. and Simpson, L. A., 1988, "Determination of the Fracture Toughness of Irradiated Reactor Pressure Tubes Using Curved Compact Specimens," *Fracture Mechanics: Eighteenth Symposium*, ASTM STP 945, ASTM International, West Conshohocken, PA, pp. 419–439. https://doi.org/10.1520/STP23256S

[10] Chow, C. K., Coleman, C. E., Hosbons, R. R., Davies, P. H., Griffiths, M. and Choubey, R., 1991, "Fracture Toughness of Irradiated Zr-2.5Nb Pressure Tubes from CANDU Reactors," *Zirconium in the Nuclear Industry: Ninth International Symposium*, ASTM STP 1132, ASTM International, West Conshohocken, PA, pp. 246–275. https://doi.org/10.1520/STP25511S

[11] Cottrell, A. H., 1965, "Mechanisms of Fracture," Proceedings of the First Tewksbury Symposium, published by the Faculty of Engineering, University of Melbourne, Australia, edited by C.J. Osborn, pp. 1-27.

[12] Cui, J. and Shek, G. K., 2009, "Effects of Hydride Morphology and Test Temperature on Fracture Toughness of Zr-2.5Nb Pressure Tube Material," *Proceedings of the ASME 2009 Pressure Vessels and Piping Division Conference*, PVP2009-77260, pp. 81–96. https://doi.org/10.1115/PVP2009-77260

[13] Davies, P. H. and Shewfelt, R. S. W., 1996, "Link Between Results of Small- and Large-Scale Toughness Tests on Irradiated Zr-2.5Nb Pressure Tube Material," *Zirconium in the Nuclear Industry: 11th International Symposium*, ASTM STP 1295, ASTM International, West Conshohocken, PA, pp. 492–517. https://doi.org/10.1520/STP16187S

[14] Davies, P. H., Himbeault, D. D., Shewfelt, R. S. W. and Hosbons, R. R., 2001, "Crack Growth Resistance of Irradiated Zr-2.5Nb Pressure Tube Material at Low Hydrogen Levels," *Effects of Radiation on Materials: 20th International Symposium*, ASTM STP 1405, ASTM International, West Conshohocken, PA, pp. 846–868. https://doi.org/10.1520/STP10577S

[15] Erdogan, F. and Kibler, J. J., 1969, "Cylindrical and Spherical Shells with Cracks," International Journal of Fracture Mechanics, **5**(3), pp. 229–237. https://doi.org/10.1007/BF00184614

[16] Folias, E. S., 1965, "An Axial Crack in a Pressurized Cylindrical Shell," International Journal of Fracture Mechanics, **1**(2), pp. 104–113. https://doi.org/10.1007/BF00186748

[17] Gurson, A. L, 1977, "Continuum Theory of Ductile Rupture by Void Nucleation and Growth: Part I—Yield Criteria and Flow Rules for Porous Ductile Media," Journal of Engineering Materials and Technology, **99**(1), pp. 2–15. https://doi.org/10.1115/1.3443401

[18] Hardie, D. and Shanahan, M. W., 1975, "Stress Reorientation of Hydrides in Zirconium−2.5% Niobium," Journal of Nuclear Materials, **55**, pp. 1–13. https://doi.org/10.1016/0022-3115(75)90132-4

[19] "Image Library," *Canteach.Candu.Org*. CANTEACH: The Most Comprehensive Public Domain Educational and Reference Library on CANDU Technology, Retrieved from on 01/17/2018.

[20] Kubo, T., Kobayashi, Y. and Uchikoshi, H., 2013, "Determination of Fracture Strength of δ-Zirconium Hydrides Embedded in Zirconium Matrix at High Temperatures," Journal of Nuclear Materials, **435**, pp. 222–230. https://doi.org/10.1016/j.jnucmat.2012.12.045

[21] Liu, C., Gutkin, L. and Scarth, D. A., 2016, "Quantitative Characterization of Hydride Spacing for Cohesive-Zone Modelling of Fracture Toughness in Zr-2.5Nb Pressure Tubes," *Proceedings of the ASME 2016 Pressure Vessels and Piping Conference*, Vancouver, British Columbia, Canada, PVP2016-63073. https://doi.org/10.1115/PVP2016-63073

[22] Murty, K. L. and Charit, I., 2013, "*An Introduction to Nuclear Materials: Fundamentals and Applications*," Wiley-VCH, Weinheim, Germany, Chap. 1.

[23] Northwood, D. O. and Kosasih, U., 1983, "Hydrides and Delayed Hydrogen Cracking in Zirconium and its Alloys," International Metals Reviews, **28**(2), pp. 92–121. https://doi.org/10.1179/imtr.1983.28.1.92

[24] Pan, J., Sung, S.-J. and Lam, P.-S., 2016, "Progress Report on Verification of Cohesive-Zone Fracture Toughness Model against Finite Element Cohesive-Zone Analysis," Kinectrics Inc., unpublished work.

[25] Puls, M. P., 2012, "*The Effect of Hydrogen and Hydrides on the Integrity of Zirconium Alloy Components: Delayed Hydride Cracking*," Springer, London. https://doi.org/10.1007/978-1-4471-4195-2

[26] Rice, J. R., 1968, "A Path Independent Integral and the Approximate Analysis of Strain Concentration by Notches and Cracks," Journal of Applied Mechanics, **35**(2), 379–386. https://doi.org/10.1115/1.3601206

[27] Scarth, D. A., Liu, C., Xu, S. X. and Gutkin, L., 2013, "Cohesive-Zone Based Fracture Toughness Model for Zr- 2.5Nb Pressure Tubes," Kinectrics Inc., unpublished work.

[28] Shek, G. K., 2012, "Fracture Stress of Hydrides for Engineering Fracture Toughness Model," Kinectrics Inc., unpublished work.

[29] Shi, S.-Q. and Puls, M. P., 1999, "Fracture Strength of Hydride Precipitates in Zr–2.5Nb Alloys," Journal of Nuclear Materials, **275**(3), pp. 312–317. https://doi.org/10.1016/S0022-3115(99)00132-4

[30] Simpson, L. A. and Cann, C. D., 1979, "Fracture Toughness of Zirconium Hydride and its Influence on the Crack Resistance of Zirconium Alloys," Journal of Nuclear Materials, **87**, pp. 303–316. https://doi.org/10.1016/0022-3115(79)90567-1

[31] Simpson, L. A., 1981, "Criteria for Fracture Initiation at Hydrides in Zirconium-2.5 Pct Niobium Alloy," Metallurgical Transactions A, **12A**, pp. 2113–2124. https://doi.org/10.1007/BF02644181

[32] Simpson, L. A. and Chow, C. K., 1987, "Effect of Metallurgical Variables and Temperature on the Fracture Toughness of Zirconium Alloy Pressure Tubes," *Zirconium in the Nuclear*

Industry: Seventh International Symposium, ASTM STP 939, ASTM International, West Conshohocken, PA, pp. 579–596. https://doi.org/10.1520/STP28145S

[33] Singh, R. N., Kishore, R., Singh, S. S., Sinha, T. K., and Kashyap, B. P., 2004, "Stress-Reorientation of Hydrides and Hydride Embrittlement of Zr-2.5 wt% Nb Pressure Tube Alloy," Journal of Nuclear Materials, **325**(1), pp. 26–33. https://doi.org/10.1016/j.jnucmat.2003.10.009

[34] Smith, E. and Davies, P. H., 1995, "Modelling the Fissuring Flat-Fracture Mode of Crack Growth in Zr-2.5Nb CANDU Pressure-Tube Material," Journal of Materials Science, **30**(3), pp. 561–567. https://doi.org/10.1007/BF00356311

[35] Smith, E. and Davies, P. H., 1996, "Modelling the Softening within the Fracture Process Zone Associated with the Fissuring Mode of Crack Growth in Zr-2.5Nb CANDU Pressure Tube Material," Journal of Materials Science, **31**(4), pp. 835–841. https://doi.org/10.1007/BF00352880

[36] St Lawrence, S., 2011, "Update: Fracture Toughness Experimental Programs, Small- and Large-Scale Tests of Irradiated Material," Private Communication, Canadian Nuclear Laboratories, Chalk River, Ontario, Canada.

[37] St Lawrence, S., 2012, "Fracture Toughness Database for Irradiated Material," Private Communication, Canadian Nuclear Laboratories, Chalk River, Ontario, Canada.

[38] St Lawrence, S., 2012, "Influence of Annealing and Hydrides on the Tensile Properties of Irradiated Pressure Tube Material," Kinectrics Inc., unpublished work.

[39] Sung, S.-J., Pan, J., Lam, P.-S. and Scarth, D. A., 2016, "Three-Dimensional Finite Element Analyses of Compact Tension Specimens of Irradiated Zr-2.5Nb Materials Using Submodeling," *Proceedings of the ASME 2016 Pressure Vessels and Piping Conference*, Vancouver, British Columbia, Canada, PVP2016-63862. https://doi.org/10.1115/PVP2016-63862

[40] Sung, S.-J., Pan, J., Lam, P.-S. and Scarth, D. A., 2016, "Three-Dimensional Finite Element Analyses of Thin-Sliced Compact Tension Specimens of Irradiated Zr-2.5Nb Materials with Consideration of Split Circumferential Hydrides," *Proceedings of the ASME 2016 Pressure Vessels and Piping Conference*, Vancouver, British Columbia, Canada, PVP2016-63863. https://doi.org/10.1115/PVP2016-63863

[41] Tada, H., Paris, P. C., and Irwin, G. R., 2000, The Stress Analysis of Cracks Handbook, Third Edition, ASME, Three Park Avenue New York, NY 10016-5990. https://doi.org/10.1115/1.801535

[42] *The Essential CANDU, A Textbook on the CANDU Nuclear Power Plant Technology*, Editor-in-Chief Wm. J. Garland, University Network of Excellence in Nuclear Engineering (UNENE), ISBN 0-9730040. Retrieved from https://www.unene.ca/education/candu-textbook on 01/16/2018.

[43] Theaker, J., Choubey, R., Moan, G., Aldridge, S., Davis, L., Graham, R. and Coleman, C., 1994, "Fabrication of Zr-2.5Nb Pressure Tubes to Minimize the Harmful Effects of Trace Elements," *Zirconium in the Nuclear Industry: Tenth International Symposium*, ASTM STP 1245, ASTM International, West Conshohocken, PA, pp. 221–242. https://doi.org/10.1520/STP15192S

[44] Tvergaard, V., 1981, "Influence of Voids on Shear Band Instabilities under Plane Strain Conditions," International Journal of Fracture, **17**(4), pp. 389–407. https://doi.org/10.1007/BF00036191

[45] Tvergaard, V., 1982, "On Localization in Ductile Materials Containing Spherical Voids," International Journal of Fracture, **18**(4), pp. 237–252. https://doi.org/10.1007/BF00015686

[46] Xia, L., Shih, C. F. and Hutchinson, J. W, 1995, "A Computational Approach to Ductile Crack Growth under Large Scale Yielding Conditions," Journal of the Mechanics and Physics of Solids, **43**(3), pp. 389–413. https://doi.org/10.1016/0022-5096(94)00069-H